

# Exo-C

## IMAGING NEARBY WORLDS

EXOPLANET DIRECT IMAGING:  
CORONAGRAPH PROBE  
MISSION STUDY "Exo-C"

SCIENCE AND TECHNOLOGY DEFINITION TEAM (STDT)  
AND THE Exo-C DESIGN TEAM

INTERIM REPORT, MARCH 2014

The cost information contained in this document is of a budgetary and planning nature and is intended for informational purposes only. It does not constitute a commitment on the part of JPL and Caltech.

© 2014. All rights reserved.

## Author List

### *Science and Technology Definition Team*

Karl Stapelfeldt.....	NASA Goddard (Chair)
Ruslan Belikov.....	NASA Ames
Geoffrey Bryden.....	JPL/Caltech
Kerri Cahoy.....	MIT
Supriya Chakrabarti.....	UMass Lowell
Mark Marley.....	NASA Ames
Michael McElwain.....	NASA Goddard
Victoria Meadows.....	Univ. of Washington
Eugene Serabyn.....	JPL/Caltech
John Trauger.....	JPL/Caltech

### *JPL Engineering Design Team*

Michael Brenner.....	Exo-C Design Lead
Keith Warfield.....	Probe Study Office
Frank Dekens.....	System Engineer
Paul Brugarolas.....	Pointing Engineer
Serge Dubovitsky.....	Flight Operations
Robert Effinger.....	Thermal Engineer
Brian Hirsch.....	Mechanical Engineer
Andy Kissel.....	Engineering Dynamics
John Krist.....	Optical Simulations
Jared Lang.....	System Engineer
Joel Nissen.....	Optical System Engineer
Jeff Oseas.....	Optical Design Engineer
Eric Sunada.....	Thermal Engineer

### *With Additional Contributions by*

Sean Domagal-Goldman.....	NASA Goddard
Marc Kuchner.....	NASA Goddard
Peter Lawson.....	JPL/Caltech
Aki Roberge.....	NASA Goddard
Jagmit Sandhu.....	JPL/Caltech
Sara Seager.....	MIT

# 1 Table of Contents

2	Executive Summary .....	2-1
3	State of the Field at the Time of Probe Launch: The Exoplanet Science Landscape in 2024.....	3-1
3.1	Indirect Detections Using Stellar Reflex Motion .....	3-1
3.2	Transits .....	3-1
3.3	Exoplanet Imaging Detections.....	3-1
3.4	Disk Imaging .....	3-2
3.5	Summary.....	3-3
4	Design Reference Mission .....	4-1
4.1	Introduction: High-level Statement of Science Goals .....	4-1
4.2	Detailed Description of Science Objectives.....	4-2
4.2.1	Exoplanet Target Samples .....	4-2
4.2.2	Giant Planet Spectra.....	4-4
4.2.3	Small Planet Spectra .....	4-8
4.2.4	Debris Disk Imaging.....	4-11
4.3	Measurement Requirements .....	4-15
4.3.1	Imaging Requirements.....	4-15
4.3.2	Spectroscopic Requirements.....	4-17
4.3.3	Mission Lifetime .....	4-20
4.4	Derived Instrument Requirements.....	4-20
4.4.1	Overview.....	4-20
4.4.2	Telescope Aperture .....	4-21
4.4.3	Coronagraphy .....	4-21
4.4.4	Wavefront Control.....	4-21
4.4.5	Stray Light .....	4-21
4.4.6	Imaging .....	4-22
4.4.7	Spectroscopy.....	4-22
4.4.8	Detectors .....	4-23
4.4.9	Baseline Instrument Concept.....	4-23
4.5	Mission Lifetime Science Observations Budget .....	4-23
4.6	Science Requirements Flow-Down .....	4-23
4.6.1	Science Requirements to Mission Requirements .....	4-23
4.6.2	Flight System Requirements.....	4-24
4.6.3	Payload Requirements .....	4-24
4.6.4	Spacecraft Requirements .....	4-24
4.7	Top-level Description of the Instrument and Mission .....	4-25
5	Architecture Trades.....	5-1
5.1	Payload Trades .....	5-1
5.1.1	Optical .....	5-1
5.1.2	Mechanical .....	5-12
5.1.3	Thermal .....	5-12
5.2	Mission and S/C Trades.....	5-13
5.2.1	Earth-trailing vs. L2 Orbit Trade.....	5-13
5.2.2	S/C Architecture.....	5-17
5.2.3	Mission Lifetime and Operations .....	5-17
5.2.4	Solar Array and High Gain.....	5-19

6	Baseline Configuration and Implementation for Detailed Study .....	6-1
6.1	Baseline Configuration Overview .....	6-1
6.2	Mechanical Configuration.....	6-1
6.3	Payload Optical Configuration.....	6-3
6.3.1	Payload Optical Block Diagram .....	6-4
6.4	Telescope.....	6-4
6.5	Instrument .....	6-5
6.5.1	Coronagraph.....	6-5
6.5.2	Fine-guidance Sensor.....	6-6
6.5.3	IFS .....	6-7
6.5.4	Detectors .....	6-7
6.5.5	LOWFS.....	6-8
6.5.6	Field Layout.....	6-10
6.6	Thermal.....	6-11
6.6.1	Telescope .....	6-11
6.7	Pointing Control Architecture.....	6-12
6.7.1	Introduction.....	6-12
6.7.2	Pointing Architecture.....	6-12
6.7.3	Pointing Requirements .....	6-13
6.7.4	Heritage .....	6-14
6.8	Electrical Configuration .....	6-14
6.9	Interfaces .....	6-15
6.9.1	Isolators.....	6-15
6.9.2	Electrical.....	6-15
6.10	Payload Structural Thermal Optical Performance Modeling.....	6-15
6.11	Spacecraft.....	6-17
6.11.1	Structure .....	6-17
6.11.2	Propulsion.....	6-18
6.11.3	Attitude Control .....	6-18
6.11.4	Electrical Power.....	6-19
6.11.5	Avionics .....	6-20
6.11.6	Communications.....	6-20
6.11.7	Thermal .....	6-21
6.12	Ground Subsystem .....	6-21
7	Mission Operations and Data Analysis .....	7-1
7.1	Mission Operations .....	7-1
7.1.1	Spacecraft Management.....	7-1
7.1.2	Target Acquisition.....	7-1
7.1.3	Instrument Optimization and Maintenance .....	7-1
7.1.4	Science Observations.....	7-1
7.1.5	Operations Flow.....	7-2
7.2	Science Data Analysis .....	7-5
7.2.1	Science-processing Pipeline.....	7-5
7.2.2	Data Distribution and Archiving .....	7-5
8	Mission Cost Estimation.....	8-1
8.1	Cost.....	8-1
8.2	Schedule .....	8-3
9	Technology Needs Assessment .....	9-1
9.1	Technology Inheritance.....	9-1

9.2	Critical Coronagraph Technologies .....	9-1
9.3	Technology Needs In Common with AFTA .....	9-1
9.3.1	Low-order Wavefront Sensor .....	9-2
9.3.2	Integral Field Spectrograph .....	9-2
9.3.3	High-contrast Actively-corrected Coronagraph .....	9-3
9.4	Focused Technology Needs for Exo-C .....	9-4
9.5	PIAA and LOWFS Technology and Testbed Demonstrations .....	9-4
9.5.1	Introduction .....	9-4
9.5.2	Overview of Technology Readiness .....	9-4
9.5.3	SSS Components, Hardware, and Algorithms .....	9-5
9.5.4	Testbeds and Results .....	9-7
9.6	Vortex Probe .....	9-10
10	Plans for the Rest of the STDT Studies .....	10-1
10.1	Planned Studies .....	10-1
10.1.1	Attitude Control .....	10-1
10.1.2	Thermal Design .....	10-1
10.1.3	Optical Design .....	10-1
10.1.4	Mechanical Design .....	10-2
10.1.5	Wavefront Sensing .....	10-2
10.1.6	STOP Modeling .....	10-2
10.1.7	Coronagraph .....	10-2
10.2	Conclusions .....	10-2
11	Conclusion .....	11-1
12	References and Acronyms .....	12-1
12.1	References .....	12-1
12.2	Acronyms .....	12-7

## 2 Executive Summary

We report on the progress of a NASA-sponsored community mission study “Exo-C” of a space telescope designed to directly image and spectrally characterize exoplanets and circumstellar disks at optical wavelengths. The mission employs an internal coronagraph with precision wavefront control to study nearby, known exoplanets detected by ground-based radial velocity and new discoveries of exoplanets down to super-Earth size. It will resolve structures and measure dust properties in a large sample of exo-Kuiper belts and a smaller sample of habitable zones. It has the potential to detect Earth-twins if they are present around a few of the nearest stars, if the exozodi is low and if exceptional telescope stability is achieved. This represents a wide range of science containing characterizations and surveys, essentially making Exo-C an “Exoplanetary Grand Tour” of the immediate solar neighborhood. In addition, the high-contrast direct imaging capabilities of Exo-C will be useful for general astronomy.

Exo-C’s science goals are to: (a) spectrally characterize at least a dozen giant planets detected by radial velocity (Figure ES-1); (b) search at least 100 nearby stars (including alpha Centauri) at multiple epochs for planets

down  $\sim 3 \times 10^{-10}$  contrast, detecting and spectrally characterizing objects down to super-Earth sizes (Figure ES-2); and (c) image hundreds of circumstellar disks in search of dynamical structures induced by the gravity of planets too small to detect by any other means.

Exo-C fits very well on NASA’s exoplanet exploration path, with its basic mission concept endorsed by the Astro2010 Electromagnetic Observations from Space (EOS) panel. It will image and spectrally characterize planets and disks in reflected light. It will achieve image contrast levels that surpass what can be done from the ground (even by Extremely Large Telescopes (ELTs) equipped with extreme adaptive optics), what can be done by current space telescopes, or by the James Webb Space Telescope (JWST). Exo-C will characterize cool planets in orbits at or beyond 1 AU irrespective of their orbit inclination to the line of sight, allowing equal access to all nearby stellar hosts and probing a different population than the set of hot, short period planets that may be characterized by transit spectroscopy. In addition to its compelling and unique science, Exo-C will also serve as a technology pathfinder for a future new worlds mission capable of detecting atmospheric biomarkers on Earth analogs orbiting nearby stars.

The Exo-C baseline design is in place and

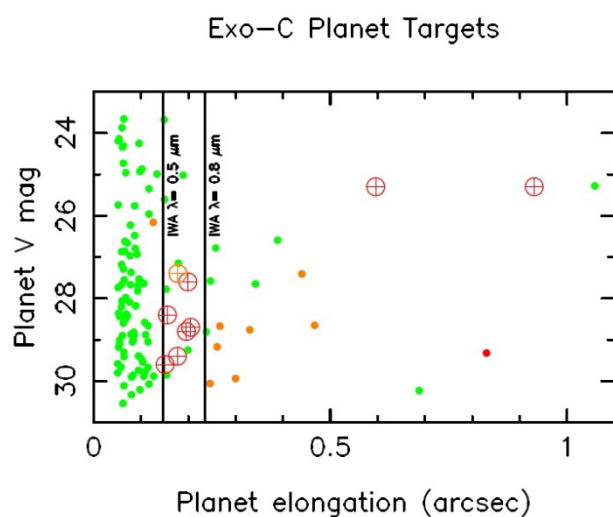


**Figure ES-1.** Known RV planets (points) and HZs accessible to Exo-C. Color codes for contrast difficulty.

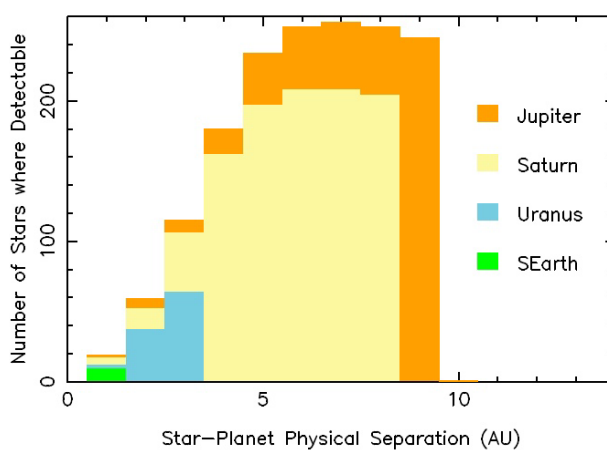


**Figure ES-2.** Exo-C exoplanetary search space among nearby stars, as a function of planet size and orbit.

will continue to be refined for the remainder of the study in 2014. Exo-C's aperture, orbit, spacecraft, and lifetime are very similar to those of the Kepler mission, which is our cost reference. This allows a mission cost that is below \$1B, including 30% contingency and the launch vehicle. It also builds on a rich heritage of exoplanet direct imaging mission concepts that have been proposed and studied by individual groups a dozen times since 1999. We highlight steps taken thus far to reduce mission cost and risk relative to previously proposed coronagraph mission concepts. These include the use of an intermediate class launch vehicle and choosing an orbit where no propulsion is needed after launch.

We present the interim design of the mission and science payload. The baseline Exo-C design is an unobscured Cassegrain telescope with a 1.5-m clear aperture, in a highly stable Earth-trailing orbit, and designed for a 3-year science mission lifetime. It carries a starlight suppression system (SSS) instrument consisting of the following elements (in optical train order): fine-guidance and low-order wavefront sensor (FGS/LOWFS), wavefront control (WFC) system based on two large-format deformable mirrors, a coronagraph, an imaging camera, and an integral field spectrometer (IFS). The science instrument is mounted laterally on the anti-Sun side of the telescope, obviating the need for high incidence reflections and better isolating it from spacecraft disturbances. The instrument delivers  $10^{-9}$  raw contrast over a  $\sim 2 - 20 \lambda/D$  field of view over the wavelength from 450 to 1000 nm, and with spectral resolution ranging from  $R = 25$  (for  $< 600$  nm) to 70 (for  $> 600$  nm).

The telescope is designed for precision pointing and high stability. Two stages of vibration isolation are used between the reaction wheels and the science payload, the solar arrays and high gain antenna are body-fixed, and a stiff inner barrel assembly is used as the telescope metering structure (Figure

ES-3). Telescope pointing is updated at a high rate using the bright science target star as a reference to drive a fine steering mirror. Active

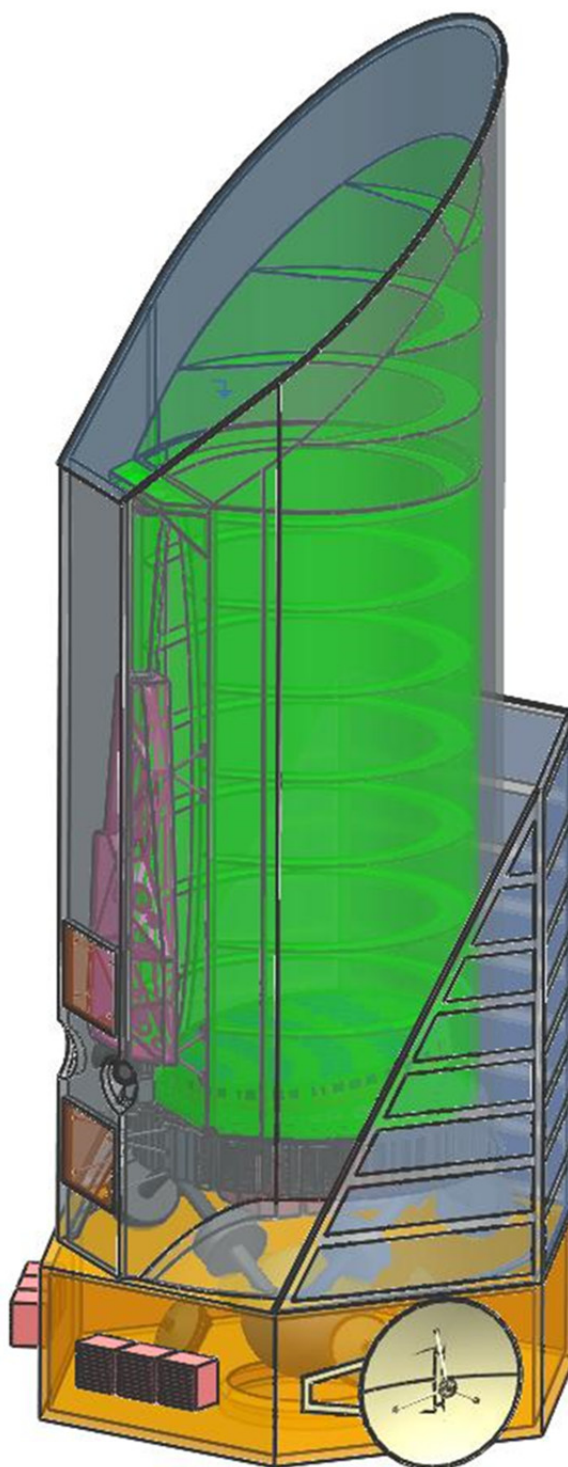


**Figure ES-3.** Visualization of the interim Exo-C observatory design. A Kepler-like spacecraft is used to host a telescope aperture comparable to Kepler's.

thermal control is used for the telescope, instrument, and inner barrel assembly—all of which are enclosed in a passive outer barrel assembly. Stability analyses via modeling of the structural, thermal, and optical performance of this configuration show that it can meet Exo-C's science goals.

Five coronagraph options were evaluated for use on the mission: hybrid Lyot, phase-induced amplitude apodization (PIAA), shaped pupil, vector vortex, and the visible nuller. Preliminary evaluations resulted in the selection of the hybrid Lyot as a baseline, with vector vortex and PIAA remaining as options for our second design cycle. All three coronagraphs have already demonstrated performance in the laboratory that is close to Exo-C's requirements; they differ primarily in which of three key performance parameters (inner working angle, contrast, and spectral bandwidth) still need to be improved. A major area for continued technology development is a dynamic testbed demonstration of

coronagraph performance, during which the FGS and LOWFS are operating to counteract flight-like disturbances. Concurrent work by the AFTA/WFIRST Coronagraph study will address this goal, and an IFS has been funded for vacuum testing. Some additional hardware development and testbed time with unobscured apertures will be needed to bring one or more of these coronagraphs to TRL 6 by FY 17.

Remaining work in the study includes developing higher-fidelity science simulations; another coronagraph design cycle and evaluation to maximize science yield and minimize risk; complete our understanding of telescope and instrument stability through modeling and lessons learned from Kepler; and continuing efforts to minimize cost. Two rounds of Cost and Technical Evaluation (CATE) will take place with the Aerospace Corporation during 2014. The Exo-C mission study will be completed in early 2015 and evaluated by NASA for potential flight at the end of this decade.

### 3 State of the Field at the Time of Probe Launch: The Exoplanet Science Landscape in 2024

Planetary systems consist of gas giant planets, rocky terrestrial planets, and belts of small bodies that generate debris particles. Ongoing research, upcoming developments in ground-based instrumentation, and the launch of new space missions will continue to advance our knowledge of these three exoplanetary system components in the coming decade. Nevertheless, a probe-scale exoplanet direct imaging mission can offer unique capabilities. Below we set the likely context for exoplanet science at the time Exo-C/S would launch.

#### 3.1 Indirect Detections Using Stellar Reflex Motion

Radial velocity (RV) surveys have detected almost 550 planets as of early 2014 (<http://exoplanets.eu>); the median orbital period of these detections is around 1 year. While the median semi-amplitude of these detections is 40 m/sec (<http://exoplanets.org>; larger than the solar reflex velocity induced by Jupiter), only a dozen planets have measured RV semi-amplitude below 2 m/sec. The best claimed detection to date has a 0.5 m/sec semi-amplitude for the very bright star  $\alpha$  Centauri B. Today's measurement precision of 50 cm/sec is expected to improve toward 10 cm/sec with the Very Large Telescope (VLT)/Echelle SPectrograph for Rocky Exoplanet and Stable Spectroscopic Observations (ESPRESSO) and similar instruments on extremely large telescopes (European Extremely Large Telescope (E-ELT), Giant Magellan Telescope (GMT), Thirty Meter Telescope (TMT)). However, stellar RV jitter arising from spots and activity sets a natural noise floor near 2 m/sec (Bastien et al. 2014). Only in the quietest stars—or through careful averaging, filtering, and detrending of the data—will RV detections be achieved for semi-amplitudes below 1 m/sec. By 2024, RV surveys should

have detected any planets with periods  $< 20$  yrs and with Saturn mass or greater around most bright stars, Neptune mass planets with periods  $< 3$  yrs around many stars, and  $5 M_{\oplus}$  super-Earths with periods  $< 1$  yr in some systems. Complementary measurements of stellar astrometric wobble by the European Space Agency (ESA) Gaia all-sky survey will detect and measure orbit inclinations for planets of Jupiter mass or larger and periods  $< 5$  yrs around unsaturated nearby stars ( $V > 6$ ; Casertano et al. 2008). The orbital elements for the inner giant planets of nearby stars should be well in-hand by 2024.

#### 3.2 Transits

Transit observations with the Kepler and COncvection ROTation et Transits (CoRoT) telescopes have revealed the frequency and radius distribution of short-period ( $P < 1$  yr) exoplanets by photometrically monitoring selected fields of solar-type stars. The 2017 Transiting Exoplanet Survey Satellite (TESS) mission will identify shorter-period ( $P \sim$  several weeks) planets around several hundred thousand bright field stars distributed around the sky. Around M stars, TESS detections will extend down to  $1 R_{\oplus}$  in the habitable zone. RV follow-up of TESS detections will reveal their mass distribution and the planetary mass-radius relationship. Spectroscopic measurements made during transit and secondary eclipse by the James Webb Space Telescope (JWST), ELTs, and other facilities will constrain the temperatures and albedos of these planets, and for clear, low-molecular weight atmospheres will detect high-opacity atmospheric species such as NaI,  $H_2O$ , and  $CH_4$ . By 2024, transit work should have built a strong statistical picture of the bulk properties of inner planetary systems and led to atmospheric spectral information for many of their larger objects.

#### 3.3 Exoplanet Imaging Detections

Only a handful of exoplanets have been imaged directly in their near-infrared thermal emission (e.g., Marois et al. 2010; <http://exoplanets.eu>).

This is due to the limited contrast capabilities of current instrumentation (Lawson 2013, Figure 1), especially at small angular separations from a star. A new generation of high-contrast imagers based on extreme adaptive optics systems is now being deployed to large ground-based telescopes. Dozens of exoplanet imaging detections at  $10^{-7}$  contrast and  $\sim 0.5''$  separation should be achieved by these systems in the near-infrared (Gemini Planet Imager (GPI), VLT-Spectro-Polarimetric High-contrast Exoplanet Research (SPHERE)), which would enable detection and spectroscopy of thermal emission from warm ( $T > 200$  K; very young or massive) gas giant planets. An appropriately designed extremely large telescope (ELT) in the 30-m class would be capable of such detections at even smaller inner working angles  $\sim 0.12''$ , but with only modestly better contrast. However, extreme adaptive optical systems are not currently baselined for ELT first generation instruments.

Ground-based, high-contrast imaging is limited by rapid wavefront changes arising from atmospheric turbulence. For a solar twin at 10 pc distance (H mag 3), a deformable mirror sized to create a  $\sim 0.5''$  radius dark field cannot suppress the residual speckles to levels fainter than  $10^{-7}$  of the central star brightness. This limit is defined by the available photons per subaperture in a reduced coherence time (Oppenheimer and Hinkley 2009, Table 2) and is nearly independent of telescope aperture size. To detect fainter objects, speckle averaging and subtraction methods must be employed. It is unclear how well this could be done, as the temporal behavior of residual atmospheric speckles at  $10^{-7}$  contrast has never been characterized. Experience at less challenging contrast levels suggests that detections a factor of 10 below the raw contrast floor should be achievable.  $10^{-8}$  contrast would enable detections of thermal emission from nine massive giant planets around nearby solar-type stars (Stapelfeldt 2006). It has been suggested that ELTs could detect planets in reflected light as small as 1

$R_{\oplus}$  at this contrast level, if they are present in the 0.1 AU radius habitable zones of bright nearby M dwarfs (Guyon and Martinache 2013). However, the required stellar properties ( $V < 7$  for sufficient guidestar photons,  $d < 8$  pc to resolve the habitable zone with an ELT) results in a null target set.

JWST/Near Infrared Camera (NIRCam) coronagraphy should be capable of detecting companions at contrasts of  $10^{-6}$  at separations beyond 1.5 arcsec, capturing objects like our own Jupiter in  $4.5 \mu\text{m}$  thermal emission if they are orbiting the nearest M stars. The uncertain luminosity evolution of young giant planets clouds the picture somewhat (Marley et al. 2007), but it appears that some of the more massive planets orbiting nearby ( $d < 20$  pc), young (age  $< 1$  Gyr), low-mass ( $M < 1.0 M_{\text{sun}}$ ) stars could be in view by 2024.

### 3.4 Disk Imaging

Imaging of protoplanetary disks is being revolutionized by the Atacama Large Millimeter/submillimeter Array (ALMA), which will be able to resolve dynamical structures driven by protoplanets at angular resolutions approaching 0.01 arcsec. Protoplanetary disks in the nearest star-forming regions ( $d \sim 150$  pc) are ideal ALMA targets, as their high optical depths give them high surface brightness in the submillimeter continuum. Debris disks are found around older main-sequence stars, with many nearby ( $d \sim 25$  pc) examples. They are optically thin with a much lower dust content and much fainter submillimeter continuum emission; it will therefore be a challenge even for ALMA to resolve their detailed structure. ALMA will map a limited number of the brightest debris disks ( $L_d/L_{\text{star}} > 10^{-4}$ ) at 0.1 arcsec resolution. In addition to their exoplanet imaging capability, new adaptive optics coronagraphs now being deployed to large ground telescopes should image bright debris disks with comparable resolution and with sensitivity a few times better than ALMA but in the near-



## 4 Design Reference Mission

### 4.1 Introduction: High-level Statement of Science Goals

Over the past five decades, NASA has carried out ambitious space observatory projects designed to study the universe at new wavelengths with improved spatial resolution, spectral resolution, and field of view—and with precise timing or photometry. In the 21<sup>st</sup> century, exoplanet research has emerged as a new focus for astrophysics and offers new space mission opportunities to explore. A new observational domain—imaging at very high contrasts and very small angular separations—must be opened if we are to understand the properties, formation, and evolution of planetary systems around stars like the Sun.

The Exo-C probe mission will be NASA's first space observatory designed from the outset to meet the requirements of high contrast imaging. It brings together a ~1.5 m aperture, active wavefront control, coronagraphs with demonstrated technical readiness, and a highly stable spacecraft environment to enable optical wavelength studies of nearby planetary systems at billion-to-one contrast. Exo-C will directly image and take spectra of planets beyond the reach of other telescopes. The mission and hardware design is patterned on the highly successful Kepler mission to achieve the same goal of delivering groundbreaking exoplanet science at an affordable cost.

In the course of its 3-year mission, Exo-C will carry out four key studies:

***Spectroscopy of known exoplanets:*** Ten nearby stars host radial velocity (RV) planets with apastron distances greater than 0.25". These are cold objects presenting a contrast of  $10^{-9}$  in the optical and near-infrared. Existing ephemerides allow observations to be timed to coincide with their maximum elongations. Exo-C will take spectra of these objects and provide astrometric measurements that will

resolve the  $\sin(i)$  ambiguity in their masses. The spectra will be sensitive to features of CH<sub>4</sub>, NH<sub>3</sub>, and H<sub>2</sub>O in their atmospheres, thereby constraining their relative abundances, metallicity, and depth of any cloud decks. In addition, Exo-C will obtain optical spectra of hot young planets detected in the near-IR by ground observatories, constraining their temperatures and the presence of additional absorbers, including Na I and K I.

***Discovery of new planets in the solar neighborhood:*** RV surveys are incomplete for orbital periods >12 years, for early F and hotter stars lacking strong metallic lines in their spectra, for stars with high chromospheric activity, and for planets in nearly face-on orbits. Multi-epoch imaging with Exo-C's coronagraph has the potential to discover planets beyond RV limits around as many as 200 nearby stars. There are more than 70 stars within 25 pc that host close-in RV planets and would be prime targets for outer planet searches. Exo-C's contrast capability will permit detections of Jupiter-like planets on orbits out to 9 AU, Neptune-like planets out to 3 AU, 2 R<sub>⊕</sub> mini-Neptunes out to 1.5 AU, and super-Earths at 1 AU. Particularly important survey targets will be the two Sun-like stars of the alpha Centauri binary system, the Sun's nearest neighbor. In addition, spectral characterization of the brightest planet discoveries would be carried out.

***Structure and evolution of circumstellar disks:*** Debris disks trace the dust liberated by ongoing collisions in belts of asteroidal and cometary parent bodies. In addition to revealing the location of these belts, debris dust serves as a tracer of the dynamical signature of unseen planets. Exo-C will be capable of resolving rings, gaps, warps, and asymmetries driven by planetary perturbations in these disks. With contrast improved 1000× over the Hubble Space Telescope (HST), Exo-C will be sensitive enough to detect disks as tenuous as our own Kuiper Belt, enabling comparative studies of dust inventory and properties across stellar ages

and spectral types. Several hundred debris disk targets will be surveyed, including nearby stars with far-IR excess and RV planet systems where sculpted dust features might be seen. A smaller survey of young protoplanetary disks will reveal how small dust particles are distributed with respect to the larger particles traced by Atacama Large Millimeter/submillimeter Array (ALMA) imaging.

***Survey of Dust in Habitable Zones:*** Exo-C's inner working angle of 0.15" at 550 nm is sufficient to spatially resolve the habitable zones of 10 Sun-like stars and another 40 stars with earlier spectral types. A survey of these targets will search for extended surface brightness from exozodiacal dust, to limits within a factor of 5–10 of the dust levels found in our own Solar System. The detected surface brightness will constrain the dust inventory and albedo, thus helping to define the background levels against which future missions will observe Earth-like extrasolar planets. In the nearest examples, Exo-C images may show asymmetric structures indicative of planetary perturbations to the dust distribution.

## **4.2 Detailed Description of Science Objectives**

### **4.2.1 Exoplanet Target Samples**

There are more than 70 known planetary systems within 25 pc. The exoplanets in those systems that have widest angular separation are prime targets for direct imaging. Observing these known planets is much more efficient than blindly surveying nearby stars—minimizing integration time and maximizing the science return for the overall mission.

For the systems only known to have short-period planets, additional planets may be present on wider orbits and be detectable through high-contrast imaging. Even for systems not known to have planets, failed planet searches provide useful information in mission planning; the phase space that is ruled out directly constrains the expected yield for each star, enabling further refinement of the

target list and improving the mission performance.

#### **4.2.1.1 Radial Velocity Planets**

RV surveys have detected many exoplanets around nearby stars, several of which are prime targets for Exo-C imaging. Beyond simply knowing that a planet is present, RV detections also determine the orbital separation and relative illumination as a function of time, such that an optimal epoch for observation can be chosen within the observatory lifetime. RV measurements also constrain the planet mass, particularly when the orbital inclination is determined by direct imaging, which aids in subsequent interpretation of the optical spectra. The RV planets orbit mature, quiet stars for which excellent elemental abundances can be derived. This will allow meaningful comparison of abundances measured in the planetary atmospheres to those of the star.

As seen in Figure 4.2-1, ~20 known RV planets have large enough angular separation and are bright enough for Exo-C to image. With the instrument inner working angle (IWA) increasing with wavelength, a full spectrum from 0.45–1.0  $\mu\text{m}$  can be obtained for about half of these planets.

New exoplanets will continue to be detected by ongoing measurements of their RV signatures. Figure 4.2-2 shows the steady rise in the number of bright exoplanets on wide orbits. By the time of Exo-C's launch, improved instrumentation, combined with an increasing timespan of observations, will enable the detection of lower-mass and longer-period planets.

While RV detections offer excellent targets for imaging, RV nondetections provide the best upper limits on possible planets. For systems with accurate RV measurements over a ~10-year timeline, Saturn-mass planets at several AU can be ruled out. Many systems cannot be so well constrained however, due to their early spectral type, unusually active chromosphere, or contamination by a stellar companion.

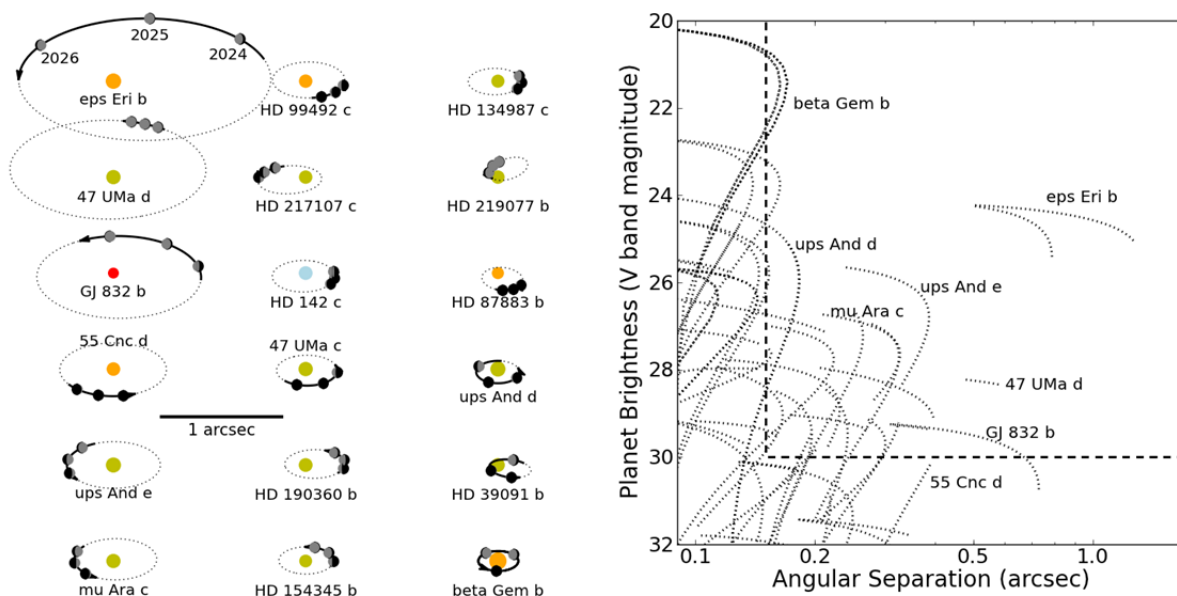


**Figure 4.2-1.** Exo-C will observe several known exoplanets whose orbital radius and orbital phase will be known during each observing epoch. The inclination and the orientation of the orbits remain unknown. Assuming an inclination of  $70^\circ$ , the illumination of the widest-separation/brightest planets is shown for three epochs from 2024 to 2026 (left panel). The brightness of each planet is shown as a function of orbital separation over the same time period (right panel). Targets must have sufficient angular separation ( $\geq 0.15''$ ) and must be bright enough ( $\geq 30$  mag) to be detected by Exo-C.

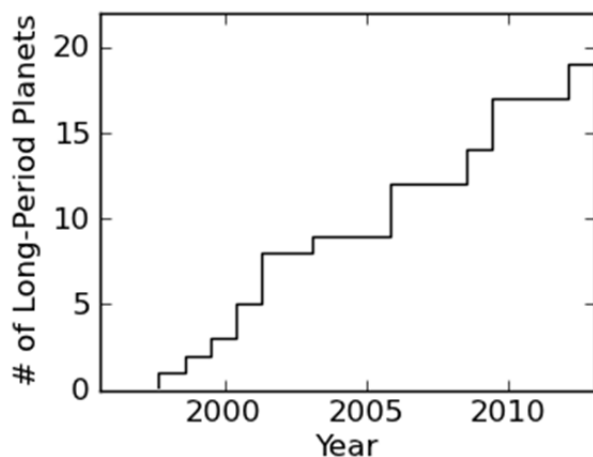


**Figure 4.2-2.** The number of known exoplanets that are good targets for Exo-C imaging continues to increase. The cumulative number of planets is shown for those with angular separation  $> 0.15''$  and whose host star is brighter than  $V = 7$  mag.

#### 4.2.1.2 Transiting Planets

Exo-C will not observe the well-known transiting planets, such as those discovered by Kepler and other surveys, since these stars are too far away and the planets orbit within the inner working angle (IWA) of Exo-C. The same is true of the planets to be discovered by

the Transiting Exoplanet Survey Satellite (TESS) and Planetary Transits and Oscillations of stars (PLATO). The cool, distant giant planets visible to Exo-C allow us to answer very different scientific questions than those raised by hot, transiting giant planets whose atmospheres are sculpted by intense irradiation, strong winds, exotic chemical and cloud processes, and atmospheric escape. The giant planets visible to Exo-C will likely be far more similar to Solar System giants to whose spectra they can be directly compared.

Transit surveys for exoplanets (e.g., Kepler, HAT, WASP) are highly biased toward short-period orbits and typically concentrate on faint, distant stars. As such, exoplanets detected by their transit signal are at too small angular separation for direct imaging by Exo-C. While the future TESS mission will find planets around brighter/closer stars, it will only be sensitive to very short ( $< 1$  month) periods.

#### 4.2.1.3 Planets Detected by Astrometry

The Gaia mission (launched Dec. 19, 2013) will provide all-sky measurements of stellar positions capable of detecting 24  $\mu$ s astrometric signatures on timescales less than the 3-year mission lifetime (Casertano et al. 2008). This accuracy is sufficient to detect the wobble induced by a Neptune-mass planet orbiting at 3 AU around a solar-mass star at 5 pc. This opens up new phase space for planet discoveries, even for stars that have been well covered by RV measurements.

However, the targets of interest for Exo-C are mostly too bright for Gaia. While the use of time-delayed integration (TDI) gates allows observation of stars beyond the nominal Gaia saturation limit ( $V = 12$  mag; Lindegren et al. 2012), our targets are even brighter than the TDI limits ( $V < 6$  mag). Unless the bright-star cutoff is improved by some new processing technique (e.g., using telescope diffraction spikes to determine stellar positions), Gaia is unlikely to discover any new planets around Exo-C target stars or to provide mass or inclination estimates for the targeted RV planets.

#### 4.2.1.4 Targets from Direct Imaging

New extreme adaptive optics coronagraphs (Gemini Planet Imager (GPI), Very Large Telescope/Spectro-polarimetric High-contrast Exoplanet Research (VLT/SPHERE), Subaru Coronagraphic Extreme Adaptive Optics (ScExAO)) should image dozens of young/massive planets in their near-infrared thermal emission. These will be targets for optical spectral characterization with Exo-C. A few current examples of such objects are beta Pictoris b and the four planets of the HR 8799 system (Lagrange et al. 2010; Marois et al. 2010).

#### 4.2.2 Giant Planet Spectra

Until now, the characterization of individual gas giant extrasolar planets has focused almost exclusively on the transiting giants. This unusual subset of planets orbits directly under

the glare of their primary stars on very short-period orbits. Transit studies from space have measured atmospheric temperatures and identified atmospheric absorbers in a few planets. In the past few years, a few young, self-luminous giant planets have been detected and studied in the near-infrared from large ground-based telescopes. These young objects have warm atmospheres that host exotic cloud decks of silicates and liquid iron drops.

However, giant planets cool as they age. By ages of 2 Gyr, those giants orbiting beyond 2 AU from their primary stars will generally have cooled well below 500 K. By focusing on older stellar systems from space, Exo-C will finally allow us to characterize the atmospheric composition and structure of those more statistically normal and more Solar System-like cool giant planets orbiting far from their primary stars.

The atmospheric envelopes of giant planets are composed predominantly of  $H_2$  and He gas enhanced with an uncertain mixture of the other elements. In the atmosphere, among the most abundant and spectroscopically interesting species, carbon will be found as  $CH_4$ , oxygen as  $H_2O$ , and nitrogen as  $NH_3$ . In warmer objects, Na and K gas may also be present. Disequilibrium effects and photochemistry can produce traces of other molecules, notably CO and hydrocarbons such as ethane and acetylene. As with the background  $H_2$  and He gas, none of these minor species have strong absorption features in Exo-C's wavelength range. The spectra of Exo-C giants are thus expected to primarily be influenced by  $CH_4$ ,  $H_2O$ ,  $NH_3$ , and the clouds formed by the condensation of these species, as well as photochemical hazes.

Spectra of Solar System giants and some model giants are shown in Figure 4.2-3. For such targets, the principal science questions that can be addressed are the relative abundances of these gaseous species, the properties of the cloud layers, the atmospheric

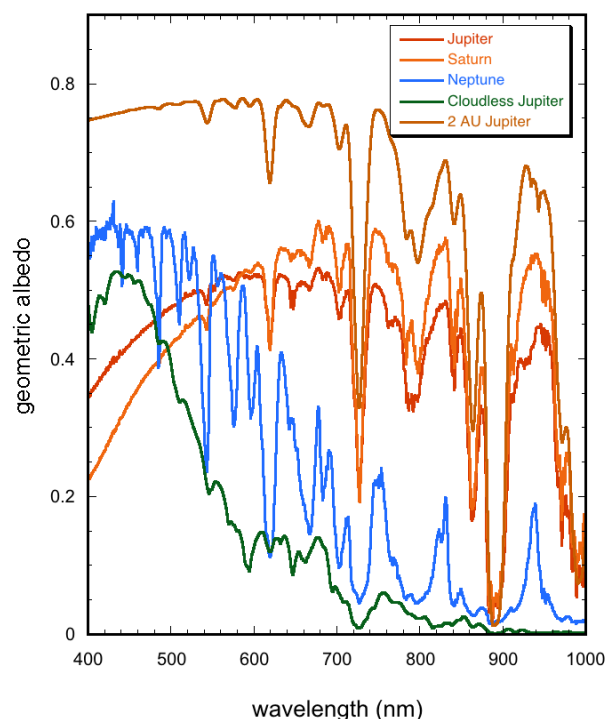


**Figure 4.2-3.** Geometric albedo spectra of real and model giant planets. Shown are Jupiter, Saturn, and Neptune (from Karkoschka 1994) and model spectra for two model giants, both with Jupiter’s mass and three-times solar abundance heavy element enhancement (from Cahoy et al. 2010). One model places Jupiter at 2 AU where it will have water clouds, leading (in the absence of photochemical smogs) to a very high albedo. In the second model, clouds are absent, a situation that may arise from a combination of smaller orbital distance and relative youth (such that the internal heat flow is larger than current day Jupiter). Such cloudless planets can be quite dark in scattered light with a distinctly blue Rayleigh scattering spectral slope.

temperature, and inferences about planet mass and planetary formation mechanisms.

Figure 4.2-4 illustrates the mass and equilibrium temperature of those RV planets that are most favorable for characterization by a direct imaging mission. Note the large range of masses and temperatures of the target objects. Depending on the atmospheric temperature, ammonia, water, or even methane or alkali clouds will be present in the atmosphere. Clouds are important as they sequester condensable species (e.g., water) and strongly affect the overall spectral shape.

The spectral characterization of extrasolar giant planets will address key science goals for

understanding the origin and evolution of planetary systems. Three of the most important questions are summarized below.

*How does the composition of gas and ice giant planets vary with planet mass, orbit, and stellar mass and metallicity?*

While RV surveys have constrained the architecture of many planetary systems, we do not yet know how the composition of giant planet atmospheres varies with these and other relevant parameters. By probing atmospheric composition for a healthy sample of extrasolar giant planets, Exo-C will ascertain if composition is correlated with mass, orbital radius, stellar type, or some other variables and thus provide key new clues for understanding planet formation.

Solar System gas giants are enhanced in heavy elements over solar composition by factors of three (Jupiter) and 10 (Saturn). The uniform enhancement across many elements

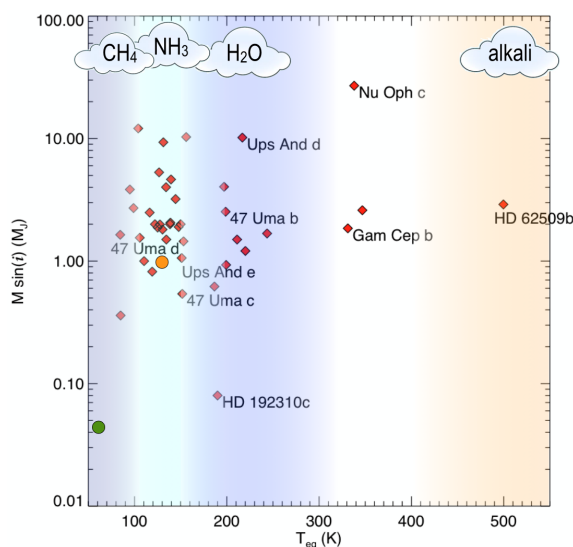


**Figure 4.2-4.** Measured  $M \sin(i)$  and estimate equilibrium temperature for known radial velocity planets with favorable angular separations from their primary stars. Equilibrium temperature assumes Jupiter’s albedo. Actual atmospheric temperatures will be warmer due to the contribution of internal heat flow, which depends on the age and mass of the planet. Approximate temperature ranges where various cloud decks will appear are indicated by colored bands with species labeled at the top. Some well-known planets are labeled. Jupiter and Neptune are depicted by the orange and green circles.

(C, N, S) at Jupiter was the greatest discovery of the Galileo entry probe mission and is a valuable piece of information regarding the giant planet formation process (Chabrier et al. 2007; Fortney et al. 2008). The enrichment may represent the accretion of icy planetesimals from the nebula after gas accretion. The roughly 30× solar enrichment in the envelopes of Uranus and Neptune may arise because the nebula did not survive long enough for it to capture large amounts of H<sub>2</sub> and He gas. With only four planets, the observed trends (increasing enhancement with decreasing mass and increasing orbital radius, for example) are not robust and limit our ability to understand how giant planets form.

Measuring atmospheric composition and temperature will illuminate how the giant planets formed and evolved with time. Statistics from transit, RV, and microlensing surveys suggest that Neptune-mass planets are very common. We have yet to learn whether these objects are mini Jupiters or are enhanced by factors of 30 to 50 over solar composition in heavy elements, like Uranus and Neptune.

The atmospheric elemental abundances that are most amenable to remote measurement are C, O, N, Na, and K. C, O, and N will be present as CH<sub>4</sub>, H<sub>2</sub>O, and NH<sub>3</sub>. Na and K are detectable in warm, cloudless Jupiter-like planets. Methane will likely dominate the visible spectra of directly imaged planets, but ammonia and water will be detectable in a few favorable cases. The best visible band for detecting water vapor in an extrasolar giant planet somewhat warmer than Jupiter is 940 nm. Other water absorption bands in the optical spectrum overlap with those of methane. The continuum flux level against which these bands will appear depends upon the height and thickness of atmospheric cloud layers and atmospheric photochemistry. In contrast, the far-red optical spectra of generally cloudless, hot, young self-luminous Jupiter-like planets will be dominated by the highly pressure-broadened lines of sodium and

potassium. These absorption bands of methane, water and alkali metals are the expected signatures of giant planet science targets for Exo-C. Measuring these features will constrain the atmospheric composition and temperature of planets even if the planetary radius and mass are uncertain.

*Do planets formed inside and outside of the nebular “snow line” have different compositions or C/O ratios?*

If both oxygen (through water) and carbon (methane) can be measured by spectroscopy then the C/O ratio of the atmosphere can be determined. The C/O ratio is crucial for discerning where in the protoplanetary nebula the object formed and what type of planetesimals were accreted during and after planet formation. Since water condensation at the “snow line” removes gaseous H<sub>2</sub>O from nebular gas, some giant planet formation models predict that planets formed at Jupiter-like separations from their stars are enhanced in C/O over the stellar value. Since the Galileo entry probe apparently entered an anomalous dry region of Jupiter, the Jovian C/O ratio is as yet unconstrained. If the Galileo value is indeed typical of the bulk of Jupiter then the Jovian C/O ratio may indeed be large. There have been attempts to measure the C/O ratio of the atmospheres of transiting giant planets; however, the realities of the wide Spitzer photometric bandpasses make such measurements ambiguous and there has not yet been a definitive measurement of C/O ratios in the atmosphere of any extrasolar giant planets. By directly measuring water abundance in a few gas giant atmospheres, Exo-C will resolve this issue.

As described in Oberg et al. (2011) the C/O ratio of the gas in a protoplanetary disk is expected to vary with orbital distance. This is because the “snow lines” for different species, particularly water and carbon monoxide, fall at different distances from the star. Between the H<sub>2</sub>O and CO snow lines, where giants detectable by Exo-C will form, most oxygen is

present as ice. This ice will form planetesimals and ultimately—in the core accretion model—planetary cores, while most carbon remains in the gas phase. As a result systematic variations in the C/O ratio of both the gas and in the condensed phases are expected. Whether a giant planet accumulates most of its atmospheric heavy elements from those present in the gas phase or from impacting planetesimals, this impacts both the atmospheric C/O ratio and the degree of overall atmospheric enhancement in heavy elements.

*How do clouds affect giant planet atmospheres and vary with atmospheric temperature and other planetary parameters?*

Every appreciable atmosphere in the Solar System is cloudy. This is almost certainly true outside of the Solar System as well. Iron, silicate, and various alkali clouds (e.g., Na<sub>2</sub>S) have been detected in the warm atmospheres of directly imaged young giant planets and clouds have been seen on at least one transiting planet. Since the giant planets that will be imaged by Exo-C are farther from their primary stars than the transiting planets—and older than the young, directly imaged giant planets—their atmospheres will be substantially cooler than both. Consequently, the giant planet atmospheres observed by Exo-C will likely contain water, ammonia, or possibly methane or alkali clouds (Figure 4.2-4). These clouds will greatly influence the reflected light spectra of these planets and the extraction of gaseous abundances will proceed in parallel with cloud characterization.

Cloud height can be discerned spectroscopically by measuring the relative depths of molecular absorption bands of diverse strengths. Cloud thickness and altitude is indicative of planet temperature. For extrasolar planets with typical ages of 200 Myr to 10 Gyr and masses of one to five Jupiters, the expected atmospheric effective temperature ranges from below 100 K to about 500 K (Figure 4.2-4). As a Jupiter-like planet cools over this range, water clouds first appear in

what is otherwise a relatively cloud-free sky, and then sink with falling effective temperature. At lower temperatures, ammonia and methane clouds appear. Thus, Exo-C will serve as an exoplanetary weather satellite by constraining cloud properties and atmospheric temperature on the directly imaged planets. The experience gained from interpreting giant planet cloud properties will be invaluable when spectra of directly imaged terrestrial planets become available.

Giant exoplanet characterization will benefit from a long, deep heritage in observing and modeling the reflected solar spectra of Solar System giant planets; the key issues are well understood. The reflected spectra of Solar System giants (see Figure 4.2-3) are dominated by strong methane absorption bands that punctuate a bright continuum flux set by cloud opacity in the red and by Rayleigh and haze scattering in the blue. The Galileo entry probe confirmed the measurement of atmospheric methane by ground-based observers. At Jupiter, NH<sub>3</sub> and H<sub>2</sub>O vapor abundances are challenging or impossible to measure from the ground as these species are condensed out into thick cloud decks. Exoplanets slightly warmer than Jupiter, because of their youth or proximity to their primary stars, will lack these cloud decks, making these gases much more accessible to remote observation.

We expect that planet characterization by Exo-C will follow a two-tiered strategy. All surveyed planets will be imaged in four or five broad filters. This will sample the continuum shape and be sufficient to identify planets with novel characteristics and separate likely gas and ice giants (Figure 4.2-5). A subset of the most interesting and brighter planets will be further characterized by R ~ 70 spectroscopy. This spectral resolution was chosen as the minimum required to uniquely identify both moderate and strong methane and ammonia bands along with the water band at 940 nm (see Table 4.2-1). Ammonia bands in the optical tend to overlap methane bands (Table

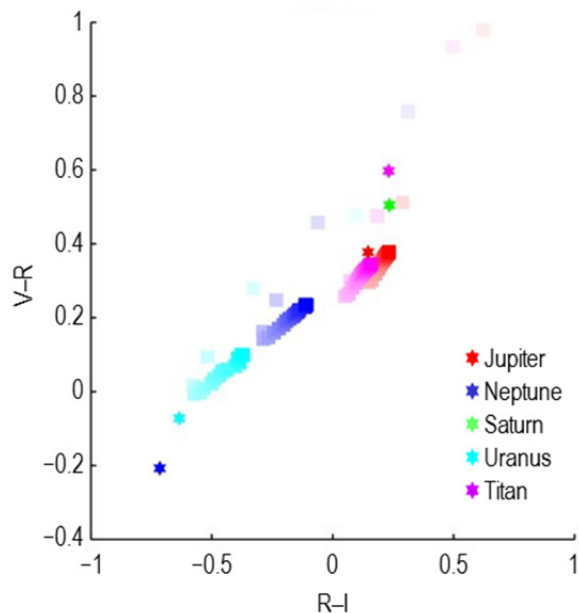


**Figure 4.2-5.** Color-color diagram from Cahoy et al. shows location of methane-rich Solar System objects (legend) and model planets (squares) placed at 2 AU. Red and magenta colors denote Jupiters with 1× and 3× enhancement over solar abundance in heavy elements. Blue and cyan are for 10× and 30× enhanced Neptunes. Intensity of color fades as model phase angle varies from 0° to 180° in 10° increments.

4.2-1); however, upper limits on  $\text{NH}_3$  abundance can also be set. Measuring a variety of molecular bands of varying strengths is desirable since the strongest bands will saturate at the higher abundances while the weaker bands will become prominent, yet still provide an accurate measure of column abundance.

In reflected light, cloud-free atmospheres are dark in molecular absorption bands. Clouds generally reduce the contrast between adjoining continuum and strongly absorbing spectral regions. By measuring the reflected flux in several methane bands of differing strengths, along with the shape of the continuum spectrum, Exo-C will constrain the gross scattering properties of the atmosphere (see Cahoy et al. 2010 for a more complete discussion).

**Table 4.2-1.** Characteristics of diagnostic giant planet absorption bands.

Species	Band Center (nm)	Width (nm)	R
$\text{NH}_3$	990	23	45
$\text{CH}_4$	990	20	50
$\text{H}_2\text{O}$	940	60	15
$\text{NH}_3$	930	20	50
$\text{CH}_4$	890	20	45
$\text{NH}_3$	890	27	35
$\text{CH}_4$	862	12	70
$\text{CH}_4$	840	10	85
$\text{CH}_4$	790	24	30
$\text{CH}_4$	725	10	70
$\text{NH}_3$	650	10	65
$\text{CH}_4$	620	8	80

Centers and widths (FWHM) of absorption bands of important absorbers in giant planet atmospheres. R give spectral resolution (following Des Marais et al. 2002) needed to detect the band if present in an atmosphere ( $R = \text{center/width}$ , rounded to nearest 5 for clarity).

The spectra of Jupiter and Saturn shortwards of 450 nm are also influenced by absorbing photochemical hazes produced by solar ultraviolet (UV) radiation. This photochemistry is only partially understood, but plays an important role in the stratospheric energy balance and temperature structure of giant planets. For gas giants on orbits inside of 5 AU, photochemistry and haze production will be important atmospheric processes. Observing the blue-wavelength albedo of a number of giant planets around both solar and non-solar-type stars will substantially increase the number of atmospheres in which photochemical processes can be studied.

### 4.2.3 Small Planet Spectra

#### 4.2.3.1 Scientific Context

The last two decades of exoplanet observations have been dominated by exoplanet discovery and initial physical characterization to determine planetary radius, mass, density, and orbital properties (e.g., Marcy et al. 2005; Lissauer et al. 2011; Howard et al. 2012; Marcy et al. 2014). Close-in giants, being larger and brighter, were the first planets discovered and characterized, but new RV and transit techniques, combined with more powerful instrumentation, are finding and

studying progressively smaller planets. Planets of a few Earth masses are now being discovered at distances from their parent star where there is a relatively high probability that they may harbor surface oceans and remotely detectable, global surface biospheres (Borucki et al. 2013; Anglada-Escude et al. 2013).

One of the great surprises from this period has been the discovery—primarily by the Kepler mission—of a plethora of planets with sizes and masses between that of Earth and Neptune (Figure 4.2-6, Howard 2013).

These planets have no analog to those in our own Solar System, and prior to their discovery were thought to be relatively rare (Ida and Lin 2004). Observations have found the opposite: super-Earth to sub-Neptune-sized planets are far more common than either ice or gas giant planets in the inner regions of planetary systems, although likely not as common as terrestrial planets.

Perhaps the most surprising exoplanet discovery to date, however, has been the observational confirmation that planets less massive than  $10 M_{\text{Earth}}$  are not necessarily solid, terrestrial super-Earth worlds with bulk compositions dominated by iron and silicate (Pollack et al. 1996), but may be low-density water and gas-dominated “mini-Neptunes” (Charbonneau et al. 2009; Lissauer et al. 2011) whose formation, composition, and evolution are not at all understood. Similarly, true super-Earths (rocky planets many times more massive than the Earth) have been confirmed (Leger et al. 2009). Depending on differences in internal structure and composition, they may have very different atmospheres from the terrestrial planets in our Solar System (Elkins-Tanton and Seager 2008). Their nature and evolution are also not well understood, primarily due to a dearth of observational data. We do not understand whether super-Earths and mini-Neptunes are two distinct planet classes that form via different mechanisms, or if they represent different end products for the same evolutionary sequence. The lack of

similar planet classes in our Solar System means that Exo-C is ideally suited guide our understanding of the nature, formation, and evolution of these common objects—and their potential suitability to support life.

While exoplanet detection and physical characterization continues apace—primarily using transit and RV techniques—another era has begun: the chemical characterization of exoplanets through direct imaging and

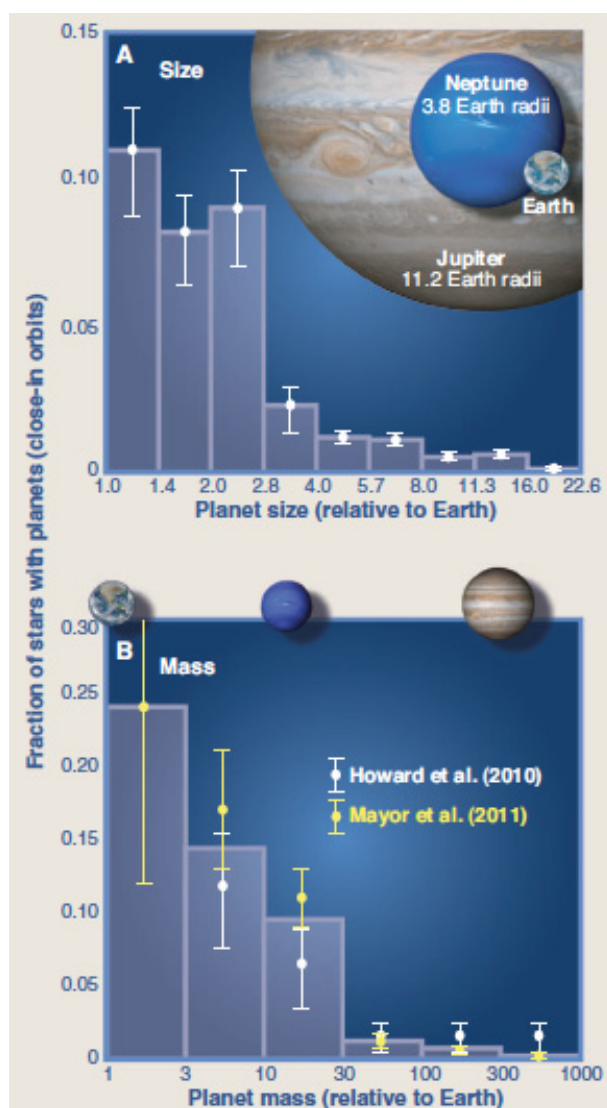


**Figure 4.2-6.** Current observations show the common nature of planets with sizes between Earth and Neptune. Histograms of known planets as a function of planet radius (top), and planet mass (bottom). Potential terrestrial planets smaller than Neptune ( $17 M_{\text{Earth}}$ ;  $3.8 R_{\text{Earth}}$ ) are much more common than larger gas giants (from A. Howard, *Science*, 2013).

spectroscopy. To date, characterization targets have predominantly been Jovian planets, but lower mass planets such as the mini-Neptune GJ1214b are also being characterized through transit spectroscopy (Bean et al. 2011; Kreidberg et al. 2014). Theoretical studies and observational measurements of density for smaller exoplanets are suggesting a dividing line near  $R = 1.7 R_{\oplus}$  between potentially habitable super-Earth objects with a relatively rocky composition and therefore the ability to support a liquid ocean on their surfaces, and likely uninhabitable mini-Neptune-class planets that retain relatively massive volatile envelopes (e.g., Rodgers 2013; Lopez et al. 2013). Empirically testing the nature of objects on either side of this theoretical line will require a spectroscopic census of planets of different sizes to determine the composition of the bulk of their atmospheres and to determine if there is a trend with planetary radius.

By the start of the next decade, we anticipate having the capability to obtain spectroscopy for planets with radii twice that of the Earth through transit observations with the James Webb Space Telescope (JWST). These transit transmission measurements, however, will be fundamentally limited to planets at the very upper end of the theoretical size limits for planetary habitability, and JWST will be better able to characterize those planets that orbit close to their parent star. Consequently, studies of planets in the habitable zone will likely only be possible for planets orbiting cooler M dwarf stars. Transit transmission observations will also likely be limited to probing the uppermost regions of an atmosphere, especially for more Sun-like stars (Betremioux and Kaltenegger 2013; Misra et al. 2014) and will never directly sample the surface compositions. Finally, the suite of spectral observations obtainable by JWST for planets with separations from their star consistent with potential habitability will likely be extremely small (Deming et al. 2009) as spectroscopic data can only be obtained during

the planetary transit, and multiple transits must be coadded over the lifetime of the mission to achieve adequate S/N for these targets. These data will likely be insufficient to adequately address questions related to the fundamental nature of these cooler sub-Neptune/super-Earth objects, including their formation history, whether they represent an evolutionary sequence, and their potential habitability.

To advance our ability to classify these objects and understand their nature, evolution, and potential habitability, we require a mission designed with the goal of spectroscopy through direct imaging of sub-Neptune planets. This is the only technique that can sample the atmospheric column and the surface properties of these planets and deliver spectroscopic information from a large enough sample to derive statistically meaningful inferences on their planetary properties and history. The most challenging goal of any such mission will be identifying and classifying potentially habitable worlds, and the first search for biosignature gases. Spectroscopic characterization of planetary environments will be the cornerstone of this search.

Specific goals for such a study include:

1. Take the chemical inventory, including absorbing gases and scattering aerosols, and estimate the bulk atmospheric elemental composition of sub-Neptune/super-Earth planets.
2. Search for H<sub>2</sub>O vapor as a marker of potential habitability for planets imaged in the habitable zone of their parent star.
3. For these potentially habitable worlds, conduct a preliminary search for at least one biosignature gas.

#### **4.2.3.2 What We Can Learn from the Spectrum**

We will search for and quantify trace gas absorption, and at visible wavelengths for sub-Neptune objects we anticipate that this will be primarily from H<sub>2</sub>O and CH<sub>4</sub>, with the possibility of detecting NH<sub>3</sub>, O<sub>3</sub>, and O<sub>2</sub>. Typical atmospheric bulk gases, such as H<sub>2</sub> and N<sub>2</sub> do not produce distinct absorption

features at visible wavelengths and will not be directly observable. CO<sub>2</sub> does have a very weak band at 0.93 μm, which may be visible for massive, CO<sub>2</sub>-dominated atmospheres with little or no water vapor. However, the presence of even a small amount of water vapor in the planetary atmosphere will produce a 0.94-μm water absorption band that will likely overwhelm the much weaker CO<sub>2</sub> absorption and preclude its detection. We may, however, be able to deduce bulk composition from detection of broadening of the trace gases such as water vapor. Detecting and quantifying either H<sub>2</sub>O or CH<sub>4</sub>, or both, will help to constrain the atmosphere's oxidation state and bulk gas composition. Specifically, a spectrum dominated by CH<sub>4</sub> and H<sub>2</sub>O constrains the atmosphere to be more reducing, with a higher H<sub>2</sub> abundance than a spectrum that contains no CH<sub>4</sub>, and is instead dominated by H<sub>2</sub>O features and, possibly, O<sub>3</sub>.

The slope of the observed spectrum may also reveal Rayleigh scattering from molecules in the atmosphere (rising toward the blue) or wavelength-dependent slopes produced by photochemical hazes such as H<sub>2</sub>SO<sub>4</sub> (grey slope) and hydrocarbons (rising toward the red). A non-blackbody slope can be used to indicate the presence of an atmosphere, and may give clues to the source of the scattering. A spectrally well-resolved slope may also give clues to the source of scattering in the atmosphere. A spectrally well-resolved Rayleigh slope may also be fit and removed, potentially revealing the presence of O<sub>3</sub> Chappuis bands from 0.5–0.7 μm. For cases where the atmosphere is nonexistent or relatively transparent, the surface will be directly sampled. The observed spectrum may then reveal the presence of surface minerals such as iron oxides, which have a strong, broad absorption feature at wavelengths below 0.6 μm, as is seen in the spectrum of Mars.

#### 4.2.4 Debris Disk Imaging

While exoplanets are the primary targets for this mission, planetary systems can also be imaged indirectly via their debris disks—the remnants left over after planets form. Ongoing destruction of asteroids and comets creates a continual supply of orbiting dust around most Sun-like stars (Bryden et al. 2006), including our own (Figure 4.2-7). In the Solar System, such dust is bright enough to be seen with the naked eye—so called zodiacal light. Far-infrared observations by the Spitzer Space Telescope and the Herschel Space Observatory have identified many neighboring stars with even brighter orbiting debris, orders of magnitude more than in the Solar System (Eiroa et al. 2013). Because they are so bright, optical imaging of debris disks is much easier than detecting their embedded planets.

A key objective for imaging debris disks is to resolve disk structure. High-resolution images taken by HST have revealed a wide variety of disk morphologies (Figure 4.2-8). Some disks are concentrated into narrow, well-defined belts while others are more diffuse. Some are very symmetric while others have pronounced asymmetries—offsets, warps, and

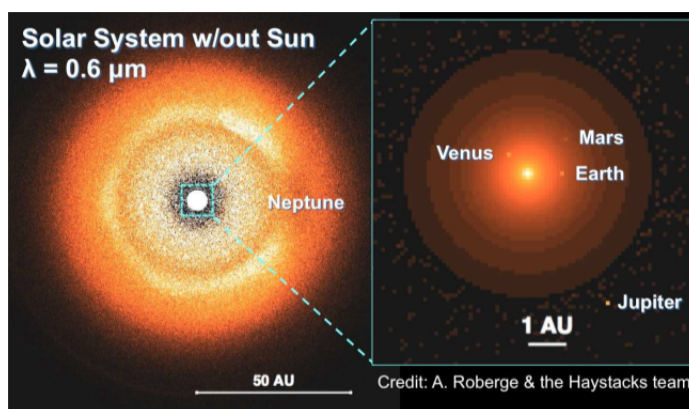


**Figure 4.2-7.** The Solar System's dust is much brighter than its planets. On the scale of the whole Solar System (left panel) or the inner 5 AU (right), the most conspicuous feature is the haze of emission coming from interplanetary dust. (Note that the Sun is not included in the above model, as if it had been perfectly suppressed by a coronagraph.) The partial ring in the outer Solar System's dust is caused by the dynamical influence of Neptune, which itself cannot be seen. The Earth creates a similar structure near its orbit, but with only a 10% enhancement of dust above the background zodiacal light (Kelsall et al. 1998).

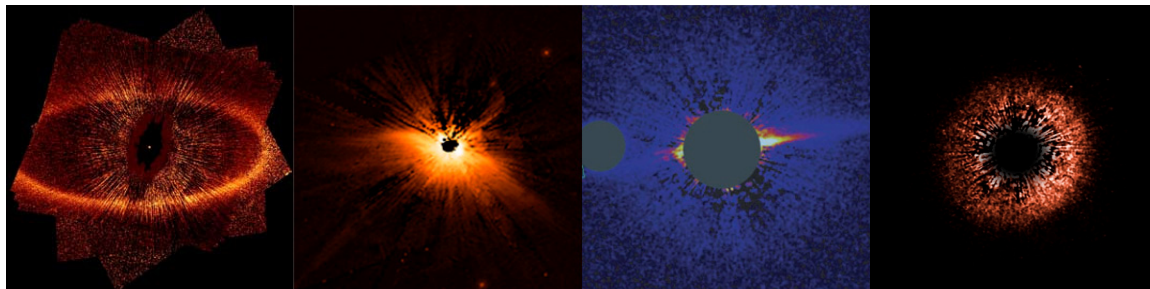


**Figure 4.2-8.** Optical imaging of debris disks by Hubble reveals a variety of disk structures—from smooth belts to eccentric rings, bow shocks, warps, and other asymmetric structure (Fomalhaut, Kalas et al. 2005; HD 61005, Hines et al. 2007; HD 107149, Ardila et al. 2004; HD 15115, Kalas et al. 2007).

clumps. To first order, the location of the debris gives a sense of the overall architecture for each system. Many systems have a two-belt architecture similar to the Solar System’s asteroid and Kuiper belts, for example, suggesting intermediate unseen planets. (In the case of HR 8799, there are four planets directly seen between the two belts; Su et al. 2009.) Some disk asymmetries can be used to infer the presence of individual planets. The planet-orbiting beta Pic, for example, was predicted based on the warp it created in the disk (Mouillet et al. 1997), years before the planet itself was eventually observed (Lagrange et al. 2010). Two other systems, Fomalhaut (Kalas et al. 2005) and HD 202628 (Krist et al. 2012), have offset eccentric rings with sharp inner edges, a configuration that will quickly disperse in the absence of a nearby shepherding planet.

Overall, Exo-C images of debris disks will probe the underlying planetary systems both generally, by mapping the system architecture, and specifically, by determining the location of individual planets.

#### 4.2.4.1 Observation of Known Disks

*Is the Solar System’s two-belt architecture normal?*

High-resolution images taken by Exo-C will greatly expand on the ~20 disks that have been imaged by Hubble. The rough sizes for over 100 disks have now been measured by low-resolution thermal imaging with Herschel (Figure 4.2-9). Whether or not the known

orbiting material is spread over a wide disk or concentrated into one or more thin rings remains to be seen. Exo-C observations will not only resolve the known outer disks—typically orbiting at 10s of AU—but also push in toward the inner reaches of each system, potentially identifying new warm asteroidal belts that accompany cold outer material.

Since the disks already discovered via their thermal emission are relatively large, some of these cold components fall outside of the Exo-C’s outer working angle (OWA). Using Exo-C’s longest wavelength band for disk observations provides the best match between field-of-view (FOV) and the known disks’ angular sizes. For disks that are smaller or have warm components discovered by Exo-C, observations at the shortest wavelength band will provide the best IWA for probing the inner disk. Measurements of disk color provide a constraint on the size of the scattering dust grains.

The primary objective of the disk imaging will be to identify the radial distribution of the orbiting dust. Exo-C will easily distinguish between thin well-defined rings and broad pancake-like morphologies, allowing for identification of multiple-belt systems like our own. As a secondary objective, Exo-C will also measure disk colors. While most disks observed by Hubble have red colors, AU Mic’s disk is blue, indicative of small, submicron grains.

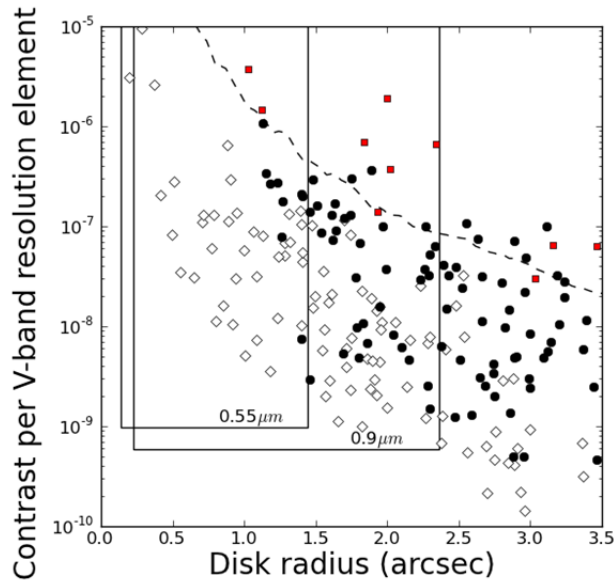


**Figure 4.2-9.** Exo-C will image many known debris disks. For systems observed by Herschel in the far-IR, the estimated contrast per resolution element is shown for systems with a range of disk sizes. Disks that are detected by Hubble are shown as red squares while those marginally resolved by Herschel are black circles. Disk size estimates for unresolved systems are shown as open diamonds. While JWST's sensitivity to disks (dashed line) is comparable to Hubble's, the detection space for Exo-C in V and I bands (U-shaped lines) contains many new targets.

#### 4.2.4.2 New Discovery Space

*How is dust produced and transported in debris disks?*

Observations by Exo-C will not only expand on the number of imaged disks, but, by pushing to much fainter contrast ratios, will cross an important threshold in disk physics, opening up for the first time an entirely new class of disk images. Brighter disks—all the ones currently imaged—are *collision dominated*; the dust grains we observe are mainly destroyed by collisions with other grains. Disks with optical depths less than  $\sim v_{\text{Keplerian}}/c$  are predicted to be *transport dominated*, meaning that grain-grain collisions are rare enough that grains can flow throughout the planetary system under the influence of radiation drag forces until they are sublimated in the star's corona or ejected from the system by an encounter with a planet. This

transition between collision dominated and transport dominated is below a contrast level of  $\sim 10^{-7}$ , so Exo-C will be the first mission capable of confidently detecting a range of transport-dominated disks (see Figure 4.2-9).

The physics of transport-dominated disks is much simpler than that of collision-dominated disks, so it is easier to interpret their morphology in terms of the properties of hidden planets that are perturbing them. Modeling the dust distribution in collision-dominated disks requires an understanding of the details of collisional processing and the distribution of planetesimals, remnants of the complex process of planet formation and migration. However, dust transported away from its source can be modeled with a simple N-body integrator, and the range of possible planet-dust interactions is already understood. Presently, the only known example of a transport-dominated debris disk is the Solar System's, where the dynamics are mostly well understood.

#### 4.2.4.3 Indirect Detection of Planets

*What planets exist in the outer reaches of nearby planetary systems?*

Planets orbiting at semi-major axes beyond  $\sim 10$  AU have orbits too long to permit detection via RV, transit, or astrometric techniques. They are also too low in contrast for direct imaging. The only way to probe the frequency of planets in the outer reaches of nearby planetary systems is to study the structure they induce in their surrounding debris disks.

Observations of debris disks commonly identify potential signatures of driving planets such as narrow, eccentric rings (e.g., Fomalhaut, Kalas et al. 2005; HD 202628, Krist et al. 2012) and inclined warps (e.g., beta Pic, Lagrange et al. 2010; AU Mic, Krist et al. 2005). Depending on the optical depth of the dust disk (i.e., whether it is collision dominated versus transport dominated), it can also create patterns by trapping dust grains into mean motion resonances. These resonant

structures not only point to the location of the planet, but also constrain its mass and eccentricity.

Furthermore, planets may have detectable amounts of dust orbiting the planet itself, which can build up through inspiraling or capture following a planetesimal collision. The resulting point source has a flux that is inconsistent with planet photosphere models. For example, the object known as Fomalhaut b that orbits within the Fomalhaut debris disk is too bright at optical wavelengths compared to its thermal emission to be explained as a bare exoplanet photosphere. However, observations are consistent with dust produced by the collisional decay of an irregular satellite swarm around a  $\sim 10 M_{\text{Earth}}$  planet. Depending on the planet's orbital distance, Exo-C could be capable of detecting Fomalhaut b analogs with a thousand times smaller dust content, allowing an exploration of this newly discovered phenomenon over a wide range of fluxes that have been inaccessible to any previous telescope. Most directly imaged planets so far are associated with debris disks, so understanding the nature of these dust-enshrouded planets is an important step to interpreting images of exoplanets. Moreover, since these objects may illustrate the process of satellite and ring formation, they may offer clues that will help us understand processes in our own Solar System, like the formation of the outermost satellites such as Callisto and Iapetus.

#### **4.2.4.4 Exozodiacal Dust**

*How much dust will obscure future images of Earth analogs?*

While many debris disks have been found with cold ( $\sim 50\text{--}100$  K) dust orbiting tens of AU from the central star, relatively little is known about the warmer dust ( $\sim 200\text{--}300$  K) located in nearby stars' habitable zones. By analogy to the Solar System's zodiacal light, this warm component of debris disks is referred to as exozodiacal dust (or exozodi, for short). Background flux from exozodiacal dust in

other systems will likely exceed the signal of an Earth-analog exoplanet in direct images and spectra, even if exozodi levels are no greater than the Solar System level. Therefore, exozodiacal dust complicates direct imaging of exoplanets in two ways: (1) as a source of noise, and (2) as a source of confusion. A discussion of these problems appears in Roberge et al. (2012). The exozodi levels around nearby stars will be as important to the success of efforts to characterize Earth-like exoplanets as the fraction of stars with potentially habitable planets ( $\eta_{\oplus}$ ).

The most important exozodi characteristic for exoplanet direct imaging at optical wavelengths is the scattered light surface brightness near the target planet, which depends on both the dust abundance and its albedo. A new survey for exozodi around nearby stars using the Large Binocular Telescope Interferometer (LBTI) is slated to begin within the next year (Hinz 2013). The LBTI survey will measure the integrated  $10\ \mu\text{m}$  thermal emission from warm dust down to about 10 times the Solar System exozodi level, providing sensitive information on the warm dust content.

However, the LBTI survey will not address two additional aspects of the exozodi problem for a future exo-Earth imager. First is the issue of how to convert the observed  $10\text{-}\mu\text{m}$  dust emission to an optical surface brightness: a value for the dust albedo must be adopted. By measuring the scattered light surface brightnesses in the habitable zones of some LBTI target stars, Exo-C can directly measure the dust albedo. The values obtained can then be used to predict scattered light brightnesses for other dust disks observed in the thermal infrared. In the process, valuable information on the composition of the exozodi grains will be obtained, shedding light on the composition of the parent planetesimals and the planet formation processes that created them. Secondly, the LBTI survey data will provide little information on the spatial distribution of

the exozodiacal dust. Resolved images in scattered light can reveal greater details of the radial and azimuthal structure of exozodiacal clouds, potentially detecting dust rings or asymmetries driven by planetary perturbations. Exo-C thus provides the added opportunity to detect habitable zone planets indirectly via their gravitational effects.

#### 4.2.4.5 Young Disks

*How does the dust in planetary systems evolve?*

The short integration times associated with bright debris disks allow Exo-C to observe many of such disks—a large enough sample to look for statistical trends with stellar age and spectral type. Beyond the core survey of the nearest debris disks, additional disks of different ages will also be included. In particular a select sample of young protoplanetary disks will be observed. The optical scattered-light images of these disks will be complementary to the thermal emission measured by ALMA, allowing for detailed modeling of the disks' constituent particles.

### 4.3 Measurement Requirements

#### 4.3.1 Imaging Requirements

##### 4.3.1.1 Starlight Suppression

**Brightness of uncontrolled speckles in coronagraphic dark field.** As seen by an observer outside of the Solar System, the reflected light brightness of Jupiter at quadrature relative to the Sun is given by  $\frac{1}{4} \times (\text{albedo}) \times (R_J / 5.2 \text{ AU})^2 = 10^{-9}$ . In order to detect a Jupiter analog around other stars, or to detect smaller planets in closer orbits, Exo-C must suppress diffracted, scattered, and stray light in a single resolution element down to a direct starlight level of  $10^{-9}$ . For a  $V = 3.7$  star, this contrast level also corresponds to the count rate from residual starlight, becoming comparable to the detector dark current background in a single resolution element. A  $10^{-9}$  contrast thus serves as a natural break point for background-limited integration times in the majority of our targets.

**Stability of uncontrolled speckles in coronagraphic dark field.** Exo-C is required to detect planets whose brightnesses are below the residual uncontrolled speckle level specified above. A planet whose contrast is  $10^{-9}$  at elongation could appear fainter at another orbital longitude, so achieving detections at more challenging contrast levels is required for robust planet searches. In addition, we aspire to detect planets as small as  $1.7 R_{\oplus}$  (corresponding to the onset of the rocky planet regime), and these will always appear at contrasts below  $10^{-9}$ . The key to detecting fainter objects is residual speckle pattern stability. Speckle stability at the level of  $10^{-10}$  would enable exoplanet detections at contrasts of  $3 \times 10^{-10}$ , meeting both of the above objectives. In addition,  $10^{-9}$  contrast planets around nearby stars will have reflected light brightnesses in the  $V = 23\text{--}29$  range, with median  $V$  of 27. The median integration time for spectroscopy of these targets with the Exo-C telescope will be 10 days each. Speckle stability will allow these long integrations to take place without interruptions to retune the stellar wavefront. A speckle stability timescale of  $\sim 48$  hours is a good compromise between operational requirements (the need to break observing sequences for momentum dumps and downlinks) and excessive overheads for frequent wavefront retuning.

**Spillover light from binary stellar companions.** Exo-C will only be able to resolve a limited number of habitable zones ( $T_{\text{eff}} = 300 \text{ K}$ ) around nearby stars. The best targets will be the two components of the alpha Centauri binary system, the closest Sun-like stars whose habitable zones are located at  $\sim 0.6''$  separation. At the time of Exo-C's launch, the apparent separation of these two stars will be  $\sim 8''$  and increasing slowly through the mission to  $\sim 10''$ . Because these two stars are so bright ( $V = -0.1, 1.3$ ), residual starlight will dominate all other backgrounds against which planets might be detected. In addition to the above requirements on speckle

brightness and stability around a single star, we also require that spillover light from the other system components at 8"–10" separation be at or below  $10^{-9}$  level of residual speckles in the coronagraphic dark field. This requirement will be met by minimizing mirror scatter at this field angle, simultaneously controlling diffraction from both stellar components, and baffling to suppress stray light and internal reflections.

#### 4.3.1.2 Spatial Fields of View

**IWA of coronagraphic dark field.** Exoplanet orbit sizes and the distances to nearby star targets combine to define the expected angular separation of a planet from its host star. The closer an imager can look to a bright star and still resolve the image of an exoplanet, the more planets and stellar targets can be examined. The IWA defines the science capability of the Exo-C mission more than any other single parameter. To enable spectroscopy of at least 10 known, nearby exoplanets, an IWA of 0.25" is required at 900 nm, or 0.125" at 450 nm. This corresponds to  $2\lambda/D$  for a 1.5-m aperture. The uncontrolled speckle contrast and stability requirements stated above should be satisfied at the IWA.

**OWA of coronagraphic dark field.** The known exoplanet target with the largest angular separation from its host star is Epsilon Eridani b at 1.06". This putative object is thought to have an orbital eccentricity of 0.3; thus to image it at its maximum elongation, an OWA of at least 1.4" is required. A more stringent requirement comes from circumstellar disk imaging, where the OWA determines whether the full extent of the disk can be imaged or only its inner regions. For the 113 debris disks within 50 pc identified by Spitzer, seventy have an estimated outer radius of 2.6" or smaller. To enable study of this debris disk sample, we therefore require an OWA of this size or larger at 900 nm. This corresponds to  $21\lambda/D$  for a 1.5-m aperture. This OWA will also be sufficient to encompass the outer radii of most of the protoplanetary

disks in nearby star-forming regions. Larger OWAs would be highly desirable, as the largest debris disks are also the closest ones that can be studied at the highest linear resolution.

#### 4.3.1.3 Astrometry

**Astrometric accuracy.** Exo-C is required to measure the orbital elements for all planets that it detects. For planets previously detected by RV, the orbit inclination will be the only unknown element. For planets newly discovered by Exo-C, all six orbital elements must be determined; however, the semi-major axis and eccentricity will be of most interest. Exo-C planet searches are most likely to discover new objects a few AU from their host stars. For a fiducial target at 10 pc distance, this corresponds to an angular separation of  $\sim 0.3$ ". To measure their semi-major axis to 10% accuracy and eccentricities  $\geq 0.1$ , the planet centroid must be measured relative to the central star to an accuracy of 30 mas or better. This capability also allows common proper motion of a candidate planet to be established with a second epoch 3 months after the first, for a star at 20 pc distance. To support this astrometric precision, a means must be provided for measuring the stellar position simultaneously with that of the planet over nine orders of magnitude of dynamic range. Furthermore, the planet must be detected with sufficient signal-to-noise (S/N) such that the statistical uncertainty in its centroid position  $\sim$  full-width, half-maximum (FWHM)/(S/N) is below the 30 mas level.

#### 4.3.1.4 Polarimetry

Planetary atmospheres and interplanetary dust particles produce scattered light with significant polarization signatures. To first order the observed polarization amplitude is a function of the scattering angle. When the latter is known, the observed polarization can provide constraints on the particle properties. For the brighter planets and disks, Exo-C should be capable of measuring linear polarizations of  $\sim 10\%$ .

### 4.3.2 Spectroscopic Requirements

Exo-C is a mission of spectroscopic characterization and exploration, and the spectrometer should be as capable and versatile as possible to measure both expected and unexpected spectral features. For smaller planets, the optimal wavelength range for characterization is between 0.45 and 1.0  $\mu\text{m}$ , a resolving power of  $R \sim 70$  is required to obtain spectroscopy of the brightest and most promising targets, and S/N of close to 10 is required to observe the features expected in Earth-like atmospheres.

Figure 4.3-1 depicts the same giant planet spectra shown in Figure 4.2-3 but convolved to  $R = 70$ . At this spectral resolution the important methane absorption features are still cleanly detectable as well as the continua between absorption bands. At lower spectral resolution the band depths become more difficult to measure against the continuum and the distinction between the various spectra begins to be more difficult to discern.

The wavelength range selected for photometric detection and characterization is 450–1000 nm. This wavelength range encompasses many molecular absorption bands of varying strengths of methane, water, and ammonia. The long wavelength cutoff is chosen to allow some detection of continuum on the red side of the 940 nm water band and the short wavelength cutoff is motivated by the relatively bland Rayleigh and haze-scattering spectrum expected in the blue for giant planets. This wavelength range can then be further subdivided for photometric and spectroscopic planetary characterization.

Solar System giant planet spectrophotometry typically relies on images taken in a variety of narrow and wide filter bandpasses centered on methane absorption bands and nearby continuum (Barnet et al. 1992). A comparable set of narrow and broad photometric filters matched to expected giant planet spectral features should be carried. One possible selection of broad filters that would be

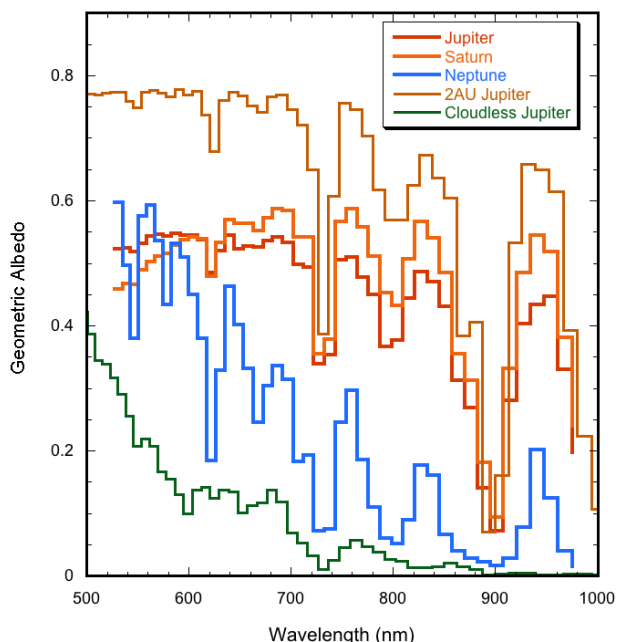


**Figure 4.3-1.** Geometric albedo spectra of real and model planets convolved to  $R = 70$  spectral resolution. Shown are Jupiter, Saturn, and Neptune (all from Karkoschka 1999), along with two model planets (from Cahoy et al. 2010), a Jupiter at 2 AU and 0.8 AU, both with three times enhancement in heavy elements. The 2-AU planet is very bright, dominated by water clouds, while the 0.8 AU is relatively dark and cloudless.

appropriate for 10% photometry is given in Table 4.3-1.

**Table 4.3-1.** Draft bandpass (10% width) for photometric characterization.

Bandpass (nm)	Comment
450–500	Rayleigh + weak CH <sub>4</sub>
510–570	Weak CH <sub>4</sub>
600–660	Weak/medium CH <sub>4</sub> & NH <sub>3</sub>
695–765	Intermediate CH <sub>4</sub> & H <sub>2</sub> O
850–940	Strong CH <sub>4</sub> & H <sub>2</sub> O

Spectroscopy with nulling over 20% wide coronagraph bandpasses implies four masks correcting over the 495–1000 nm wavelength range. The boundaries of each spectral subregion must be chosen carefully to allow for spectral overlaps to aid stitching of spectra while avoiding placing boundaries in the midst of strong absorption bands. Four bandpasses that are acceptable for both giant and terrestrial planet characterization are shown in Table 4.3-2.

**Table 4.3-2.** Draft 20% spectroscopic passbands for coronagraph mask design.

Band Center (nm)	Range
550	495–605
650	585–715
780	700–860
910	820–1000

For spectral characterization, a spectral resolution of  $R \sim 70$  was chosen as the minimum required to detect and characterize methane bands with a variety of strengths, as well as the water band at 940 nm for Jovian planets. Additionally,  $R \sim 70$  is optimal for detecting the O<sub>2</sub> A-band at 760 nm, a potential biosignature, should a super-Earth planet be found in the habitable zone of one of the stars in the alpha Centauri system.

Clearly obtaining spectra at this resolution on all planets detected by Exo-C will not be possible, but having this capability to characterize the brightest and best-placed planets will be crucial for characterizing the range of solar neighborhood planets, and in particular for searching for signs of life on the closest extrasolar planets to the Earth.

We then must consider the SNR required to meaningfully characterize these planets. A bare minimum requirement for giants is to be able to distinguish gas giants with Jupiter-like methane abundance from gas giants with 10× greater methane. We find that at  $R \sim 25$  the best bands for distinguishing these two classes of planets are those at 530 and 660 nm. In Jupiter- and Saturn-like planets, these bands are weak, while in Uranus- and Neptune-like they are quite strong. The 660-nm band depth is about 50% of the continuum flux level. To distinguish the presence of this band to  $3\sigma$  thus requires that the continuum flux level be measured from 600–700 nm at  $S/N \sim 6$ . Note, however, that since Uranus’s radius is about 1/3 that of Jupiter’s it reflects only 11% of the light. Thus the capability to obtain  $S/N \sim 6$  spectra of an ice giant is a much stricter requirement than  $S/N \sim 6$  for a gas giant.

Our second requirement is to be able to measure the degree of methane enhancement in a gas giant within 50%. This requires measuring the depths of the several methane absorption features relative to the continuum and is similar to the problem of distinguishing the reflection spectrum of Saturn from that of Jupiter. For  $R \sim 70$  this requires  $S/N \sim 10$  to uniquely characterize multiple methane bands and the associated continuum.

Detecting and measuring the water band at 940 nm will only be possible for bright gas giant planets with thin water clouds (to provide continuum-scattered flux). For a Jupiter-like planet at 2 AU, detecting a 20% deep band at  $3\sigma$  requires  $S/N \sim 20$ .

Given these considerations, we require the ability to obtain  $S/N \sim 10$  spectra of a gas giant planet at 5 AU from a solar-type star with a radius equal to that of Jupiter and  $S/N \sim 7$  spectra of a similar ice giant planet with a radius equal to that of Neptune. For a favorable Jupiter-like planet at 2 AU, we require the ability to measure the red spectrum, including the 940 nm water band and associated continuum to  $S/N \sim 20$ .

In summary the requirements are:

1. Spectral range 450 to 1000 nm
2. Spectral resolution  $R \sim 70$
3. Spectral  $S/N \sim 10$  on Jupiter twin at 5 AU
4. Spectral  $S/N \sim 7$  on Uranus at 5 AU
5. Spectral  $S/N \sim 20$  on “best case” Jupiter at 2 AU

#### 4.3.2.3 Wavelength Range

The required spectral range for small planets is 0.45–1.0  $\mu\text{m}$ . This wavelength range encompasses absorption from CH<sub>4</sub>, NH<sub>3</sub>, H<sub>2</sub>O, O<sub>2</sub>, and O<sub>3</sub>. It also includes shorter wavelengths that can be strongly Rayleigh scattered in planetary atmospheres or absorbed by planetary surfaces. This wavelength range will allow us to discriminate between reducing atmospheres like those seen on the ice giants in our Solar System, and oxygen and water-

dominated atmospheres like the Earth's, as well as to search for biosignature gases.

The short wavelength cutoff is selected to allow detection of continuum on the short wavelength side of the ozone Chappuis band from 0.5–0.7  $\mu\text{m}$  for super-Earth planets. Detection of ozone would help constrain the bulk and oxidation state of the atmosphere and indicate the presence of a surface UV shield for life. Large amounts of ozone can be considered a potential biosignature as long as abiotic sources of ozone can be ruled out via knowledge of the star's spectral energy distribution (SED), and the presence of other oxygen bearing gases in the atmosphere. The short wavelength cutoff also provides a region from 0.45–0.6  $\mu\text{m}$  in which to detect Rayleigh and other forms of scattering from gases and particles in the planetary atmosphere. Because scattering is more pronounced at shorter wavelengths, the strongest deviation from a nonscattering atmosphere will be more readily detected at these shorter wavelengths.

The long wavelength cutoff is required for detection of the 0.94  $\mu\text{m}$  H<sub>2</sub>O band. This is the strongest water band in terrestrial atmospheres, and in fact often the strongest feature in the spectrum. On planets with reducing atmospheres, as may be the case for mini-Neptunes, this water band is also the cleanest band, as the shorter wavelength H<sub>2</sub>O bands are often combined with CH<sub>4</sub>. The extension of the spectrum to 1.0  $\mu\text{m}$  is required for measuring continuum on the long-wavelength side of the water band, which is needed for accurately quantifying the water feature.

#### 4.3.2.4 Spectral Resolving Power

The required spectral resolving power is  $\geq 70$  at 0.63  $\mu\text{m}$ , which must be achieved for the very brightest targets. We also require sufficient control of detector systematics that it is feasible to bin down in resolution to increase S/N for our fainter targets. The number of molecular features in exoplanet spectra increases with wavelength, so it is highly desirable that the resolving power scales with

wavelength, such that larger resolving powers are obtained at longer wavelengths. At spectral resolving powers below 70, many features of interest are contained in only one resolution element, making robust detection and quantification extremely difficult. The choice of 70 for the brightest targets is set by the width of the O<sub>2</sub> band and by the width of the continuum between water bands for Earth-like atmospheres. The simulated spectrum for a realistic (with clouds) Earth-like planet with resolving power of R = 20, 50, and 70 is shown in Figure 4.3-2. Similar spectra for simulated super-Earth spectra at R = 20 and R = 50 are shown in Figure 4.3-3. R = 70 is also the pivotal resolution above which very little is gained in S/N benefits for the targeted absorption features, and below which S/N for these features starts to degrade significantly (see Figure 4.3-4).

#### 4.3.2.5 Signal-to-Noise Requirements

In Figure 4.3-4, we show a plot of SNR required as a function of spectral resolving power for O<sub>2</sub> and H<sub>2</sub>O features in an Earth-like planetary atmosphere. For the realistic Earth case sampled with constant-width wavelength bins that give R = 70 at 630 nm, we see that we would need a S/N of  $\sim 3$  to detect the H<sub>2</sub>O 0.94  $\mu\text{m}$  band at the 3- $\sigma$  level, and a S/N of  $\sim 7$  to

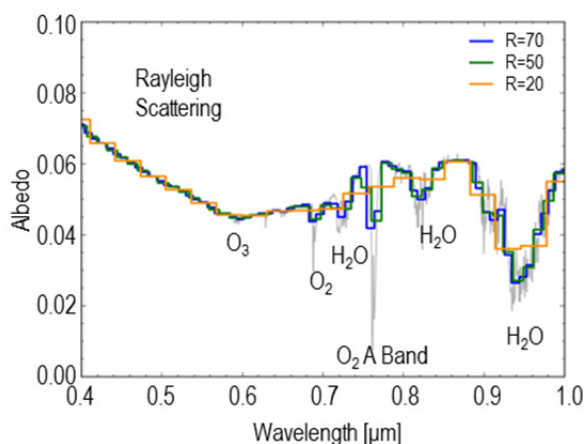


**Figure 4.3-2:** A realistic Earth spectrum (grey) degraded to spectral resolutions of R = 20, 50, and 70. The oxygen A-band is seen at 0.76  $\mu\text{m}$ , and the strongest water vapor band in this spectral wavelength range is seen at 0.94  $\mu\text{m}$ .

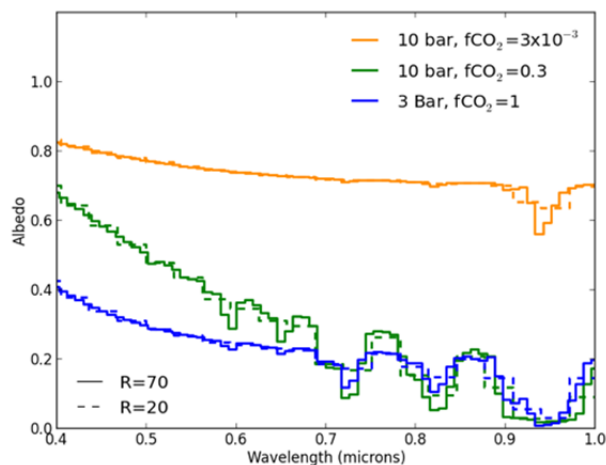


**Figure 4.3-3.** Simulated spectra of super-Earth atmospheres with different total pressures and amounts of CO<sub>2</sub> and water vapor. Note the change in Rayleigh scattering slope between 0.4–0.6 microns for different total pressures and CO<sub>2</sub> fractions.

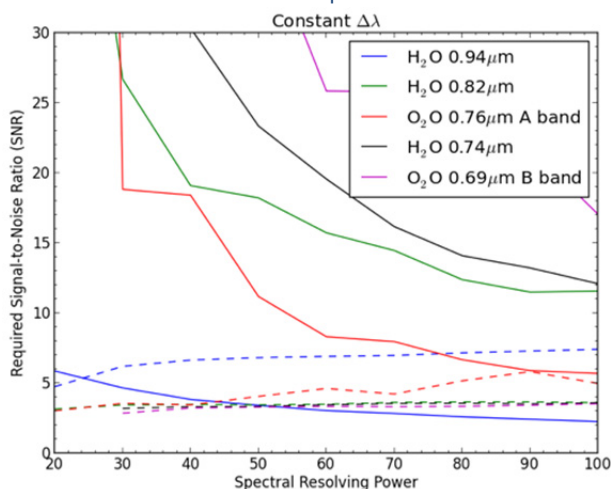


**Figure 4.3-4.** Spectral S/N required as a function of spectral resolving power for water and molecular oxygen in the albedo spectrum of an Earth-like atmosphere. The solid lines are for detection of a feature, and is specifically detection of a deviation from the surrounding continuum with a 3- $\sigma$  confidence level at the wavelength position of the absorption feature. The dashed lines are for measuring the bottom of the absorption band to 3- $\sigma$ , which is required to assist in the quantification of a molecular constituent. For broad, shallow bands, it may be that quantifying the bottom of the band, which will be at a relatively high albedo/flux level, will require less S/N than discriminating it from the surrounding continuum.

detect the bottom of this band to 3- $\sigma$ . To obtain the continuum on the longward side of the water band, we would need a S/N of 6 for a 3- $\sigma$  result and a S/N of 10 for a 5- $\sigma$  result. To obtain another, weaker, water band as a

confirmation of water detection, would require S/N close to 15 (this S/N would rise to 19 for R = 50). To detect the O<sub>2</sub> A band, we would need a S/N close to 8, which would rise to 11 at R ~ 50). For a 10-bar atmosphere on a CO<sub>2</sub> and water-dominated world, we would need a S/N of ~ 8 to discriminate the 0.94  $\mu$ m band from the adjacent methane band to help distinguish between a reducing and oxidizing atmosphere.

In summary, an S/N of ~ 10 across the 0.9–1.0  $\mu$ m region would provide 5- $\sigma$  confidence for the detection of the bottom of the water band and the continuum on either side of it. This S/N obtained from 0.7–0.9  $\mu$ m would also allow us to potentially obtain the O<sub>2</sub> A-band at 0.76  $\mu$ m, which is a potential biosignature.

### 4.3.3 Mission Lifetime

The Exo-C mission should be of sufficient duration to carry out the following science programs: (1) spectroscopy of at least 10 known, nearby planets; (2) meaningful searches of at least 100 nearby stars for planets beyond the limits of previous detection surveys; and (3) imaging surveys of several hundred circumstellar disks. The second program includes imaging searches for objects with the orbital period of Jupiter at multiple epochs. To maximize the completeness of a search for objects with 12-year orbital periods, images at two epochs separated by almost 3 years is required; this will allow a planet that happened to be at stellar conjunction at the first observation epoch to move through 90° of orbital longitude to elongation at the second epoch and be detected. A minimum mission lifetime of 3 years is therefore required.

## 4.4 Derived Instrument Requirements

### 4.4.1 Overview

The instrument requirements presented in this section encapsulate the wide range of exoplanet and disk objectives for this mission. These top-level instrument requirements are derived from the science requirements

described in §4.2 and their detailed measurement requirements described in §4.3.

#### 4.4.2 Telescope Aperture

The required inner working angle requirement and spectral bandpass conspire to set a minimum telescope diameter. The inner working angle is required to be at least  $0.250''$  at 900 nm. Coronagraph demonstrations with unobscured apertures have achieved high contrast at  $2 \lambda/D$ , but smaller angular separations are expected to be far more challenging, as those separations impose stringent pointing and coronagraph mask fabrication requirements. The diameter of the telescope must then be at least 1.5 m, as represented in Figure 4.4-1.

#### 4.4.3 Coronagraphy

The coronagraph must be used to provide point source sensitivity of  $10^{-9}$  contrast at an angular separation of  $2 \lambda/D$  ( $0.125''$  at 450 nm). There are several coronagraph architectures that can meet this requirement, all of which were considered in this study. The high-contrast coronagraphs include the hybrid Lyot, phase-induced amplitude apodization (PIAA), visible

nulling coronagraph, and the vector vortex. There is a full description of the other coronagraph designs and simulated performance in §5.1.1.5. The hybrid Lyot, PIAA, and vector vortex all meet the mission requirements. Following the interim report, a more detailed analysis will be conducted in order to trade the coronagraph performance (e.g., inner working angle, contrast, and throughput) against the science metrics and technology readiness, as described in §9.

#### 4.4.4 Wavefront Control

A wavefront control system must be used in order to correct wavefront aberrations that degrade contrast in the optical system. The deformable mirrors must be able to provide high contrast from the IWA ( $\sim 2 \lambda/D$ ) to the OWA ( $\sim 22 \lambda/D$ ) as described in §4.3.1.2. The high contrast regions must be corrected on both sides of the image plane, and therefore, two deformable mirrors must be employed. The operational plan and detailed wavefront control sequences will be explored for the final report.

The 30 mas relative astrometric precision required for orbital motion characterization corresponds to a pixel. Fiducial markers will be generated in the science camera FOV by applying specific spatial frequencies on the deformable mirror, causing a small amount of starlight to “leak” onto the science detector. Centroiding on these “leaked” DM-generated spots will be used to locate the center of the star behind the coronagraph to high accuracy. The astrometric position of the exoplanet will be measured from this location.

#### 4.4.5 Stray Light

The science requirement to achieve high contrast on binary stars places requirements on stray light control. For example, the binary alpha Centauri will have a separation between  $\sim 8$  and  $12$  arcsec during the lifetime of Exo-C (Figure 4.4-2). Coronagraphic masks can reduce the stray light. However, the coronagraph fore-optics can generate

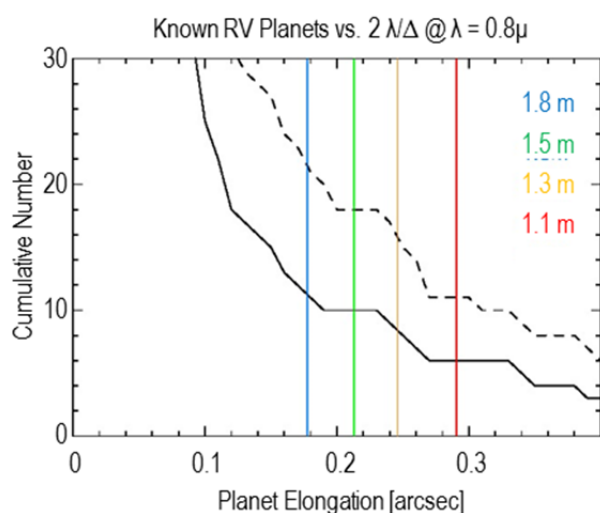


**Figure 4.4-1.** Cumulative number of RV planets known in early 2014 that can be accessed outside the telescope inner working angle, as a function of aperture size. The solid line shows planets with expected brightness greater than  $V = 29$ , and the dashed line all planets.

aberrations that are not occulted by the mask design. This will place requirements on the high-frequency errors on the optics upstream from the coronagraph. For light that passes through the coronagraph, baffling and wavefront control schemes will be used to further suppress the starlight.

#### 4.4.6 Imaging

The measurement at the image plane of the science camera must be at least Nyquist sampled at the diffraction limit for the shortest wavelength (i.e., 450 nm). This critical sampling will result in the fewest number of detector pixels that are required for the mission. The science camera detector will also be integrated into the wavefront control architecture. It will serve as a focal plane wavefront sensor that will be used to estimate aberrations.

The science requires that the field sample the entire dark hole at the longest wavelength (i.e., 1000 nm), which at the longest wavelength,  $\lambda/D$  is 130 mas.

#### 4.4.7 Spectroscopy

The full spectral range of the science camera should cover at least 450–1000 nm. This full spectral coverage is not required to be measured simultaneously. The instantaneous spectral bandpass should be no less than 20%. This requirement is necessary to measure broad spectral features and adjacent continuum spectra within the same dataset. Furthermore, this bandpass will enable multiple adjacent spectra to be overlapped together for subsequent merging. The full spectral coverage combined with the instantaneous spectral coverage means that, at minimum, four separate

instantaneous bandpasses would be required for the spectrograph.

The instantaneous spectral coverage could be limited by the broadband contrast achievable with the selected coronagraph technique. Coronagraphs experience optical chromatic effects that degrade contrast spectral when expanding to larger bandpasses. To date, the broadband laboratory demonstrations have been limited to 20%.

The spectral resolution shall be greater than  $R \sim 70 (\lambda/\Delta\lambda)$  across the entire spectral bandpass. This spectral resolution means that at the shortest wavelength, each spectral resolution element on the detector should be no more than 6.42 nm (450 nm/70).

The spectrophotometric precision of the instrument should be 0.06 mag (5%) with respect to the central star. This level of spectrophotometric precision ensures that high S/N spectroscopy ( $S/N \sim 20$ ) is not limited by the spectrophotometric precision. The

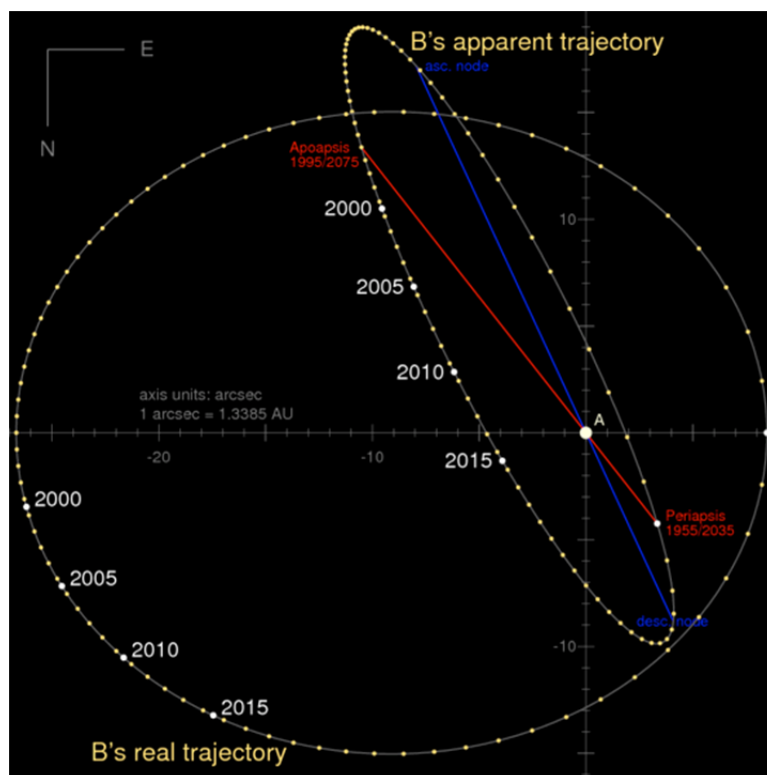


**Figure 4.4-2** The orbital separation of the alpha Centauri binary system sets the requirement for stray light suppression between 8 and 10 arcseconds.

spectrograph must be able to maintain an intrascene contrast of  $10^3$ .

#### 4.4.8 Detectors

The baseline detector must cover the entire spectral bandpass from 450–1000 nm. The quantum efficiency must be high across the entire bandpass in order to meet the sensitivity requirement defined in §4.3.2.5, but the exact requirement is dependent on the coronagraph choice. A deep depletion silicon detector would meet these requirements. The specific detector performance requirements for read and dark noise are dependent on the system throughput and the length of the science integration times. In addition to reaching saturation, detector integration times may be limited by cosmic ray impacts. The design team is investigating the radiation environment in an Earth-trailing orbit to determine the cosmic ray exposure time limit to impose on the mission. A conventional charge coupled device (CCD) with an analog register has high heritage and could in principle meet the science requirements if long integration times are acceptable. Electron-Multiplying CCDs (EMCCDs) could meet more challenging read and dark noise requirements. A full system and detector trade study will be completed to determine the highest performing, lowest risk, and cost compliant implementation.

#### 4.4.9 Baseline Instrument Concept

Exo-C has baselined a lenslet-based integral field spectrograph to meet the requirements specified in §4.4.7. The design will accommodate some spectral overlap between the different bandpass filters. In addition to the IFS, Exo-C will have an imaging camera for target acquisition and circumstellar disk science.

#### 4.5 Mission Lifetime Science Observations Budget

Science observations are governed by science objectives and fall into three categories: (1) Spectroscopy of Known Exoplanets, (2) Planet

Discovery Surveys, and (3) Disk Imaging Surveys. Planets discovered by the survey also become candidates for spectroscopy. We have estimated the duration required to conduct mission operations in support of these science objectives. The detailed discussion, along with duration justifications, are described in §7. The mission operations and summary time budget is shown in Table 4.5-1. In the *Visits* columns, we estimate the number of targets and number of revisits per target in each category. *Total Observe Time* is calculated by multiplying the *number of targets*, *number of visits*, and the *integration time per visit*. *Nonobserving Time* consists of spacecraft management; retargeting, dominated by thermal stabilization of the observatory; and instrument optimization, i.e., tuning the Deformable Mirror to obtain the required contrast. Nominal spacecraft management consists of weekly telecom passes and momentum management events. Multiple observations will occur during a week (see §7), therefore in Table 4.5-1 we assign a portion of weekly spacecraft management time to each observation, roughly proportional to its duration.

Based on our mission lifetime science observations budget, we expect to observe spectra of 20 known exoplanets, survey 20 nearby stars for super-Earths, and search 140 nearby stellar systems for the presence of giant planets. We also expect to conduct 300 disk-imaging surveys in the subcategories shown in Table 4.5-1.

#### 4.6 Science Requirements Flow-Down

The science requirements from §4.3, along with the derived top-level instrument requirements from §4.4, will form the Level 1 science requirements for the Exo-C mission.

##### 4.6.1 Science Requirements to Mission Requirements

The STDT members are involved in flowing each science goal into the top-level mission requirements. The union of these requirements is then taken to form a complete set of mission

**Table 4.5-1.** The table represents a notional science allocation of the 3-year lifetime. Each science type has its associated downlink, thermal stabilization, and optimization times, which are captured in observing efficiency (last column).

Science Type	Visits		Science Observation Times		Total Mission Time	Observation Efficiency
	# of Visits	Average # of Visits	Average Integration Time/Visit	Total Observation Time per Science Type		
	$N_{target}$	$N_{visit}$	$t_I$ (hrs)	$T_{Obs} = N_{Target} \cdot t \cdot N_{visit} \cdot t_I$ (days)		
<b>Planet characterizations</b>						
Spectroscopy of known exoplanets (known from RV and Exo-C survey)	20	1	200	167	193	87%
Multicolor photometry of known exoplanets (known from RV and Exo-C survey)	20	1	20	17	43	39%
<b>Planet discovery surveys</b>						
Survey nearby stars for Super-Earths within the habitable zone	20	6	20	100	150	67%
Search for giant planets around nearby stars	140	3	20	350	525	67%
<b>Disk imaging surveys</b>						
Detection survey in RV planet systems	60	1	12	30	40	75%
Known debris within 40 pc	60	1	6	15	24	63%
Young debris disks from Wide-field Infrared Survey Explorer (WISE)	100	1	6	25	40	63%
Nearby protoplanetary disks	80	1	6	20	32	63%
<b>Total on-orbit ops time</b>				723	1045	
Initial on-orbit checkout (days)					60	
Total (days)					1105	65%
<b>Total (years)</b>					<b>3.0</b>	

requirements, which are used by the Science Team in the observatory performance simulations.

#### 4.6.2 Flight System Requirements

Flight system requirements are those that affect both the payload and spacecraft. Requirements only affecting either the payload or the spacecraft flow directly to that subsystem. We have focused on flow of the mission requirements into the flight system-level requirements, and will address other systems (e.g., ground data system (GDS) and mission operations system (MOS)) in the final report.

#### 4.6.3 Payload Requirements

Most of the science requirements lead to payload requirements, since this is where the coronagraph resides, affecting the coronagraph architecture trade (see §5.1.1.6). Notably, the science requirements lead to the telescope aperture choice, which is a major driver.

#### 4.6.4 Spacecraft Requirements

For the spacecraft, the top two driving requirements are jitter and pointing. The jitter requirement has resulted in a two-layer isolation system, and the pointing requirement has resulted in the multi-layer control architecture (see §6.7.2).

#### 4.7 Top-level Description of the Instrument and Mission

The system consists of several functional subsystems, as shown in Figure 4.7-1. Light is collected by a telescope, which is then passed into the instrument assembly. The electronics module controls the various sensors and mechanisms within the instrument, while the thermal control system (temperature sensors, heaters, control electronics, blankets, thermal links, radiators) maintains a stable temperature environment for all of these elements. The electronics module also routes power and signals from, and data to, the spacecraft. The entire optical system is dynamically isolated from the spacecraft to minimize externally induced perturbations, which would degrade instrument performance.

The basic function of the system is to permit the direct imaging of objects of interest

(planets, dust) surrounding stars. The root technical problem is twofold: first, the objects appear substantially fainter than the star they orbit, and second, the direct image of the star itself spreads out considerably due to physical processes in both light propagation (diffraction, scattering) and in detection (blooming, image smear), thereby overlapping the light coming from the objects of interest. Thus, by efficiently blocking the starlight from reaching the detector while allowing the light from the objects of interest to be effectively unimpeded, the objects of interest may be directly imaged. The general class of instrumentation that performs this function is the coronagraph; for this mission, the coronagraph is required to reduce (suppress) the starlight to a level of  $10^{-9}$  or better.

In order to achieve the suppression level required, the coronagraph needs to have a

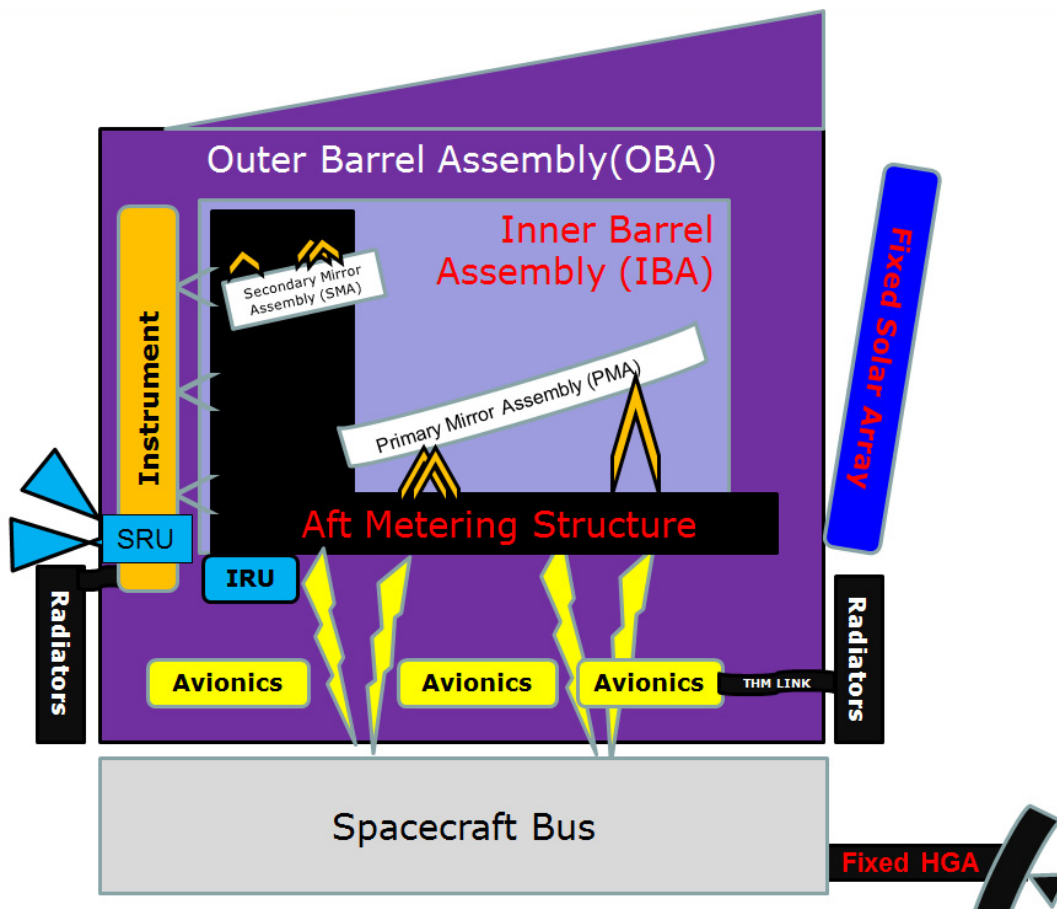


**Figure 4.7-1.** The block diagram shows a high-level layout of the Exo-C payload and spacecraft, with locations and identification of the major sub-assemblies.

wavefront that is extraordinarily well corrected and stable. As such, minute irregularities in the surface figure, coatings, or alignment that occur due to manufacturing, assembly alignment, ground-to-orbit, or on-orbit environmental perturbations must be compensated. This is accomplished by a control system just ahead of the coronagraph that monitors and corrects subtle variations in the wavefront properties. Further, the system performance is sensitive to drifts in the spacecraft base-body pointing during the course of an observation; a pointing control system within the instrument senses this and corrects for it via internal compensations.

The other system function is to characterize the spectra of the light coming from the detected objects of interest. For the spectral resolution required ( $R \sim 70$ ), the general class of instrumentation is the spectrometer. Efficient use of observation time is accomplished by obtaining the spectra from multiple objects of interest simultaneously.

The spacecraft and the mission plan are both designed around providing a stable environment for the instrument to function to its best capability. This means, to the best possible levels, minimal dynamic disturbances and minimal thermal variations to the instrument during the course of an observation. On the spacecraft side, this is accomplished with a body-fixed solar array and high-gain antenna; the only moving parts are the reaction

wheels required to maintain pointing stability. An earth-trailing solar orbit puts the system in as stable a thermal environment as possible, the only changes being those due to changing solar angle as the spacecraft slews for operational demands (retargeting or telecom).

Retargeting effects will be minimized by careful planning. Using the results from prior missions and ground observations, a list of star systems will be identified for study. This list will be prioritized, and sequenced such that minimal solar angle changes are experienced with each slew between successive targets. With minimized solar angle changes, thermal perturbations are minimized, and thermal control can bring the system back into optimal conditions for observations in minimal time. This maximizes the time spent on science data collection over the course of a 3-year mission lifetime.

The 3-year mission allows multiple revisits to selected targets. This yields data on planet positions over time that allows for orbital parameter determinations. It also expands the opportunities for observation of planets that initially appeared too close to the star for discovery; as their orbits appear to move them farther out from the star (increased planet-star separation angles from our vantage point), they move beyond the instrument IWA and into the zone where direct imaging can be accomplished.

## 5 Architecture Trades

### 5.1 Payload Trades

The focus of the JPL design team for the first 9 months was to conduct and complete the primary trade studies that drive the general mission architecture. The JPL design team was established and met in July 2013 and generated a detailed trade list that would be assessed for the interim report. The focus of the design team for the interim report was to establish a baseline and complete the trades necessary to have the system hold together technically. After the interim report, the design team will focus on refining the design through detailed optical, mechanical, and thermal modeling as documented in §10. The first trades that were conducted were related to the optical architecture and design. All mechanical and thermal trades were conducted once the optical architecture yielded a system that maximized performance and efficiency. Each of the major functional engineering areas had related trades that progressed to more detail at the subsystem and assembly levels. Many of the trades were coupled and contained a large trade space,

such as the pointing control architecture and the S/C bus trade. The design team conducted trades that affected the payload, spacecraft, and mission-level aspects. Table 5.1-1 contains a listing of trades and their current status. This section provides a summary of the major trades and recommended solutions.

#### 5.1.1 Optical

##### 5.1.1.1 Obscured versus Unobscured Configuration

A study was performed that evaluated the merits/impacts of obscured versus unobscured aperture forms for a coronagraph instrument. Only technical and performance aspects were examined, independent of cost and schedule considerations. From a performance perspective, the use of an *unobscured telescope form for a coronagraph is preferred*. The two main factors involved in determining this were collecting area and integration time, both of which significantly favored the unobscured form. Five other factors were examined (polarization influence, fabrication complexity, structural considerations, optical design complexity, and binary target performance) that either yielded no net

**Table.5.1-1. Completed trades**

Trade	Outcome
Telescope obscured vs. unobscured	Unobscured
Telescope design	Cassegrain
Primary mirror material	Low CTE glass
Orbit	Earth-trailing
Aperture size	1.5 meter
High-gain antenna (HGA)	Fixed
Instrument bench configuration	Lateral
Low-order wavefront sensor (LOWFS) design	Zernike Low-order Wavefront Sensor (ZLOWS)
Spacecraft bus	Kepler type
Solar array configuration	Fixed
Mission lifetime	3 years
Pointing architecture	Isolation, flight management system (FMS), payload, and spacecraft interface
Spectral measurement technique	Integral field spectrometer (IFS)
Telescope stability—thermal architecture	Heater control on inner barrel, outer barrel, and primary mirror assemblies
Secondary mirror configuration	Actuated secondary
Aft metering structure configuration	Integrated inner barrel assembly
Instrument architecture	Fine-guidance sensor (FGS), LOWFS, Coronagraph, filters, IFS

distinction or only very weakly favored one form over the other.

### 5.1.1.2 Instrument Bench Configuration

#### 5.1.1.2.1 Summary

Two basic configurations were examined to accommodate the coronagraph instrument. A lateral configuration, which places the instrument parallel and offset to the telescope axis was selected for its ability to fulfill all desired functions while providing for best overall performance with a minimum total count and lowest angles of incidence on critical optical surfaces. The resulting configuration is shown in Figures 5.1-1 and 5.1-2

This configuration was developed further to include mechanism representations to visualize clearances around the light paths. In the process of sketching out the filter wheel mechanism (Figure 5.1-3), it became apparent that a second filter wheel would be needed to perform all desired functions while keeping the

wheel diameter manageable, hence the presence of “Filter Set 1” and “Filter Set 2” ahead of the imaging detector.

### 5.1.1.3 Aperture Size

#### 5.1.1.3.1 Summary and Recommendation

Several factors were studied in the trade that set the baseline clear aperture. Since science only improves with aperture size, available resources set the upper limit. Of those, mass was not a limitation because we have ample mass margin with respect to the launch vehicle capability. Because of that, cost is the dominant driver for the upper limit of the aperture size. The current baseline is set at 1.5 m.

#### 5.1.1.3.2 Introduction of Trade

The science performance clearly increases with aperture size, since it increases the light collected. More important, the clear aperture size for a coronagraph sets the inner working angle (IWA). This in turn directly affects the number of known radial velocity (RV)

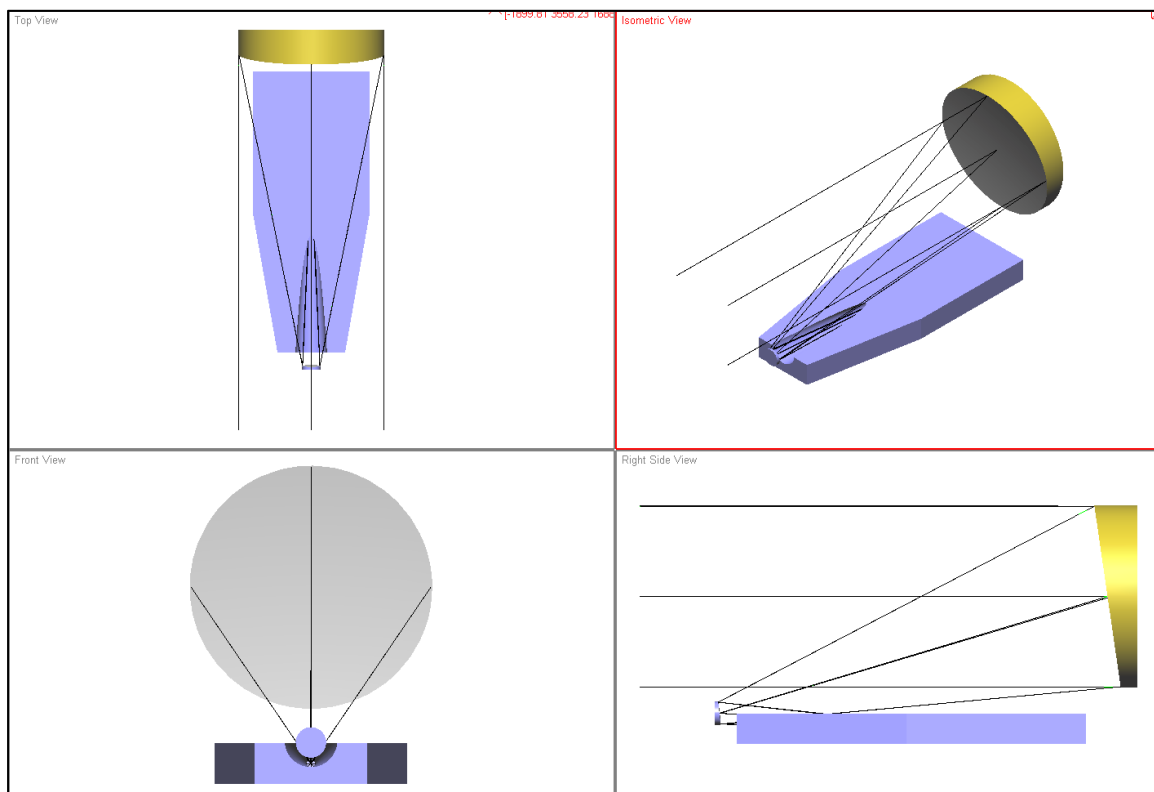


**Figure 5.1-1.** “Lateral” configuration. The instrument bench was placed parallel to the telescope primary-secondary axis, which eliminated the need for an initial 90° fold mirror and provided ample volume for packaging the optical system.

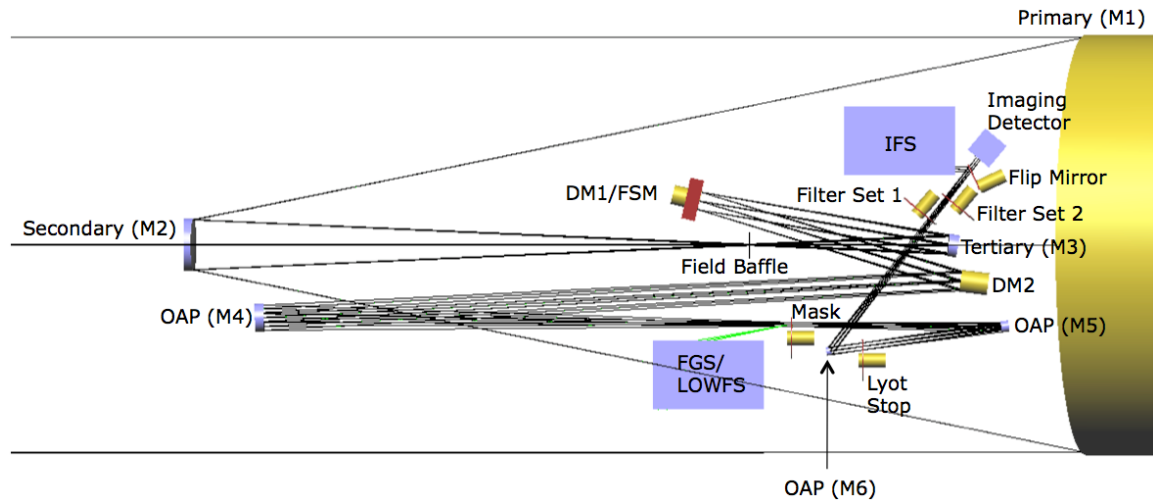


**Figure 5.1-2.** “Lateral” configuration, top view. This configuration incorporates the desirable properties of (1) Fold mirrors are eliminated. (2) All sensitive elements have low AOIs. (3) Significant clear volumes exist in this plane to accommodate the FGS/LOWFS, IFS, and an auxiliary instrument.

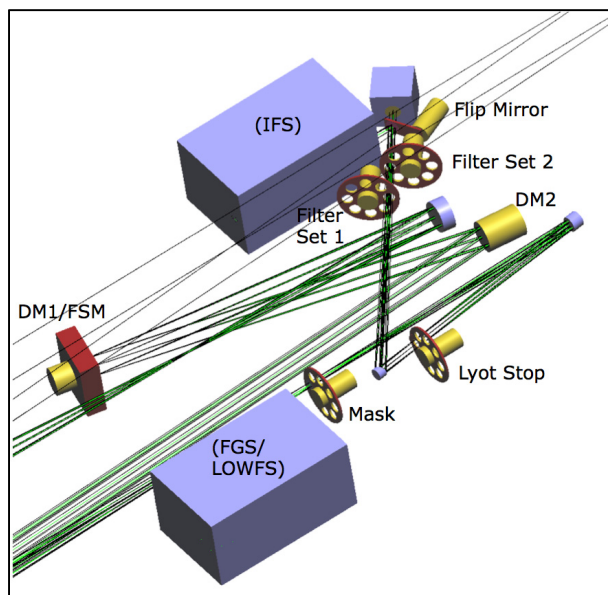


**Figure 5.1-3.** “Lateral” configuration, detail of mechanism and subassembly allocations, isometric view. The eight-slot wheel capacity was defined by the minimum slot diameter to pass the light beam and the maximum wheel diameter that would package into the allocated mechanical envelope; this resulted in the use of two filter wheels to provide sufficient slots to carry a presumed complement of filters.

exoplanets for which Exo-C is able to obtain spectra, and the number of Super-Earths that Exo-C would be capable of detecting.

### 5.1.1.3.3 Assessment of Factors

#### Integration Time

The integration time needed per target decreases as the clear aperture diameter increases. This can therefore be traded with lifetime, or throughput. Thus, this is not that strong a driver toward larger aperture size.

#### Inner Working Angle

IWA goes as  $\sim 2\lambda/D$ . Since the detectors and system throughput will limit the short wavelengths, this is fixed at  $\sim 450$  nm. Hence, an increase in diameter directly affects how close to the star we can detect or characterize exoplanets. There is no other parameter to trade for diameter, as there is with integration time, and hence the IWA becomes a very strong driver. Figure 5.1-4 shows the number of known RV exoplanets that can be characterized as a function of clear aperture diameter. Note that the cutoff is set at  $0.8 \mu\text{m}$  so that, for these exoplanets, a spectrum from 0.45 to 0.8 microns would be measured.

From the diagram, there is a modest gain in going from 1.3 m to 1.5 m. There is little advantage in going from 1.5 m to 1.8 m since there is a flattening in that part of the accumulated targets. It would require apertures

larger than 1.8 m to dramatically increase the known RV planets that we can observe.

### Detections

Neptune to Jupiter sized planets are expected to be detectable around a few hundred nearby stars using an aperture range between 1.1 and 1.8 m; however, that is not the case for Super-Earths. Table 5.1-3 shows the number of Super-Earth planets (two Earth radii) we may expect to be detectable. This assumes a maximum of 10 days of integration time.

**Table 5.1-3.** Expected number of Super-Earth-sized planets detectable as a function of their orbital distance and telescope aperture diameter. Exo-C can probe for Super Earth-sized planets around 1 AU separation around 10 Hipparcos stars (values in black). This will hold true even if the clear aperture diameter decreases a little. Super-Earths could be accessed in a substantially larger target sample if contrasts better than  $10^{-9}$  could be achieved (values in red).

Orb Rad (AU)	1.1m	1.3m	1.5m	1.8m	Delta Mag
1	4	10	10	17	22.6
2	16	25	39	61	24.1
3	17	35	46	66	25

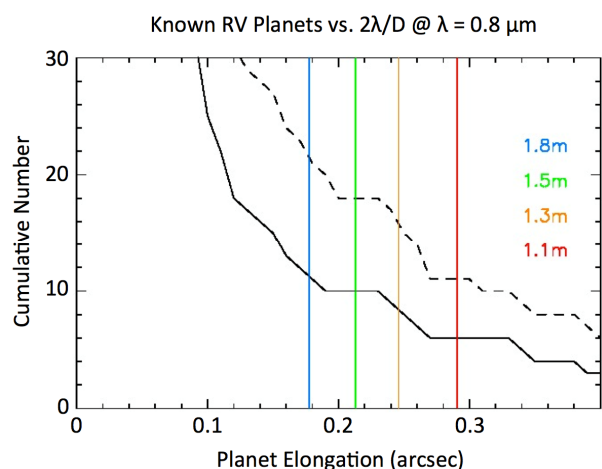


**Figure 5.1-4.** Cumulative number of known RV planets Exo-C can measure with different aperture diameters. Below 1.3 m, the presumptive science return would be minimal. Exo-C can measure the spectra of 10 known RV planets at 0.45–0.8 microns. The dashed line represents the cumulative number of known RV planets vs. separation from the parent star. The solid line only counts those with  $V \text{ mag} \leq 29$ , which is measurable by Exo-C. The vertical lines show the sensitivity vs. clear aperture diameter, indicating a small plateau around our current baseline of 1.5 m.

The table shows that for Super-Earths, 1.3-m and 1.5-m diameter apertures have comparable yields; however, at 1.1 m the sample drops to only four objects, which is below our current minimum baseline science requirement of 10. Hence, we adopt a minimum aperture diameter of 1.3 m for our science floor.

#### 5.1.1.3.4 Resources Needed

### Mass

With a clear aperture diameter of 1.5 m, our current best estimate (CBE) wet mass for the observatory is well within the capability that a low cost intermediate class launch vehicle has for an Earth-trailing orbit. Within the range of apertures being evaluated, mass will not drive the aperture choice.

### Cost

Not surprisingly, cost is the main resource restriction for aperture size. Early in this design process, Exo-C commissioned a study through JPL's Advanced Projects Design Team on aperture cost sensitivity using an earlier coronagraph mission study as a starting point. The study showed that a more complicated 1.5 m telescope with 5 years of operations was just above the Exo-C \$1B target (simplifications would later prove the answer in getting the 1.5 m design below \$1B). Designs with 1.3 m and 1.1 m apertures came in soundly below the target in the JPL Advanced Projects Design Team study. As a result, of this study, apertures larger than 1.5 m were not considered as credibly below the \$1B requirement.

#### 5.1.1.3.5 Conclusion

Given the results of the JPL Advanced Projects Design Team study and the reality of the Kepler mission—1.4 m primary mirror and 4.5 years of leading edge exoplanet discoveries for a total cost of ~\$750M FY15—Exo-C decided to baseline a 1.5 m primary mirror aperture.

### 5.1.1.4 Instrument Architecture

#### 5.1.1.4.1 Summary

A single-path instrument with selectable elements (to provide coverage over the full waveband) is baselined at this time to support initial STOP (structural, thermal, optical, performance) modeling activities. The FGS uses reflections off the starlight rejection element to maximize the fine-steering mirror (FSM) control loop rate at no impact to the science path. Spectral content is evaluated with a field spectrometer to provide the most efficient use of observing time.

#### 5.1.1.4.2 Background

Recent mission concept studies (e.g., Actively-Corrected Coronagraphs for Exoplanetary System Studies (ACCESS), DaVinci, Pupil mapping Exoplanet Coronagraphic Observer (PECO), EXoplanetary Circumstellar Environments and Disk Explorer (EXCEDE)) have documented the base coronagraphic functional approaches, with attributes, limitations, and commonalities (Lawson 2013). In summary:

There are five primary approaches, of which three (Lyot, shaped pupil, and vector vortex) share a virtually identical configuration (distinguished by the nature of the element placed in the mask plane). These three, plus the fourth (phase-induced amplitude apodization), once past the coronagraphic implementation, can have identical backends. The fifth form (visible nuller) is unique in almost all aspects, and, while not represented in the following discussion of backend options, was also considered as a coronagraph approach for this mission.

There are three areas where options are considered: science path, FGS function path, and spectrometer path. While there are multiple options for implementing each area, a single architecture needed to be identified to promote the initial analysis activity. This section describes the baseline selections made.

#### 5.1.1.4.3 Science Path

Once past the coronagraphic elements, all of the starlight rejection will have occurred, leaving a straightforward camera system to create a field image. The performance assumption made is that, based on wavelength-dependent effects, multiple discrete images in several wavebands would be required to preserve the nominal contrast ratio across a broad band. These multiple images can be captured through either multi-path/simultaneous observation or single-path/sequential observation.

Observing efficiency would be maximized if data from all wavebands of interest were collected simultaneously. However, wavefront control cannot provide adequate correction over the full bandwidth, so this would require multiple coronagraph paths from the first DM back to the detector, each path being effectively an independent instrument as illustrated in Figure 5.1-5.

Preserving the necessary conjugate relationship between the primary mirror and the FSM to control pointing and beamwalk effects in all paths would require either equal optical distances, or unique pupil reimaging optics, in each path. The technical impact of this would be extra surfaces in each path, and consequently more opportunities for energy loss and wavefront degradations (from surface figure deformations and/or alignment perturbations). While both of these effects could be mitigated to some degree, what would be unavoidable is the mass/cost impact of implementing such a system. While some variations exist that could eliminate some components, this impact was considered to be undesirable, and this option was set aside.

The alternative to the above would be the single-path system (Figure 5.1-6). Acquisition of data over the full waveband would require mechanisms to switch waveband-specific components and repeating observing runs multiple times.

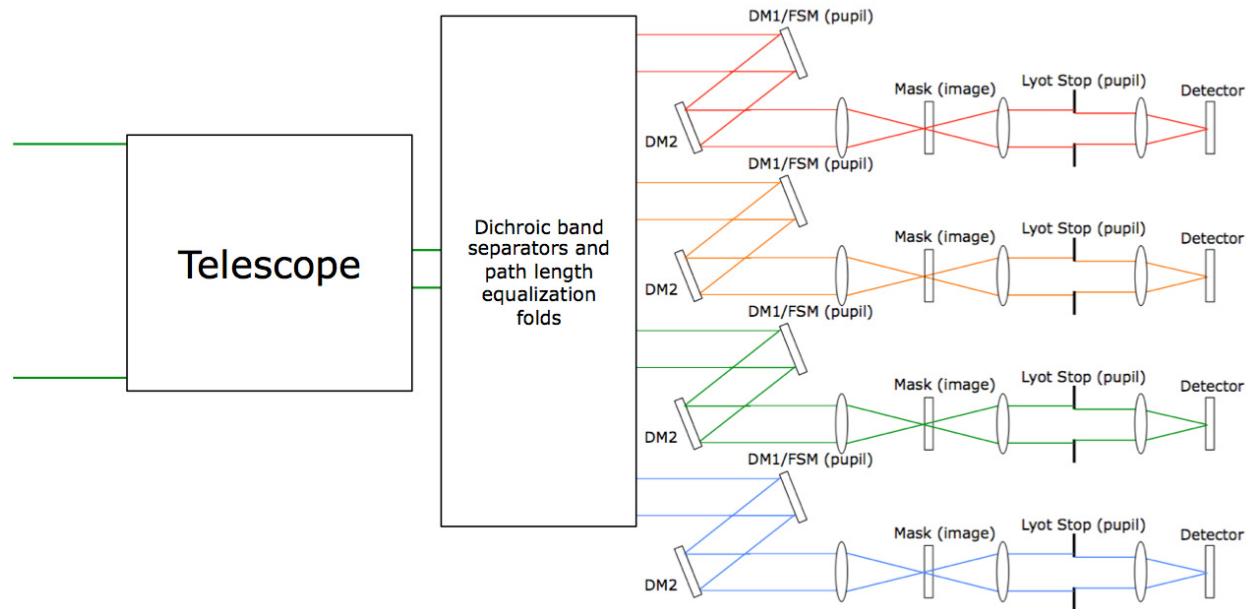


**Figure 5.1-5.** Multiple path option. The dichroic separators and path length equalizers split the collected light into multiple wavebands and channel each band to a dedicated coronagraphic system. This approach would provide efficient use of observing time, but would require significant mass and volume to implement.

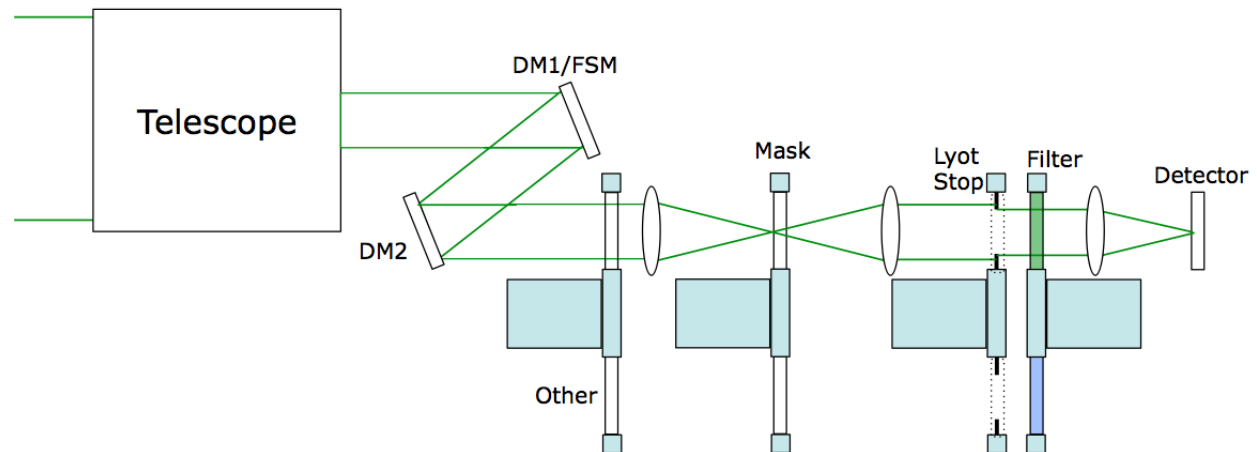


**Figure 5.1-6.** Single path option. In this simplified representation, mechanisms switch-in band-specific elements for sequential observations, with the full waveband covered by multiple narrower wavelength regions. This approach would take longer than the multi-path option to make a full observation, but is considered more practical to implement.

Implementing the single-path option would require several mechanisms; in the ideal case, they would all be copies of a single design to minimize costs. It is expected that packaging, mass, and total costs would be, in aggregate, minimized with this option. So, while the multiple-path option would provide optimum use of observing time, practical considerations (component costs, integration costs, mass)

were weighed in favor of *the single-path option, so it was baselined for the initial STOP analysis at this time.*

#### 5.1.1.4.4 Fine-guidance Path

The desired ideal would be to use the target starlight as the control for the fine-guidance function (control of the fine-steering mirror). Since this starlight would not be accessible past the coronagraphic elements, it must be

acquired ahead of, or within, that zone. Further, since the role of the FGS would be to sense any perturbations of the optical path leading to the key coronagraphic element, acquiring that light as close as possible to the mask would be optimum.

An issue would to be aware of is that of non-common mode influences between the FGS path and the science path. These non-common mode effects will need to be identified and reduced to tolerable levels by choice of configuration, materials, and thermal controls.

The selected option for directing light into the FGS path is a field splitting approach by using the light from the center of the field, i.e., the rejected target star light. This operates with no loss of light in the science path, sending the full amount of available light from the target star to the FGS.

For coronagraphs that function by blocking the light at the mask, the blocking area would be made reflective, and the star light reimaged to the FGS detector (Figure 5.1-7).

In the vector vortex coronagraph the mask would transmit the rejected target star light, but by virtue of the vortex function, its energy

would appear at the edge of the beam. Making the Lyot aperture reflective, the star light would be redirected and focused onto the FGS detector (Figure 5.1-8).

Note that in both of these field-splitting forms starlight would only reach the FGS detector once the system had been reasonably well aligned to the mask. Thus, the initial acquisition function would need to be implemented via other means. A two-step acquisition process is visualized: First, by using spacecraft sensors (star trackers) registered to the instrument line-of-sight, point the spacecraft to get the target star within the field-of-view of the science path. Second, by using the image of the target star on the imaging detector, update the FSM to get the starlight centered on the mask. From that point, the FGS would take command of the FSM to set and hold the desired pointing.

#### 5.1.1.4.5 Spectrometer Path

Once a stabilized high-contrast scene has been established, spectral measurements will be performed for both target identification and target characterization functions. The basic spectral resolution requirement ( $R$ ) to perform these functions was identified to be  $R \sim 70$ .

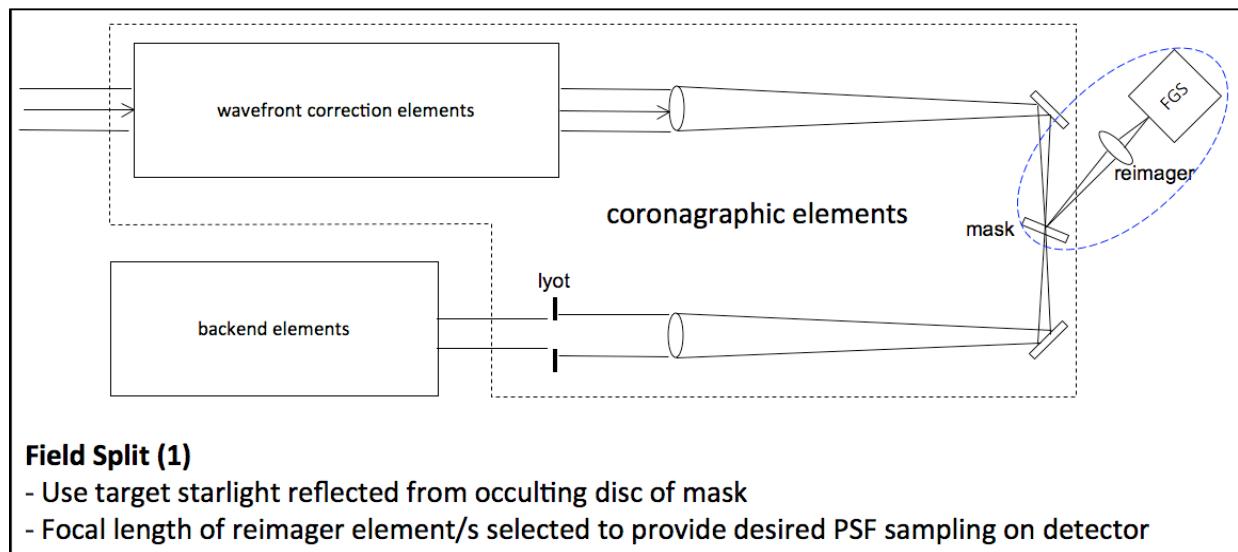


**Figure 5.1-7.** FGS via field splitting at coronagraph mask. Once the system is well-enough aligned using information from the imaging detector, the target starlight is picked up by the FGS for the pointing control function. This option makes use of 100% of the starlight with no throughput loss in the science path.

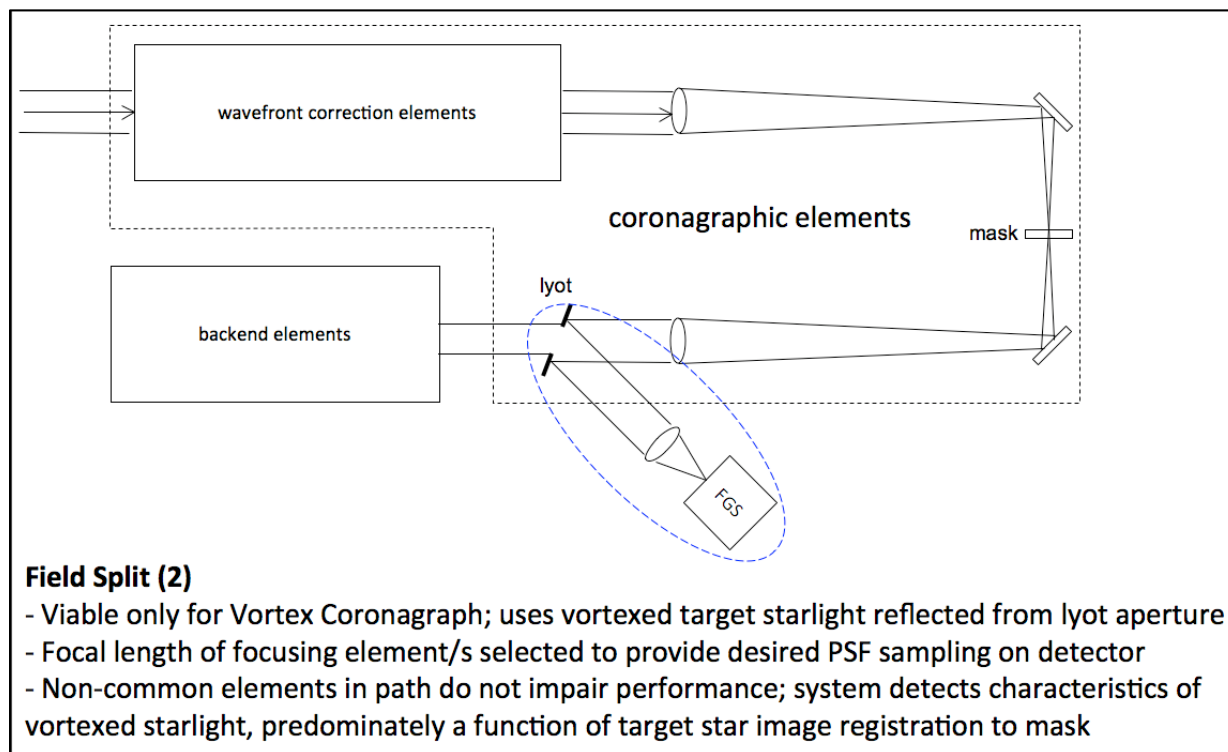


**Figure 5.1-8.** FGS via field splitting at Lyot stop (vector vortex only). Similar in concept and operation to that shown in Figure 5.1-7, except it makes use of the unique property of the vector vortex coronagraph operation that puts the target starlight at the edge of the Lyot stop where it can be redirected with high efficiency to the FGS with no impact to the science path. This option functions without non-common mode effects, making for a simple implementation.

The selected approach to acquiring this measurement is an integral field spectrometer as shown in Figure 5.1-9 that shares the science field-of-view (the annular zone bounded by the inner working angle of the shortest wavelength and the outer working angle of the longest).

Implementation of an IFS would have significant mission benefits. Its detector could perform as a reduced-capacity backup in the event of a failure of the imaging detector. It also provides spectral diversity information within a single observing period, in addition to its primary function of full-field spectrographic measurement.

### 5.1.1.5 Coronagraph

Five coronagraph approaches have been identified for evaluation and comparison in this application. They all have common functional sections: wavefront sensing and control (WFSC), followed by starlight suppression (coronagraph), and finally imaging.

The first and last sections are, to first order, the same for all the approaches. The WFSC section consists of an FSM, DM pair, and simple mirrors as needed to create pupil images on each of these elements of the appropriate size. The imaging section includes filters, lenses, and other elements to fulfill various desired capabilities (waveband limits, calibration functions, imaging functions, etc.).

While there are other minor differences (e.g., how the starlight is sensed for the WFS area), the primary distinctions in the five approaches is in the coronagraph section. A high-level outline of each of the approaches is provided below:

#### 5.1.1.5.1 Lyot/Hybrid-Lyot

This is the classical coronagraph form. After the WFSC section, light from the target star is focused on an occulting disc (mask) that blocks the majority of the starlight while passing virtually all of the light from the

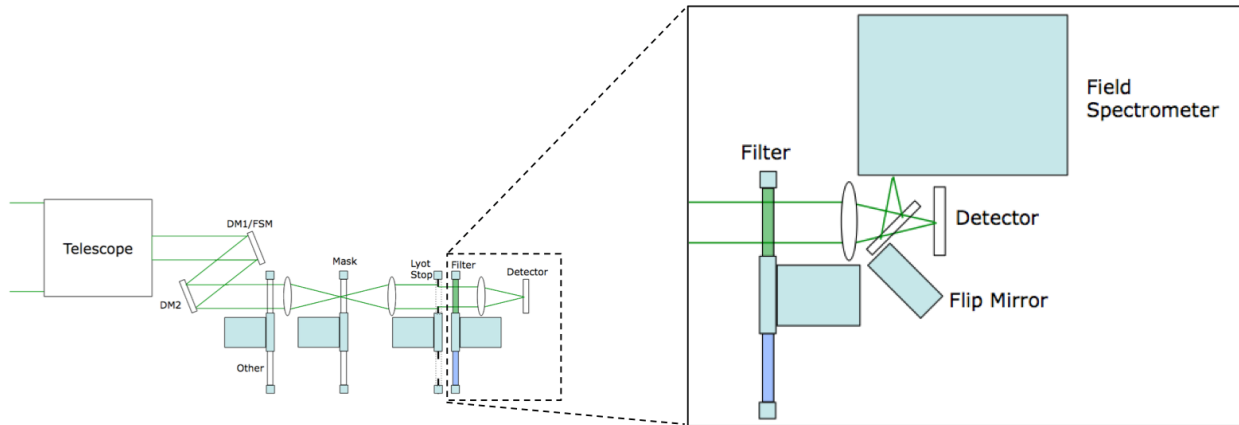


**Figure 5.1-9.** Spectrometer implementation. Once the coronagraph establishes that features of interest exist around a target star, the light is directed into a spectrometer that analyzes the spectral content with a resolution  $R \sim 70$  across the waveband. While a static solution exists (a beamsplitter near the detector), observing efficiency in each mode is maximized by the use of a mechanism that either passes the light to the detector or flips in a mirror to reflect it to the spectrometer.

surrounding region. In the hybrid variation, a metal and dielectric coating is applied to the mask to provide improved suppression of the starlight at the focal plane. A Lyot mask placed at a downstream pupil image blocks the bulk of the diffracted starlight from the edge of the pupil, and the beam, now with the starlight effectively removed, passes on to the imaging section (Trauger 2012).

#### 5.1.1.5.2 Vector Vortex

This approach is structurally identical to the Lyot approach, except the occulting mask is replaced by a structured phase plate that induces a complex phase pattern onto the wavefront. The effect of that pattern is to diffract the starlight to the periphery of the wavefront at a downstream pupil image where it is blocked by the Lyot stop. The nature of the phase plate is such that only light centered on the plate experiences this effect; light from the surrounding region propagates through and is passed by the Lyot stop to be imaged at the focal plane (Serabyn 2013).

#### 5.1.1.5.3 Shaped Pupil

This approach is essentially identical to the Lyot, except an amplitude mask is located in a pupil plane before the light reaches the occulting mask. The amplitude mask shapes the energy distribution in the focal plane to suppress diffracted light effects.

Implementation comes at a throughput cost as effective masks typically have transmission efficiencies around 25–50% (Kasden 2012).

#### 5.1.1.5.4 Phase-induced Amplitude Apodization

This is another technique for reshaping the energy distribution in the beam to suppress diffraction effects. It uses additional elements in the optical train to induce beam apodization ahead of the occulting mask, and a second set of additional elements following the Lyot stop to unwrap the apodization in order to provide good imaging across the outer working angle (OWA) (Kern 2013).

#### 5.1.1.5.5 Visible Nuller

This approach is structurally different from the four others. Rather than focusing the light to a coronagraph mask, the wavefront is split, phase shifted, and interferometrically recombined to create a regular pattern of destructive interference across the field of view. The system is aligned to place the target star in one of these zones to null its light; multiple observations made with rotations of the null pattern around this point reveal any objects of interest at the target star (Lyon 2012).

#### 5.1.1.5.6 Coronagraph PROPER Modeling

The predicted science return of each coronagraph (e.g., the number of planets potentially characterized within a given amount of time) is dependent on the contrast that can be achieved.

Because of the effects of optical aberrations and wavefront control, the contrast could not be reliably determined via analytical methods. It required end-to-end numerical modeling of the optical system including realistic errors on each surface and wavefront control with DMs.

In this study, a realistic numerical model of the optical system for each approach was constructed using the PROPER library for IDL (Krist 2007). The resulting performance predictions were incorporated into the downselect process.

#### 5.1.1.5.7 Coronagraph Architecture Downselect

Each of the approaches outlined provides different performances such as IWA, OWA, throughput, bandwidth, contrast, as well as varying levels of complexity, and technology readiness level (TRL). Carrying a design and performing analyses for all five approaches would exceed the resources available to this task; in order to narrow the field for the work going forward, the capabilities of each of the approaches (both as demonstrated to date in laboratory testing and as projected for flight implementation) was collected as shown in Table 5.1-4.

A weighted trade of these capabilities and other factors was performed, and relative scores assigned to each approach. After all considerations were taken into account, the hybrid Lyot approach was ranked as first choice and hence baseline for this mission, while the vector vortex and PIAA approaches scored a very close second and third

respectively. The vector vortex approach has an architecture that is highly compatible with the hybrid Lyot, and will be carried as the prime alternate in case the hybrid Lyot does not achieve its projected flight levels of performance in future testing. In the meantime, progress made on the PIAA by other studies will be monitored and compared against developments for the vector vortex. Should it become necessary to pursue one of these alternate approaches, the trade for these two will be reevaluated at that time and a final selection made.

#### 5.1.1.6 Low-order Wavefront Sensor

##### 5.1.1.6.1 Summary

Although each coronagraph design has different sensitivities to wavefront drift, all coronagraph designs will require a LOWFS in a closed loop with DMs to maintain contrast levels of  $10^{-9}$  for the duration of the typical exposure. Three LOWFS architectures were examined in detail and the Zernike Wavefront Sensor (ZWFS) was chosen as the baseline method for the Exo-C probe mission.

##### 5.1.1.6.2 Introduction

It has been shown by Green and Shaklan (2003) that coronagraphs designed for  $10^{-9}$  contrast and small inner working angles are sensitive to low-order wavefront drift as small as a few 10s of picometers. Maintaining this level of stability during the exposure requires a dedicated sensor that feeds the wavefront error signal back to a DM, which is actuated to correct the drift. The dominant contributors to

**Table 5.1-4.** Performance summary of the coronagraph architecture options. The columns “Flight” are the projected capabilities of the architectures, while “Lab” columns contain performance numbers that have been shown to date in laboratory testing. The difference between the two columns provides an indication of the relative maturity of the technology, and the relative amount of development work remaining for each.

Coronagraph Architecture		Option 1		Option 2		Option 3		Option 4		Option 5	
		Hybrid Lyot		Vector Vortex		Shaped Pupil		PIAA		Visible Nuller (Davinci)	
		Flight	Lab	Flight	Lab	Flight	Lab	Flight	Lab	Flight	Lab
IWA	λ/D	2.2	3	2.2	2	3	4	2.1	2	1	3
OWA	λ/D	16	15	20	7	21	~20	18	4	24	N/A
Bandpass	%	20	20	20	10	20	10	20	10	20	10
Contrast (floor)		1.E-10	1.E-09	5.E-12	9.E-09	8.E-10	2.E-09	3.E-11	1.E-08	2.E-09	2.0E-06
AZ Coverage	degrees	360	180	360	180	360	~90	360	180	90	N/A
Throughput: Pupil x Reflectivity	%	37	-	33	-	17	-	49	-	18	-

loss of contrast are focus, astigmatism, coma, trefoil, and spherical aberrations. These are also the dominant terms arising from figure and rigid body drift of individual optical elements due to thermal settling.

#### 5.1.1.6.3 LOWFS Trade

Many wavefront sensors have been developed over the years, but most are not suited for the photon-limited regime of a probe-class coronagraph (Guyon 2005). While no LOWFS has been demonstrated at the level of performance needed for Exo-C, the trade selected the ZWFS (N'Diaye 2013) for further study due to its simplicity, performance, and compatibility with the selected coronagraphs. A detailed description of the proposed ZWFS implementation is presented in §6.5.5.

#### 5.1.1.7 Primary Mirror Material Options

We performed a trade study to determine the primary mirror material for the Exo-C mission study. The design team favors a glass primary mirror design given the constraints and assumptions of this mission study. The flight heritage and low thermal expansivity of a glass primary mirror are deemed important design factors. Among the glass options, the design team favors ULE due to its slightly favorable mass in designs with flight heritage, see Figure 5.1-10.

#### 5.1.1.7.1 Assessment of Factors

The first four factors (WFE, wavefront drift, thermal settling time, and mass) were evaluated based on engineering handbook data, prior mission studies, and prior technology demonstrations. The last two factors (maturity/risk and cost) were examined based on engineering experience.

#### Wavefront Error

The science requirements for this mission study specify an overall system WFE of  $< 1$  nm root mean square (RMS) including two DMs and a LOWFS. In addition, the overall system wavefront stability must be  $< 0.1$  nm RMS over the duration of each science observation. (To characterize Earth-like planets would require wavefront stability  $< 0.01$  nm RMS) Spectroscopy observations can have durations  $\geq 48$  hrs. A comparison of candidate materials showed that glass provides the best WFE performance in this application.

#### Wavefront Drift

The dynamic wavefront stability of each trade space option was taken into consideration.

#### Thermal Settling Time

Approximate values for the thermal settling time of each trade space option were

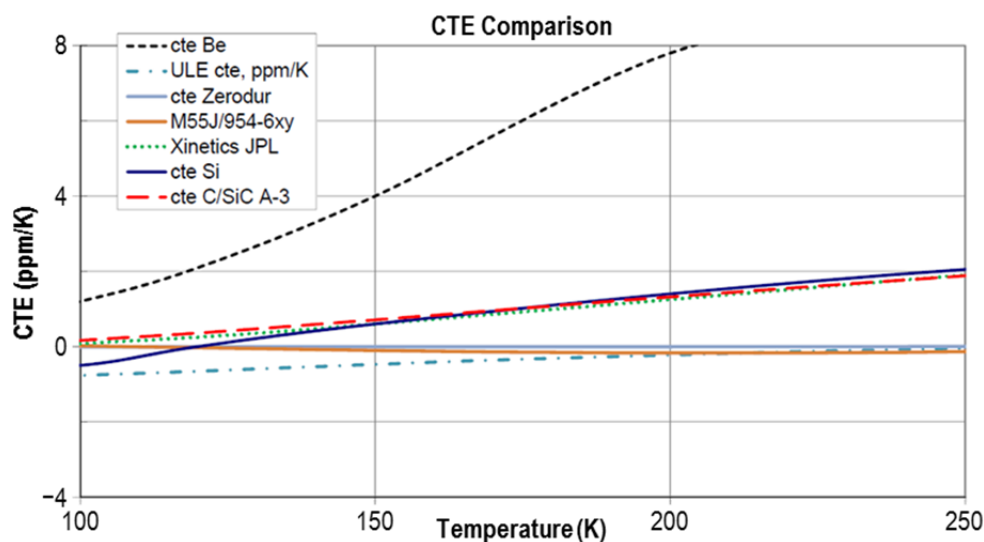


**Figure 5.1-10.** Thermal expansivity of various optical and structural materials (Green et al. 2012). The modest power requirements to maintain the primary mirror at 290 K are more than compensated by the low thermal expansion capability of ULE and Zerodur.

evaluated. While glass was not the best performer in this area, the difference between it and the better-performing materials was not significant enough to affect the trade outcome.

### **Mass**

The mass of each trade space option was assessed. While glass compared relatively unfavorably in this area, like above the difference was not significant enough to dominate the trade process.

### **Maturity/Risk**

The TRL of each trade space option was considered in this trade, with the TRLs being best estimates based on the collective experience and engineering judgment of the team. This factor was critical as the cost to mature technology to flight readiness levels must be included in the overall mission cost of \$1B.

Although other materials options have been flown on several missions, they have been either substantially smaller than 1.5 m in diameter or the surface finish has not been adequate for coronagraph missions. In this area, the glass option was found to be significantly superior.

### **Cost**

Requests for information have not been sent out; however, recent surveys suggest that, of the material options, glass would enjoy a notably lower cost.

#### **5.1.1.7.2 Conclusion**

Although other materials have an attractive technology for the benign thermal environment of either Earth-trailing or L2 orbits, overall, glass is favored due to the cost and schedule risk required to mature other material mirror technology to flight readiness levels. The lower mass and faster settling time of the alternatives are deemed less important design factors than cost and maturity. Among the glass options, ULE is favored due to its slightly lower mass in designs with flight heritage.

## **5.1.2 Mechanical**

The design of the telescope is a result of the standard mechanical configuration design and analysis process. No mechanical trades have been conducted. The mechanical design, up to this point, has been largely driven by optical design decisions and considerations. For example, the decision to move the instrument bench to the side of the inner barrel led to the elimination of the Aft Metering Structure and the Secondary Support Tower. Additionally, the decision was made to have an articulated secondary mirror, instead of a stationary mirror, due to alignment and ground-to-orbit structural effects.

## **5.1.3 Thermal**

### **5.1.3.3 Introduction**

To date, the thermal/mechanical design team has performed two trade studies, both aimed at characterizing the thermal settling time and wavefront (WFE) stability of the primary mirror (PM). The first trade studied the effect of four different heater controller configurations on the thermal settling time and WFE stability of the PM, while the second trade studied the effects of varying the amount of solar shielding. Two spacecraft maneuvers were used as representative input disturbances to the thermal control system. These maneuvers were a 45° pitch (maximum slew to the next star) and a 30° roll (needed to distinguish speckles from planets during discovery observations). A visual depiction of each maneuver is presented in §6.10, Figures 6.10-1 and 6.10-2, respectively.

### **5.1.3.4 Trade #1: Heater Controller Design**

In order to characterize the relationship between heater controller design complexity and optical performance (measured as PM settling time and PM WFE stability), four different heater controller designs were implemented—two active techniques, and two constant. The location of heater zones and temperature sensors was the same across all configurations. The PM surface figure error (SFE) in response

to a representative  $45^\circ$  pitch maneuver was analyzed for each design configuration. The two active control approaches met the current thermal settling time requirement of less than 4 hours. In addition, the SFE stability is much better with active control. It is important to note that SFE drifts over time and must be kept small during each science observation in order to maintain a high-contrast ratio in the coronagraph instrument. Alternatively, the magnitude of SFE present when the PM reaches steady state is not important for errors on these scales since the DMs can correct for the static offset. The amount of acceptable PM SFE drift during a science observation has yet to be determined since the design team is still working to develop a detailed error budget.

#### 5.1.3.5 Trade #2: Solar Shielding Design

To characterize the relationship between solar shielding and optical performance (measured as PM settling time and PM WFE stability), four solar shielding concepts were studied. The four designs are shown in Figure 5.1-11.

Each solar shielding design was subjected to a representative  $45^\circ$  pitch, and  $30^\circ$  roll maneuver with active heater control on the inner barrel and PM (cases 1 through 4). In addition, for comparison, the fourth solar shielding design (Figure 5.1-11d) was also subjected to a  $45^\circ$  pitch, and  $30^\circ$  roll maneuver with no active heater control (case 5).

The results show marginal improvements provided by additional shielding. These must be weighed against the cost of manufacture and testing of the additional shields. The results of this trade lead us to choose a baseline design with no sunshields (aside from the outer barrel) and a single fixed solar array that partially covers the outer barrel (Figure 5.1-11d).

It is important to note that the two thermal trade studies presented in this section focus on characterizing the thermal settling time and wavefront (WFE) stability of the primary mirror. Another important metric for telescope performance is the spacing between the PM and secondary mirror (SM). A detailed analysis is presented in §6.10 that includes PM to SM spacing.

## 5.2 Mission and S/C Trades

### 5.2.1 Earth-trailing vs. L2 Orbit Trade

This section lays out considerations for comparing science capability and cost associated with an observatory located in an Earth-trailing orbit versus a halo orbit at about the Earth-Sun L2 Lagrange point. For this study, the mission's science capability was assessed as a function of sky accessibility and target availability. In addition, model-based cost estimation was used to determine engineering and operation cost differences to access and maintain the two orbits.

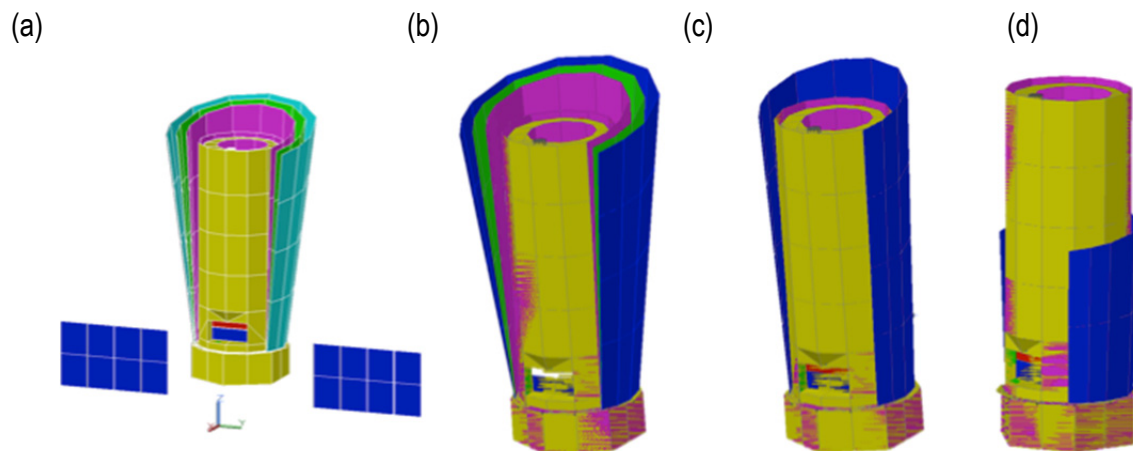


**Figure 5.1-11.** Four different sunshield configurations: (a) three sunshields, articulated solar arrays, (b) two sunshields, one fixed solar array, (c) one fixed solar array—full cover, and (d) one fixed solar array—partial cover.

The initial examination of this trade suggests that there is no significant increase in target availability or data return capability for a L2-orbiting spacecraft over an Earth-trailing spacecraft. As a result, the major driver for orbit selection will be determined by the overall mission cost. Due to increased operations for orbital maintenance, L2 orbit requires additional navigation costs that the Earth-trailing orbit does not. Therefore, the Earth-trailing orbit is recommended as the baseline orbit for the Exo-C Probe study.

### 5.2.1.3 Approach to Study the Trade

The orbital trade study was broken up into two parts to better understand the effects of choosing an L2 halo versus an Earth-trailing orbit. To assess the science drivers for the various orbits, visibility, and target scheduling for Spitzer (Earth-trailing) and the James Webb Space Telescope (JWST) (L2 halo) were compared based on their viewing constraints. This provided a better understanding of the portions of the sky that will be visible throughout the mission either from the L2 halo orbit or from the Earth-trailing orbit.

To better understand the engineering and cost ramifications of choosing one orbit over the other, a sample spacecraft architecture was selected and examined using JPL's institutional cost models. Small variations to the telecom and propulsion subsystems were changed based on requirements levied by the orbit selected. From there, an overall mission cost was produced for each orbit and compared.

### 5.2.1.4 Earth-trailing and L2 Halo Orbits Characteristics

#### Earth-trailing Orbit

Earth-trailing orbit is a heliocentric orbit where a spacecraft is provided a very low positive characteristic energy, allowing the spacecraft to barely escape the Earth's sphere of influence. Once in heliocentric space, the spacecraft will continue to drift away from the Earth at a rate of roughly 0.11 AU per year. Table 5.2-1 describes various characteristics for an Earth-

trailing orbit that drive the spacecraft design, while Figure 5.2-1 provides a visual depiction of the orbit. Figure 5.2-2 depicts the Earth's location within the Exo-C viewing zone.

**Table 5.2-1.** Earth-trailing orbit characteristics.

Parameter	Value
Launch Characteristic Energy	0.4 km <sup>2</sup> /s <sup>2</sup>
Max Distance from Earth	0.33 AU (after 3 years)
Orbital Maintenance Delta V	0 m/s

#### L2 Halo Orbit

The L2 halo orbit is an actively controlled orbit in which the spacecraft maintains a stable orbit at about the L2 Lagrange point. This particular orbit provides an ideal viewing platform, allowing an observatory to access the entire sky as it rotates around the Sun. Though the orbit maintains a constant distance from the Earth for communication, it also requires constant orbit maintenance, including frequent maneuvers for stability. Table 5.2-2 and Figure 5.2-3 provide orbit characteristics and a visual

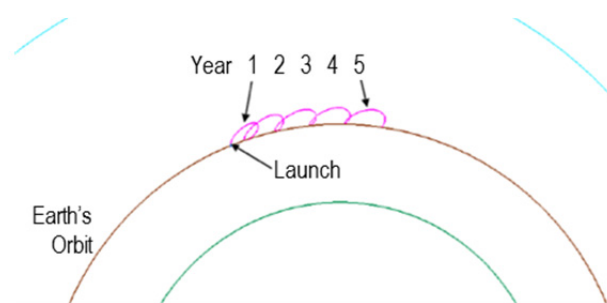


**Figure 5.2-1.** Depiction of an Earth-trailing orbit.

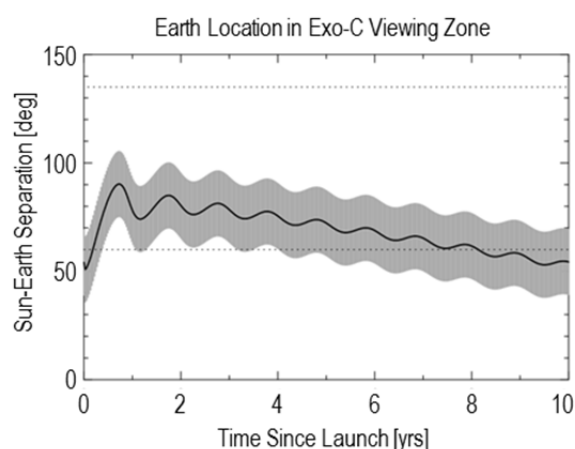


**Figure 5.2-2.** Earth location in Exo-C viewing zone for Earth-trailing orbit.

depiction of the L2 halo orbit.

**Table 5.2-2.** L2 halo orbit characteristics.

Parameter	Value
Launch Characteristic Energy	0.5 km <sup>2</sup> /s <sup>2</sup>
Max Distance from Earth	1500000 km
Orbital Maintenance Delta V	150 m/s

### 5.2.1.5 Science Target Selection and Visibility

With regard to sky accessibility and periods of target availability, an Earth-trailing orbit has comparable advantages to an L2 orbit. Models for comparison of visibility and target scheduling for these two orbits include Spitzer, which has an Earth-trailing orbit, and JWST, which will have an L2 halo orbit. The two telescopes have comparable target viewing windows and sky availability.

In Earth-trailing orbit, the operational pointing zone (OPZ) of an astronomical telescope migrates at a rate of  $\sim 1^\circ$  per day such that the entire sky is visible during the year. However, the number of days in which a target will be visible is a strong function of that target's ecliptic latitude. Within  $10^\circ$  of the ecliptic poles, targets are visible year round in the continuous viewing zone (CVZ). From  $\pm 80^\circ$  ecliptic latitude, targets are visible for a single extended period of time, which decreases with decreasing absolute latitude. At ecliptic latitudes below  $60^\circ$ , the viewing zones break into two shorter periods per year, down to a target on the ecliptic plane, which will be visible for approximately 75 days, twice a year. For our exoplanet targets, we would

therefore be able to schedule observations at least 6 months apart, which would be important for phase-dependent measurements. For targets near the poles, there would be a lot more flexibility in scheduling revisits and orbital phase sampling.

For comparison, JWST can observe targets in the ecliptic plane for approximately 53 continuous days, twice a year. Targets within  $45^\circ$  of the ecliptic have two visibility windows per year. There are larger continuous visibility periods above  $45^\circ$ , and these periods culminate in continuous accessibility within  $5^\circ$  of the ecliptic poles.

Targets on the ecliptic are susceptible to zodiacal light, and they have their viewing windows truncated by the presence of the Solar System's planet (including the Earth), which can drift into the OPZ from the sunward direction for an Earth-trailing spacecraft in the first few years of the mission. This problem will not affect a telescope at L2, which is shielded against the Sun, Moon, and Earth, and which will only have to avoid planets at larger distances from the Sun than the Earth. Spitzer's policy was to avoid the Earth by at least  $7^\circ$  when it was in the OPZ, which can heavily truncate available observing periods for targets on or near the ecliptic plane. All other Solar System planets had a  $0.5^\circ$  zone of avoidance. For the Exo-C design, we may need an even tighter avoidance constraint. For Spitzer, the Earth was in the OPZ in the first two years of the mission, dwelling near the inner edge of the OPZ for 160 days in year one and for 132 days in year two. Its largest excursion into the OPZ was a few degrees. However, even at these times, targets beyond the  $7^\circ$  Earth avoidance zone were visible and operations continued. Having the Earth enter the OPZ will only affect targets near the ecliptic, which is already an undesirable region due to zodiacal light, and should not affect overall observing strategies for extrasolar planet observations, since the target stars will be widely distributed across the sky.

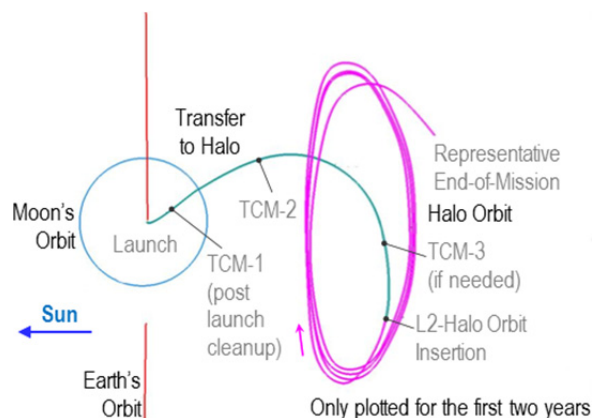


**Figure 5.2-3.** Depiction of sample L2 halo orbit.

### 5.2.1.6 *Spacecraft Considerations for the Orbits*

Both the Earth-trailing and L2 halo orbits have unique considerations required when designing spacecraft. For the Earth-trailing case, communication is the driving engineering hurdle, while the L2 halo case requires a more capable propulsion system. For both orbits, subsystems-specific upgrades are required to a “standard” spacecraft bus designed for Earth orbit in order to meet mission requirements. For comparison purposes, we assumed a standard spacecraft bus consists of deep space capable avionics, attitude determination and control, power, structure and thermal that would be used independent of the orbit selected. From there, communication and propulsion capabilities are added to the bus, depending on mission requirements for the selected orbit. Model-based costs were developed using cost models to differentiate the overall bus costs associated with each orbit.

#### *Communication Variations*

Due to the drift rate of the Earth-trailing orbit, communication is a major consideration to meet the science needs of the mission. As the observatory drifts farther from Earth, the data rate capability of the system decreases at a rate proportional to the distance squared. To meet the new distances and provide the data rates necessary for the science mission, the frequency used and radio frequency power output must be designed to meet the data rate requirements at the maximum distance from the Earth. A communication system based on that used by Kepler was examined and was determined to provide sufficient data rates for the Exo-C mission at maximum expected distances in an Earth-trailing orbit.

In comparison, the L2 halo orbit always remains fixed, and relatively close to Earth (1,500,000 km). This allows the spacecraft to employ a much simpler system to meet the communication needs of the mission.

### *Propulsion Variations*

Propulsion systems are used in space missions for a number of reasons, including trajectory corrections, maintaining a steady orbit, or for desaturating the reaction wheels due to rotational rate build-up from reorientation of the spacecraft. As a result, observatories in both the L2 halo and Earth trailing orbits require a propulsion system for one or more of these reasons.

For the L2 halo orbit, the propulsion system is required to perform all three of the above operations, including, “clean-up” discrepancies in the launch vehicle’s original trajectory, injection maneuvers, and minor but consistent halo orbit maintenance. These maneuvers are substantial, requiring a fairly capable propulsion system to move the observatory around.

The Earth-trailing orbit is substantially easier to access and maintain. Since the orbit is effectively a heliocentric, uncontrolled orbit, there are no additional maneuvers required outside the initial launch vehicle injection burn. As a result, the only propulsion system required by the mission is for spacecraft orientation, including reaction wheel desaturations. These maneuvers are quite small, requiring a very small propulsion system.

#### *5.2.1.7 Cost Trades Discussion*

To assess the cost impacts of the two orbits, sample missions were examined using the JPL Institutional Cost Models. A baseline mission concept was developed and used for both the L2 halo and Earth-trailing orbit to ensure that only changes due to the orbit selection affected the cost. From there, orbit-specific spacecraft and operations variations were applied to compare the cost differences.

The Earth-trailing option was estimated to be between \$10M and \$20M cheaper than the L2 halo option. The major savings for this option is due to the navigation support associated with maintaining the Halo orbit. This requires a fully staffed navigation team throughout the life of the mission to analyze

the current orbit of the spacecraft, plan, and perform correction maneuvers when appropriate. Since the Earth-trailing orbit requires no additional maintenance maneuvers, this team can be substantially reduced to almost nothing. All other variations, including the propulsion and communication trades, effectively cancel each other out.

### 5.2.1.8 Summary and Conclusion

The initial examination of Earth-trailing versus L2 halo orbit trade suggests that the Earth-trailing orbit is the low-cost option with minimal impact to target visibility and selection for the Exo-C probe study. As a result, it is recommended that the baseline option moving forward should be an Earth-trailing orbit.

## 5.2.2 S/C Architecture

This section lays out considerations for the comparison of contractor-built “off-the-shelf” spacecraft buses versus a custom designed bus.

The initial examination of this trade space suggests that a mission based around a contractor-built spacecraft bus is likely the lowest-cost mission. Of the missions examined, Kepler and Spitzer seem to draw the most similarities to the Exo-C mission, including payload size, power generation, communication and propulsive capability. An architecture utilizing one of these types of buses will likely provide the lowest cost and least risk option for the Exo-C mission.

### 5.2.2.3 Potential Vendor Buses

NASA has recently conducted a range of observatory missions that used commercially built buses. Of these missions the Kepler and Spitzer space telescopes share the most similarities to the Exo-C mission. Both of these spacecraft are good analogies due to their mission class, payload size, and observatory orbit.

To assess the capability of meeting the Exo-C mission requirements, a set of guidelines was developed using mission and instrument requirements defined for the study. These guidelines allowed for the comparison of a variety of potential observatory buses, including the Kepler and Spitzer buses to determine the required modifications needed to meet the mission objectives.

#### 5.2.2.3.1 Potential Bus Product Lines

Table 5.2-3 provides a summary of the Kepler and Spitzer bus capabilities. Both buses require minor modifications to increase payload and power capabilities to accommodate the Exo-C payload. Both missions employed a similar overall mission architecture to that being proposed for the Exo-C mission, including overall mission life, observing scheme, and target orbit. As a result, either bus would be favored moving forward toward the development of the Exo-C mission.

#### 5.2.2.4 Conclusion

Due to the existence of “product lines,” commercial buses are likely to be the lowest cost option for developing the Exo-C spacecraft bus. Of the many observatory missions examined during this trade study, the Kepler and Spitzer missions carry the highest amount of heritage for the overall mission architecture. As a result, buses developed based on these missions will likely be the lowest cost and least risky options moving forward for Exo-C.

## 5.2.3 Mission Lifetime and Operations

### 5.2.3.3 Summary

An initial examination of the trade relating the increase in mission cost due to mission life vs. additional science acquired suggests that there is potentially a significant increase in overall mission cost for an incremental increase in

**Table 5.2-3.** Summary of key parameters for commercial buses that could meet the science objectives of Exo-C.

Bus	Target Orbit	Payload Mass	Available Power	Propulsive Capability	Downlink Capability	Pointing Capability
Kepler	Earth Trailing	478 kg	807 W	~50 m/s	4.3 Mbps	0.75 arcsec
Spitzer	Earth Trailing	403 kg	413 W	~150 m/s	2.2 Mbps	5 arcsec

overall science. Though increased mission life will provide for additional observations and an increased cadence, baselining the longer mission will result in additional technical requirements as well as an increase in operations cost. As a result, it has been determined that the mission will baseline an overall mission life of 3 years, but will carry consumables for 5 years to allow for a potential extended mission.

#### **5.2.3.4 Introduction**

To first order, the mission lifetime trade exchanges cost for additional observations. Additional observations serve to increase the size of the surveys and can improve the quality of measured parameters. For example, better orbital parameters may be obtained by measuring a longer portion of an orbit. If a planet has a 12-year orbit, then the fit of that orbit will have significant improvements as the length of the mission increases to a larger fraction of that orbit.

The drivers for increasing lifetime are consumables, tougher end-of-life (EOL) requirements, and operations cost. We will assume that all the parts and reliability will stay the same, since Exo-C is a Class-B mission, regardless of the lifetime. Of these, the operations cost is the dominant factor, since we plan to have consumables for 5 years, regardless of the planned lifetime. This ensures that we have the capability to extend the mission later on, and adds margin to the consumables.

The lifetime trade space is between 3 and 5 years. The 3-year minimum is set by the minimum science observations levied on the mission. The 5-year maximum is set by the program office's requirement that Exo-C be a Class-B mission. Although there are exceptions, missions longer than 5 years will tend toward the higher reliability Class-A requirements. Since these are the two extremes, we have selected these two as the only possible options for the trade space.

#### **5.2.3.5 Increase in Science**

There are two scientific benefits to increasing the lifetime of the coronagraph mission. First, lifetime increases the number of observations, and second, it improves the timing or cadence at which measurements can be made. We will address each separately in the following subsections.

##### **5.2.3.5.1 Additional Observations**

We will assume that by the Exo-C mission launch, enough known RV planets will be available that we can linearly scale up the number of targets, such that we are not imaging dimmer and dimmer planets. Although this is a simplification, it is a reasonable assumption since RV measurements are still ongoing and improving. Other science branches, such as planetary searches and dusk disks characterizations, already have plenty of targets. Hence, for this trade we will linearly scale all science by the number of years observing. Table 5.2-4 shows the number of science targets for each of the two lifetime options.

##### **5.2.3.5.2 Improved Science Cadence**

The improvement in the cadence is much harder to assess and would have to be modeled properly in order to determine the benefits to measuring long orbital periods over 5 years, compared to the 3-year baseline mission lifetime. In addition, a statistical model would have to be used with typical orbital periods that we are going to observe. If the typical orbital periods are short compared to the lifetime, then increased lifetime will be less beneficial.

#### **5.2.3.6 Resources Needed**

The affected resources needed to change the lifetime from 3 to 5 years are cost and consumables. In addition, the requirements specified at EOL become more stringent. We address each of these in the next subsections.

##### **5.2.3.6.1 Consumables**

The current baseline is to carry 5 years of consumables, regardless of mission lifetime. Given the \$1B cost of these concepts, any

Science Type	Visits		Science Observation		Total Mission Time	Visits		Total Mission Time	Delta
	No. of targets	Ave No. of visits	Ave. Integration time/visit	Total Observe time per Science Type		No. of targets	Total Observe time per Science Type		
	N_target	N_visit	t_I (hrs)	T_Obs (days)	T_M (days)	N_target	T_Obs (days)	T_M (days)	N_target
<b>Planet characterizations</b>									
Spectroscopy of Known Exoplanets (known from RV and exo-C survey)	20	1	200	167	193	25	104	136	5
Multi color photometry of Known Exoplanets (known from RV and exo-C survey)	20	1	20	17	43	30	25	64	10
<b>Planet discovery surveys</b>									
Survey nearby stars for super-Earths within the habitable zone	20	6	20	100	150	40	200	300	20
Search for giant planets around nearby stars	140	3	20	350	525	200	500	750	60
<b>Disk Imaging Surveys</b>									
Detection survey in RV planet systems	60	1	12	30	40	120	60	80	60
Known debris disks within 40 pc	60	1	6	15	24	100	25	40	40
Young debris disks from WISE	100	1	6	25	40	300	75	119	200
Nearby protoplanetary disks	80	1	6	20	32	200	50	79	120
<b>Total on-orbit ops time</b>				<b>723</b>	<b>1045</b>		<b>1039</b>	<b>1568</b>	
Initial On-Orbit Checkout (days)					60			60	
Total (days)					<b>1105</b>			<b>1628</b>	
<b>Total (years)</b>					<b>3.0</b>			<b>4.5</b>	

**Table 5.2-4.** This table shows the number of science targets for the 3- and 5-year options (center and right columns, respectively). The last column shows the difference between the two cases.

future mission would represent a significant asset to NASA so carrying enough propellant to support operations through the typical expected life of the commercial bus, regardless of the time required to meet the mission's primary science goals, would be sensible. As often happens, the spacecraft could be repurposed to a different mission once the science goals of its original mission are reached. Hence, there is no change in the consumables that Exo-C would carry.

#### 5.2.3.6.2 Operating Costs

Based on Kepler actual operations costs, Exo-C is budgeting just under \$20M FY15 per year plus 30% cost reserves. This means that adding 2 years to the current 3-year baseline mission, would increase operations costs by about \$50M.

#### 5.2.3.6.3 End-of-Life Requirements

Several other requirements, such as the solar panel output, are set at mission EOL. For this concept, EOL is defined as the end of the primary science mission—3 years. Any subsequent missions will make the best use of the spacecraft's resources available at that time, and most can compensate operationally

for degradations below performance levels required for the primary mission.

#### 5.2.3.7 Conclusion

The lifetime trade is fundamentally a trade between additional costs and additional observations. The additional \$50M in cost for a 5-year mission represents a significant increase and would impact other elements of the mission concept in order to meet the \$1B total mission cost cap. This impact to the baseline design is not seen as a worthwhile tradeoff against the improvement in science created by an additional 2 years of observations. Accordingly, the recommended baseline design life is 3 years, with consumables sized for 5 years.

#### 5.2.4 Solar Array and High Gain

We evaluated articulated vs. body-fixed versions of both the Solar Array and the High Gain antenna. In both cases, the body-fixed version saves mass and cost, while still being able to meet the science requirements. We have therefor baselined body-fixed versions of both.

## 6 Baseline Configuration and Implementation for Detailed Study

### 6.1 Baseline Configuration Overview

Following the architecture trades described in §5, a baseline configuration for Exo-C has been chosen. With many of the trades breaking in favor of an architecture similar to Kepler, Exo-C has gravitated toward a Kepler-like design as a proof-of-existence model for this Interim Report. With a total mission cost around \$750M FY15—well below the Probe study \$1B requirement—Kepler makes an excellent starting point for the Exo-C design. Aside from the payload, Exo-C is very similar to Kepler in design, only needing to add a two-stage passive vibration isolation system to the original Kepler architecture. These passive isolators are flight proven technology. The only other planned changes to the bus are more reliable reaction wheels and some structural panel resizing.

The ground system too is based on Kepler. For this existence-proof baseline, there were no significant departures from the original Kepler ground architecture. Only the payload is significantly different, and even then, the telescope is of comparable size and complexity to Kepler.

This section describes the baseline configuration of the payload, spacecraft, and ground system.

### 6.2 Mechanical Configuration

Exo-C consists of the instrument payload attached to the spacecraft bus, as seen in Figure 6.2-1. Mounted directly to the top surface of the bus is the outer barrel assembly, which is comprised of the outer barrel structure and the outer lid. The outer barrel assembly encloses the payload, which includes the inner barrel assembly, the primary and secondary

mirror assemblies, the primary support structure (PSS), the instrument bench with instruments and optics, the payload avionics, and the star trackers (see Figure 6.2-2). Two openings in the outer barrel give the payload radiators a view to cold space. Both the inner and outer barrels have a scarfed baffle structure at the top. Along the height of the inner barrel are thin cylindrical ribs to suppress stray light.

Mounted atop the PSS is the primary mirror assembly (Figure 6.2-2). The payload avionics are mounted to the underside of the PSS.

The secondary mirror assembly is attached to the top of the inner barrel (see Figure 6.2-4). The assembly is comprised of the secondary mirror, and the secondary support structure.

The instrument bench is designed such that the optics and instruments are enclosed within the bench. Access holes have been designed into the top panel to enable installation and adjustment of the bench components. A computer-aided design (CAD) model of the bench and the optics layout are shown in Figure 6.2-5. The optics layout will be discussed in more detail in §6.5.

The payload is attached to the spacecraft bus at the PSS via a vibration isolation system (see Figure 6.2-1) to isolate the payload from bus disturbances.

The payload contains two separate radiator panels (see Figure 6.2-2). The instrument radiator panel attaches directly to the top instrument bench panel, while the payload avionics radiator mounts to the side of the PSS. Two star trackers, along with the star tracker electronics, attach to the inner barrel in between the instrument bench and the PSS. The star tracker electronics share a radiator with the payload electronics.

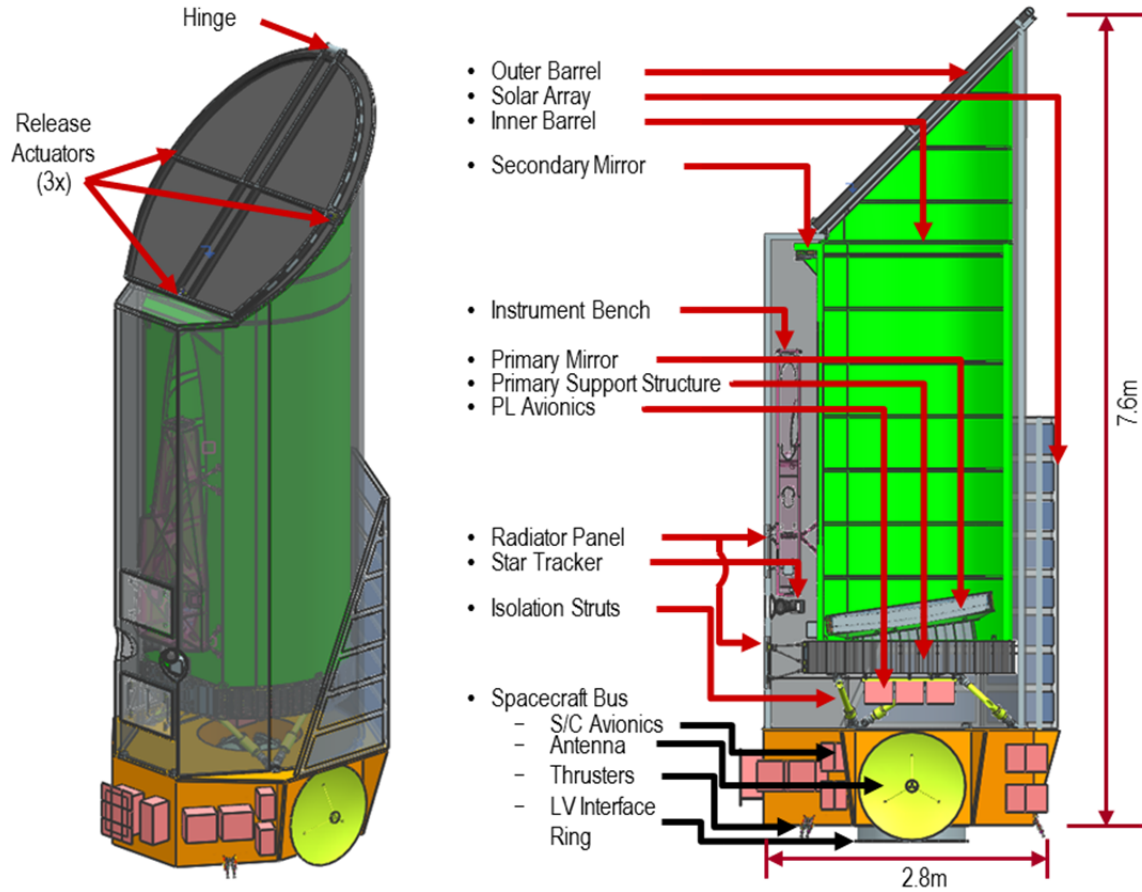


Figure 6.2-1. Baseline mechanical configuration.

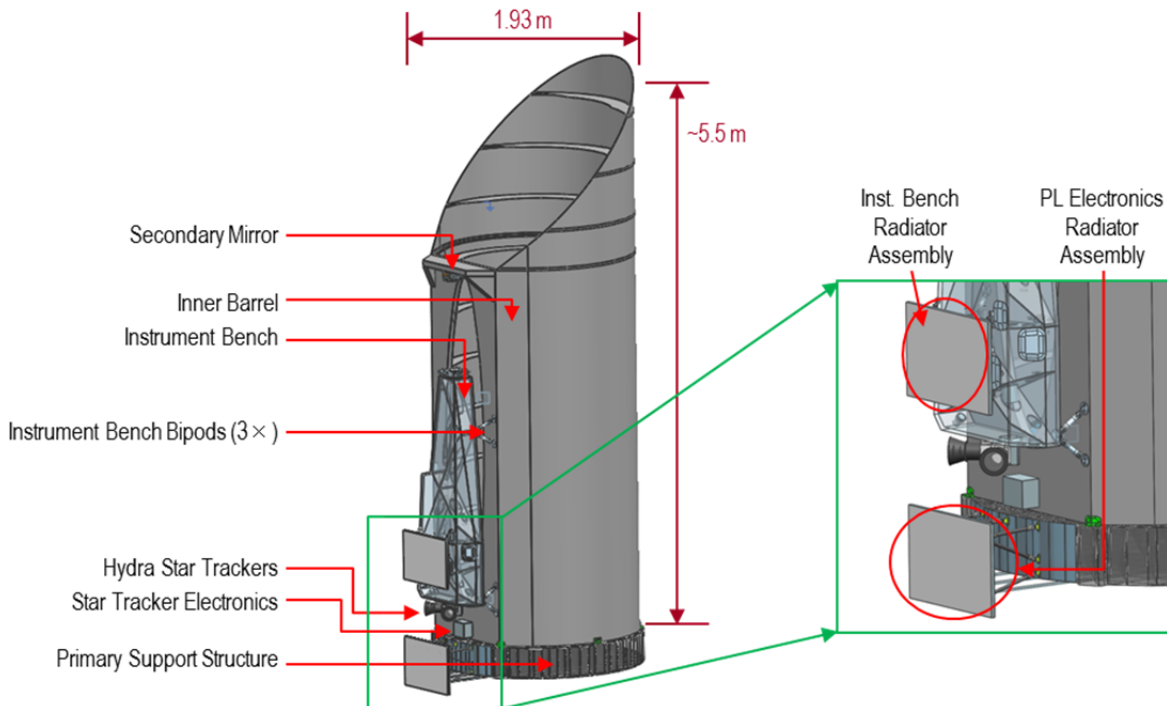


Figure 6.2-2. Inner barrel and instrument components.

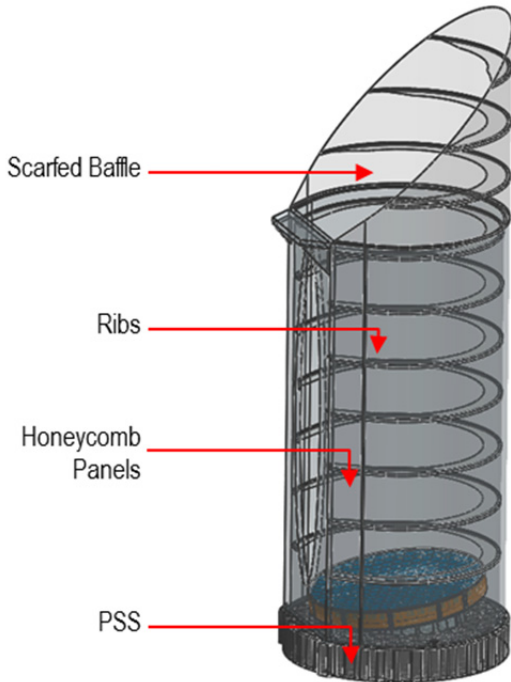


Figure 6.2-3. Inner barrel.

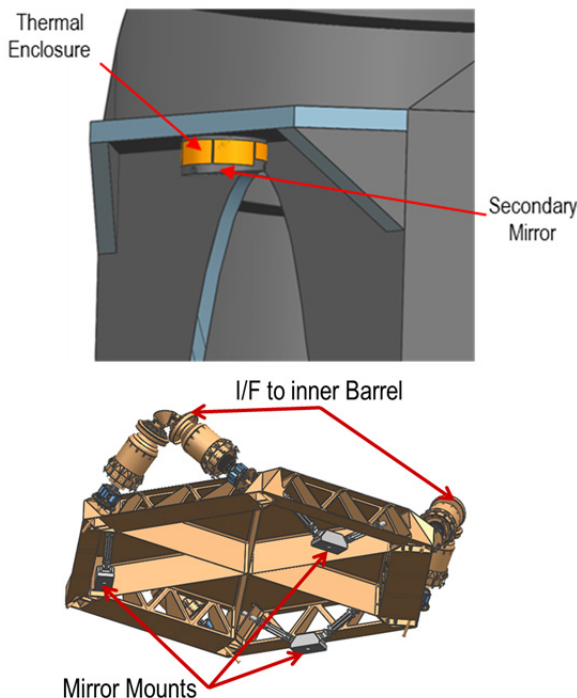


Figure 6.2-4. Secondary mirror assembly.

As shown in Figure 6.2-6, the outer barrel contains cutouts to accommodate the radiator volumes, as well as cutouts to allow the proper field of view (FOV) for the star trackers.

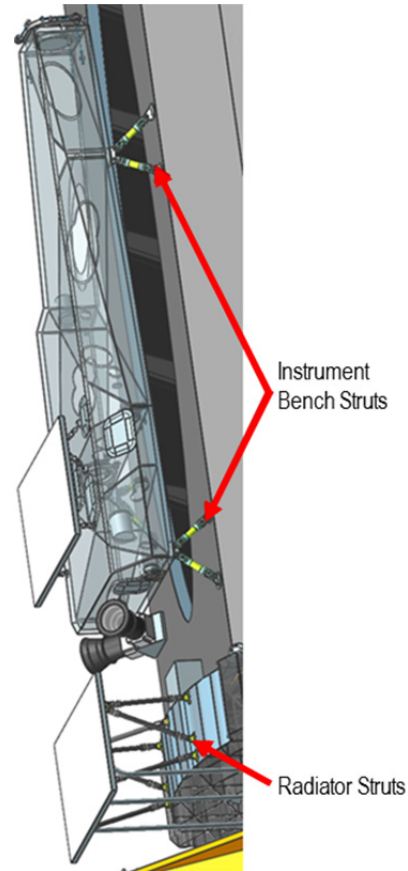


Figure 6.2-5. Instrument bench.

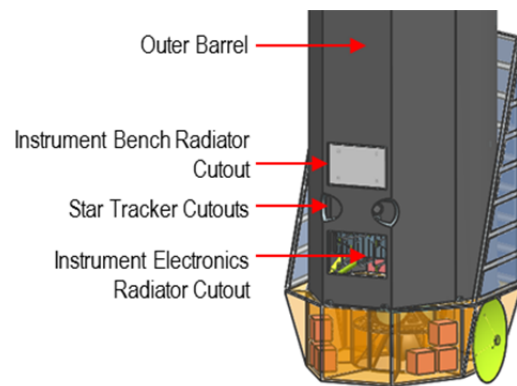


Figure 6.2-6. Outer barrel cutouts.

### 6.3 Payload Optical Configuration

The optical portion of the payload (Figure 6.3-1) comprises the telescope and instrument assembly. The instrument assembly has two main subsections: the wavefront control optics and the coronagraph. Within these two subsections, there are subassemblies that support their indicated function. The control

subsection contains a fine-guidance sensor (FGS) and a low-order wavefront sensor (LOWFS) used for pointing and wavefront error correction, respectively. The final focal planes are the imager and the integral field spectrograph (IFS).

The physical configuration of the payload is shown in Figure 6.2-5 and Figure 6.3-2. The instrument assembly is located laterally with respect to the telescope axis, in a plane parallel to the telescope axis and offset to one side. The volume available in this configuration for the packaging of the instrument assembly enables a minimum number of fold mirrors, and

provides for low angles-of-incidence (AOI) on all sensitive surfaces to provide the least impact to instrument performance (i.e., higher throughput, minimal polarization effect).

### 6.3.1 Payload Optical Block Diagram

The payload optical diagram is provided in Figure 6.3-1.

### 6.4 Telescope

The first two telescope mirrors (M1 and M2) are in an unobscured Cassegrain configuration, with the entrance pupil located at the primary. A field baffle for rejecting out-of-field light is located where a real image of the sky is formed

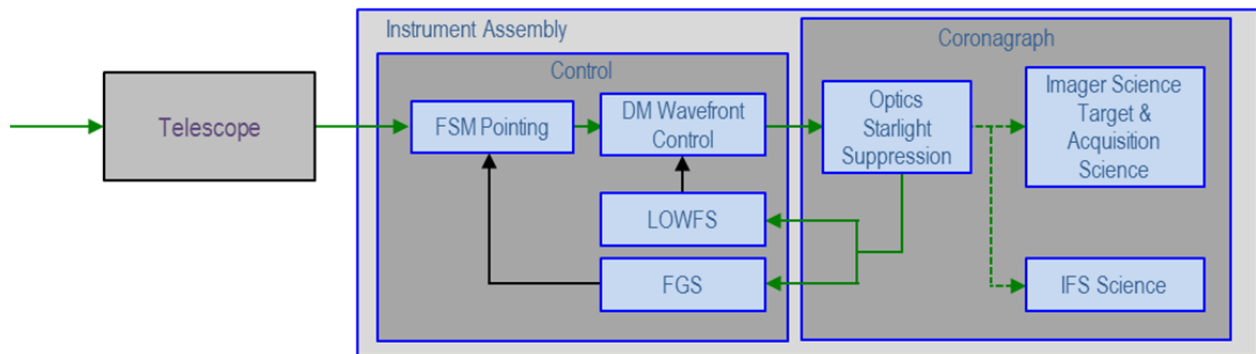


Figure 6.3-1. Optical system block diagram.

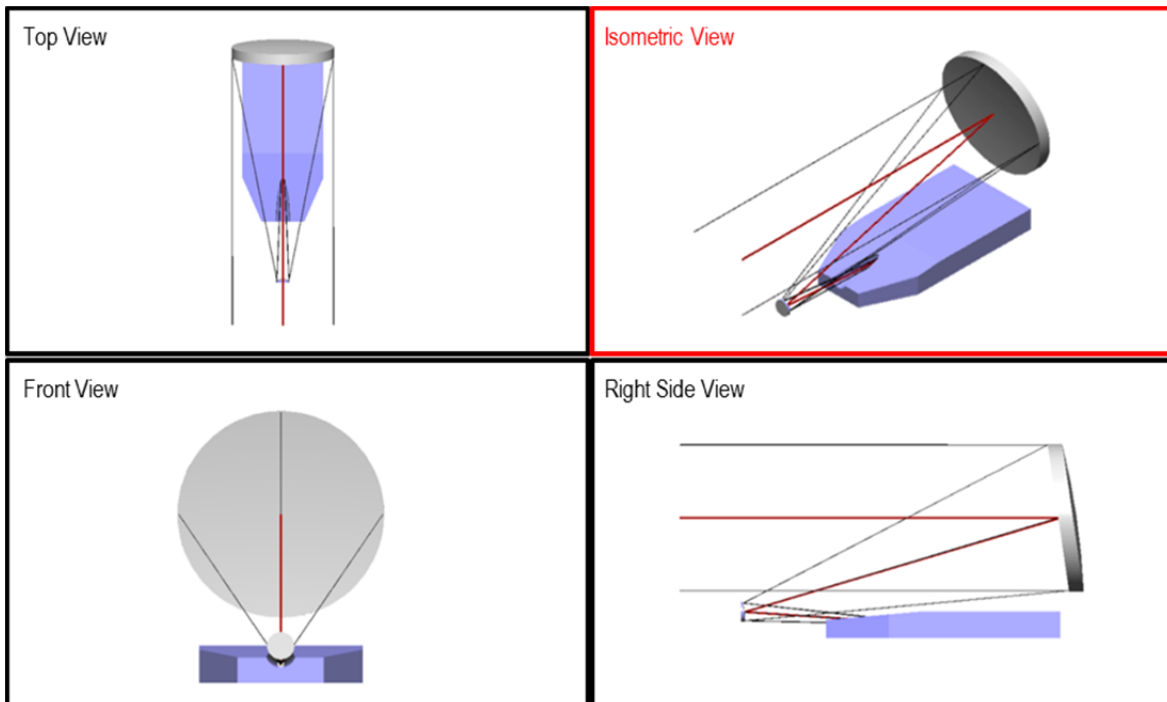
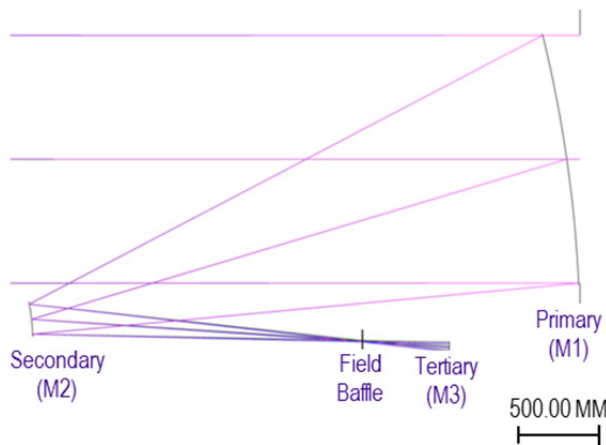


Figure 6.3-2. Baseline payload configuration of optics.

by the two mirrors, followed by a third mirror (M3) that recollimates the light and creates a real image of the pupil (See Figure 6.4-1).



**Figure 6.4-1.** Baseline telescope configuration. Raypaths following M3 not shown.

## 6.5 Instrument

### 6.5.1 Coronagraph

There are multiple candidate coronagraph technologies that provide varying degrees of contrast, inner working angle, and throughput. At this phase of the effort, detailed trades have not been performed to down select to any particular approach. However, a point design was needed to support the development of optical, thermal, mechanical, and performance models. The Hybrid-Lyot Coronagraph (HLC) was selected at this stage as its configuration is well studied and can serve as a useful tool for the development of our analysis approaches (Trauger et al 2012, and Trauger et al 2009). The following describes the elements, functions, and rationale for the baseline instrument coronagraph's optical system; refer to Figure 6.5-1.

Light from the telescope M1 and M2 mirrors enters from the left, focuses at the field baffle, and is recollimated by the telescope M3 to form a pupil image. This is followed by the instrument elements:

1. Deformable fold mirror 1/fine-steering mirror (DM1/FSM) located at the pupil image\*
2. Deformable fold mirror 2 (DM2)\*

3. Focusing mirror M4, which creates an image at
4. Coronagraph mask, which also splits off a portion of the light to\*
5. FGS/LOWFS
6. Collimating mirror M5, which forms a pupil image for
7. Lyot stop\*
8. Focusing mirror M6, creating an image through
9. Filter sets\*
10. Flip mirror, which selects the incoming beam
11. Imaging detector (flip mirror out) or
12. Integral Field spectrograph (IFS) (flip mirror in).

(\*) Discussion of selected elements follows.

All mirrors within the instrument are either flat (DMs, flip mirror) or off-axis concave paraboloids (conic constant = -1).

#### 6.5.1.3 Fine Steering Mirror

The FSM is located at the pupil image formed by the telescope. This mirror is used to stabilize the optical system line-of-sight for two purposes. First, it keeps the target star image centered on the coronagraph mask as the spacecraft attitude wanders within the limits of its control capability. Second, it minimizes the beam walk influences on wavefront error (*beamwalk: as the line-of-sight changes, the specific portion of an optical surface that light path covers varies slightly. This "walk" exposes the beam to slight changes in the surface imperfections, which subtly changes the wavefront error in the beam*).

#### 6.5.1.4 Deformable Fold Mirrors

DFM1 is used to provide wavefront control in a plane conjugate to the primary mirror (pupil). Next in the optical path is DFM2; the separation between the two DFM units allows the pair to provide a capability in wavefront control in both amplitude and phase domains, correcting minute wavefront errors due to fabrication and alignment inaccuracies in the system and facilitating the ability to achieve the deep ( $1e^{-9}$ ) contrast ratios for this instrument.

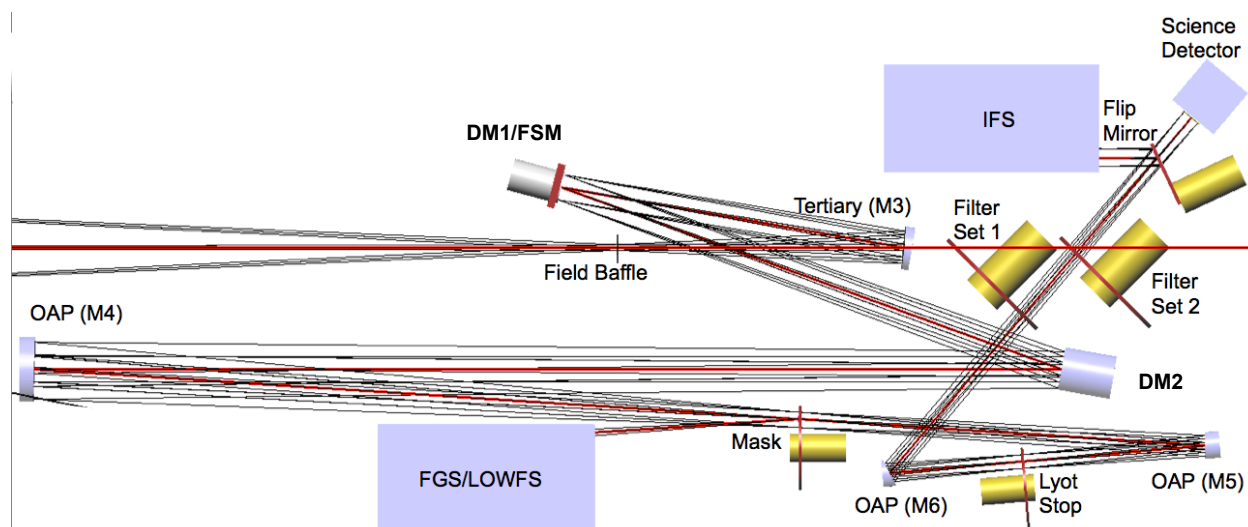


Figure 6.5-1. Baseline instrument optical layout.

### 6.5.1.5 Coronagraph Mask

The collimated beam reflecting off DM2 is then brought to a focus by M4. The primary coronagraphic element is placed at this focal plane, which in the case of our baseline is the hybrid-Lyot mask. Since the star image size varies by wavelength due to diffraction spreading, a single mask functions best (optimum blocking with minimum inner working angle) over a limited waveband. Hence, multiple masks are needed to provide the best occulting efficiency (contrast) over the full waveband. Our preliminary design has four overlapping bands which adequately cover the entire science wavelength range. We will evaluate broader band options if needed.

These masks are carried by a wheel mechanism, with the best mask rotated into position depending on the science waveband selected for observation. The hybrid-Lyot coronagraph uses a partially opaque spot to block the majority of the target star light; in our implementation, the mask is slightly tilted and the spot is made reflective. This reflected light is collected by the FGS/LOWFS; the elements of this module are discussed later in this section.

### 6.5.1.6 Lyot Stop

Like the mask, a single Lyot stop is most efficient (best contrast at best transmission) over a limited wavelength range; like the mask,

several Lyot stops are carried on a wheel mechanism, with the appropriate stop selected for the current observation. An implementation option exists here, however, to have only a single, non-mechanized Lyot stop sized to the best operation at the shortest wavelength. Such a stop would still provide good contrast at longer wavelengths, with the tradeoff being less light throughput than could be achieved with stops created specifically for those wavelengths.

### 6.5.1.7 Filter Sets

Two wheels carry multiple filters to select the various wavebands of interest for observation. Sufficient slots are present (eight per wheel) to have several slots in the wheels carry special elements other than filters: one neutral substrate in each wheel for a “null” effect that preserves system focus but does nothing else, a lens that creates an image of the pupil at the detector (“pupil-imaging lens”), an opaque disk to act as a shutter (“blocker”), and optionally polarizers in various orientations to permit polarimetric data collection

### 6.5.2 Fine-guidance Sensor

The FGS is part of the FGS/LOWFS module. It consists of four elements: a relay optic<sup>1</sup>, a

<sup>1</sup> This subsystem has not been detail designed at the time of this writing. One may safely proceed with the understanding

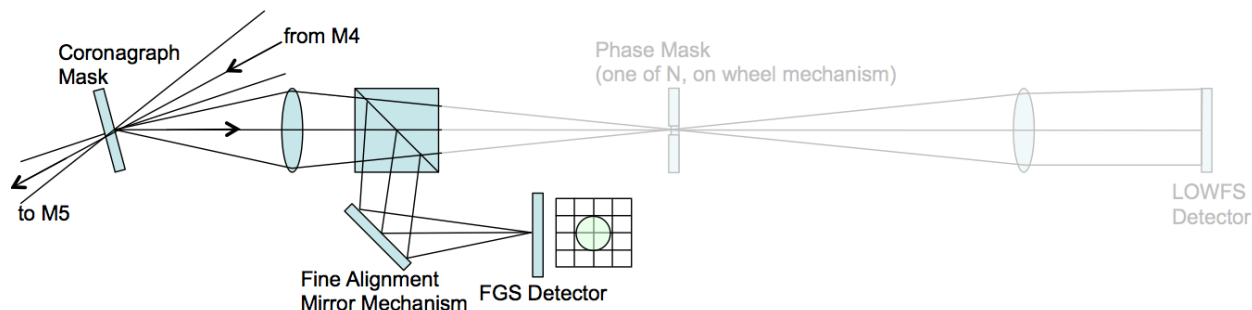


**Figure 6.5-2.** FGS portion of FGS/LOWFS module.

beamsplitter (shared with the LOWFS path), a fine alignment mirror, and a detector, as illustrated in Figure 6.5-2.

Once the spacecraft has been slewed to a target star and stabilized, an acquisition process results in the star being centered on the coronagraph occulting mask, and the star light reflecting off the mask. This light is reimaged by the relay optic onto the fine guidance detector; the centroid of the star image is monitored, and any motion creates an error signal that feeds back to the FSM to correct. Running in such a nulling loop makes the system insensitive to detector non-uniformities, optics distortion, and aberrations.

### 6.5.3 IFS

The IFS functions to provide spectrographic information simultaneously about multiple objects in the field-of-view. Following Figure 6.5-3, light focused by M6 is intercepted by the flip mirror and reflected into the IFS module.

The IFS module samples the field with a lenslet/pinhole array pair. Light passed through the pinholes is collimated, dispersed, and the resulting spectra focused onto the IFS detector.

The axis of the dispersing element is rotated compared to that of the lenslet/ pinhole array, preventing overlapping of spectra from adjacent samples (Foldout 6-1B<sup>2</sup>). By appropriate selection of focal lengths and disperser properties

needed to work with a selected detector, a spectral resolution of 70 is achieved.

### 6.5.4 Detectors

The Exo-C instrument's science subsystems are the imager and the IFS. Each of these instruments requires its own detector. In addition, the LOWFS and FGS employ array detectors. The requirements on these detectors are significantly varied, and in this section we discuss the status of each.

#### 6.5.4.3 Requirements for the Detectors

The primary functional requirements of the detectors are summarized in Table 6.5-1.

**Table 6.5-1.** This table lists the main detector requirements for each of the four detectors.

Requirements	Imaging	IFS	LOWFS	FGS
Minimal Format	2K × 2K	4K × 4K	64 × 64	64 × 64
Sensitive Range	0.45–1.0 μm	0.45–1.0 μm	0.45–0.80 μm	0.45–0.80 μm
Special Modes	256 × 256 central readout	2 × 2 binning support		50 fps readout
Special Features	Minimal blooming			

The performance requirements of these detectors are functions of the signal-to-noise ratio (SNR) and the time available to achieve the required SNR. A basic model is being developed to provide a traceable quantitative link between the detector performance requirements and the higher level constraints. Besides the scene characteristics, SNR is most sensitive to the detector characteristics of quantum efficiency (QE), read noise, dark current. Since Exo-C targets will be very dim (typically  $1e^{-9}$  of the host star in brightness),

that the relay optic will be a mirror, and will operate no higher than unit magnification.

<sup>2</sup> Source: STDT presentation “Internal Coronagraph Imaging Cameras, McElwain, 7/21/2013.

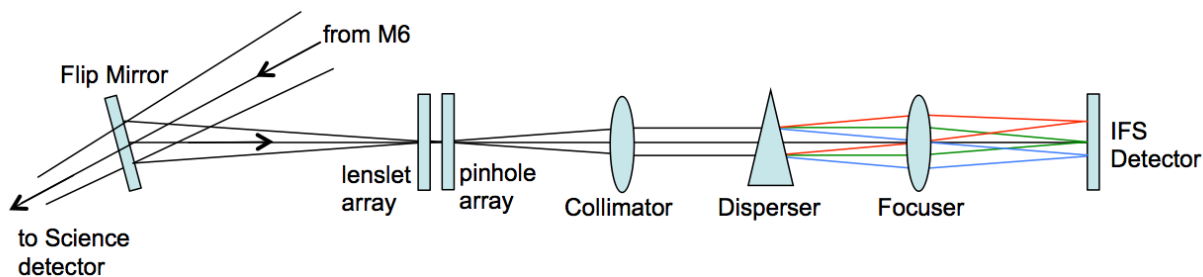


**Figure 6.5-3.** Schematic layout of the IFS. The lenslet/pinhole arrays separate the field such that the subsequent collimator, disperser, and focuser produce a spectrum for every lenslet.

photon rates are exceedingly low (order 0.01 e/s or less), and it is very likely that ordinary charge coupled devices (CCDs) will have a read noise that is too high to accommodate the science needs of Exo-C. As such, electron multiplication CCDs (EMCCDs) will be needed (see Figure 6.5-4).

These are currently the leading choice for the Wide Field Infrared Survey Telescope-Astrophysics Focused Telescope Asset (WFIRST-AFTA) coronagraph’s imaging cameras (the imager and the IFS). EMCCDs are similar to regular CCDs, except that they employ an extended multiplication register (also referred to as a gain register) with a high-voltage phase (typically around 40 V) where electrons undergo an avalanche multiplication process as they move across the stages. The probability for getting an extra electron at each stage is low (typically < 2%), but the cumulative effect can be quite high. For example, a gain register with 600 stages and a single-stage multiplication probability of 1.5% can have a gain of  $(1 + 1.5\%)^{600} \approx 7500$ . Lower voltages produce lower gain.

A drawback of EMCCDs is that the electron multiplication process is stochastic in nature, introducing its own noise. This is referred to as “excess noise factor” (ENF) in the literature, and asymptotically approaches  $\sqrt{2}$  for large enough gains (> 10 or so).

Since the LOWFS and the FGS will be using the starlight, the requirements are very different, and other choices are more appropriate. Here CCDs can be viable, as well

as scientific complementary metal-oxide-semiconductor (CMOS) sensors, among others.

Preliminary results from the model under construction suggest the following detector performance numbers (Table 6.5-2), assuming EMCCD technology.

**Table 6.5-2.** Preliminary detector performance requirements..

Requirements	Imaging	IFS	LOWFS	FGS
Baseline Detector	EMCCD	EMCCD	CCD	sCMOS
QE at red	> 80%	> 80%	> 50%	> 50%
Read Noise	< 0.1 e-	< 0.05 e-	< 3 e-	< 3 e-
Dark Current	< 0.001 e-/pix/s	< 0.0005 e-/pix/s	< 0.01 e-/pix/s	< 0.01 e-/pix/s
Frame Rate	1/300 fps	1/10 fps (ph. ctg.)	1/30 fps	50 fps

These numbers and baselines are, of course, preliminary at this stage. We plan to produce a model that predicts the performance of each of these sensors and using this model we plan to perform a trade study over detector architectures. Additionally, the WFIRST-AFTA detector development currently under way will help inform our decision as to the best detectors for Exo-C.

### 6.5.5 LOWFS

#### Executive Summary

The dominant source of wavefront drift is expected to be body-pointing errors, which the pointing control architecture is designed to remove with a fast-steering mirror (FSM) in closed loop with the FGS. The implementation of the line-of-sight control loop will be addressed in §6.7 Pointing Control Architecture and will not be addressed here. Higher order wavefront drift due to changing thermal loads

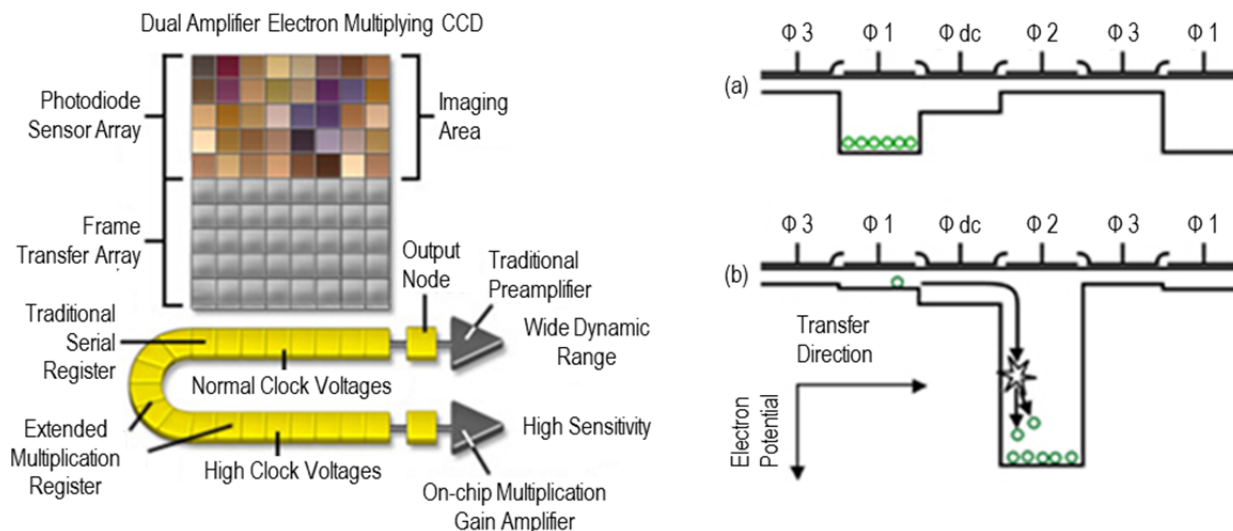


**Figure 6.5-4.** Typical EMCCD architecture (left), showing the multiplication register, where electron multiplication occurs (right) during each transfer.

is, however, expected to significantly degrade the dark field speckle during individual exposures. Although each coronagraph design has different sensitivities to wavefront drift, all coronagraph designs will likely require an LOWFS in closed loop with the deformable mirrors to maintain contrast levels of  $10^{-9}$ .

#### 6.5.5.1 Introduction

The  $10^{-9}$  contrast dark field produced by the coronagraph is initialized by driving deformable mirrors to minimize the speckle on the imaging camera. After initialization, light from the central star will be suppressed to  $10^{-9}$  contrast within the dark field and it will be necessary to maintain stability of the speckle to  $10^{-10}$  contrast for the duration of the exposure. To image faint planets it is expected that single exposures will be limited by the background noise sources to about an hour. When longer integration times are needed, the dark field can be reinitialized between exposures and multiple exposures can be stacked to increase the signal-to-noise ratio. During the exposure (whether using the imaging camera in the discovery phase of the mission or using the IFS during the characterization phase of the mission) the speckle drift must be maintained at the  $10^{-10}$  level without reference to the imaging camera readout. The LOWFS is used

in closed loop with the deformable mirrors to maintain the dark field at the imaging camera or IFS. Since its role is simply maintenance, it is insensitive to calibration errors.

While in principle the wavefront drift asymptotically approaches zero for a telescope in Earth-trailing orbit when the solar angle is constant, in practice there is still significant wavefront drift for 12 hours after slewing the telescope to a new target. Rather than waiting long periods for thermal equilibrium, the deformable mirrors can be used to correct the wavefront drift during the exposure if a suitable wavefront sensor is employed. The dominant wavefront error (WFE) sensitivities in order of decreasing significance are focus, astigmatism, and coma; however, high-order Zernike modes can mimic planets and be difficult to subtract in post processing.

#### 6.5.5.2 WFS Architecture

The imaging camera and the IFS are not well suited for wavefront drift measurements because the suppression of the central star means very few photons are available on these cameras. For coronagraphs employing a focal-plane mask or other optical element such as a vector vortex, it is most effective to pick up light from the central star at an image plane upstream of the focal-plane mask where

photons are plentiful. This approach will be taken for both the FGS and the LOWFS. While line-of-sight error is sensed by the LOWFS, the line-of-sight drift is better handled by the dedicated FGS in a high bandwidth loop with a FSM in order to suppress not only the thermal drift of the optics but also body pointing errors and jitter. This division of function allows us to optimize the LOWFS for slowly varying WFE terms. Figure 6.5-5 is a schematic layout of a representative LOWFS and its relation to the FGS and the occulting mask.

To sense WFE beyond the tip tilt and focus terms, it is necessary to sample the wings of the central star's PSF. A dichroic layer can be selected that reflects out-of-band light for use by the LOWFS and FGS. In the example of a Zernike Wavefront Sensor (ZWFS) version of the LOWFS shown in Figure 6.5-5, both the deformable mirror and the detector are in the pupil plane so the detector is sized to match the actuator count of the deformable mirror.

Visible nuller coronagraphs differ from the example in that they do not utilize a focal plane mask. Light from the central star is, however, readily available in the arms of the interferometer for use by the LOWFS. The two arms can be combined in a Pupil Plane Mach-Zehnder Wavefront Sensor (PPMZWFS), for example.

#### 6.5.5.3 WFE Drift Requirements

The WFE drift requirements are derived from the residual speckle stability requirement of  $10^{-10}$  contrast drift over 48 hours. Modeling of

the Exo-C configuration will convert the contrast stability requirements into WFE drift requirements broken down into Zernike components and weighted by the impact each Zernike term has on planet detection. Preliminary models of the Exo-C design indicate that the benign earth trailing orbit in combination with careful mechanical and thermal design reduce the WFE drift rate to manageable levels within a few hours of slewing to a new target.

#### 6.5.5.4 Conclusion

Thermal transients lasting many hours degrade the dark field during long exposures. Wavefront sensing of light from the central star in a closed loop with the deformable mirrors can be used to mitigate the detrimental effects of the thermal drift.

#### 6.5.6 Field Layout

The instrument has a  $1 \times 1$  arcmin FOV which ensures that the target star will be acquired after spacecraft pointing maneuvers (assuming a maximum 30 arcsec uncertainty between star tracker and instrument lines-of-sight). While the FGS has a comparable field-of-regard, its acquisition is achieved by scanning its much narrower FOV via a mechanism; with the instrument FOV supporting initial acquisition, a more efficient timeline is supported.

The portion of the FOV required for science operations is significantly smaller than the total instrument capability; the nominal outer working angle (OWA) within which sufficient starlight

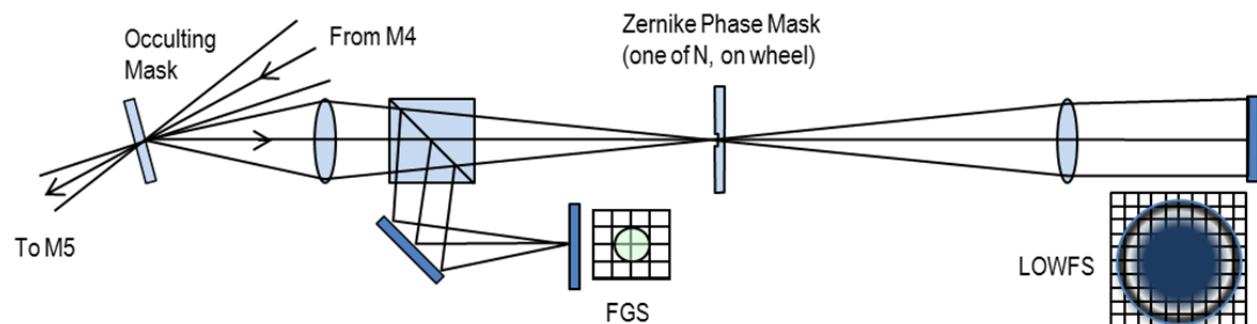


**Figure 6.5-5.** Star light is focused on the occulting mask having already been conditioned by the deformable mirror optics. In-band light is passed to the coronagraph and out-of-band light is reflected to the FGS and LOWFS. In this example, a ZWFS is employed as the LOWFS.

suppression occurs is 1.9 arcsec (radial), equivalent to  $\sim 1/32$  of the instrument FOV.

The utility of this FOV is illustrated by considering a Solar System equivalent 10 parsecs away. The apparent angular separation from the star of selected equivalent features, along with the relevant instrument properties, would be (Table 6.5-3):

**Table 6.5-3.** Apparent angular separation.

Instrument Property	Solar System Equivalent	Angle (arcsec)
PSF Core(*)		0.12
Inner Working Angle		0.14
	Mars orbit (1.5 AU)	0.15
	Jupiter orbit (5.2 AU)	0.52
	Neptune orbit (30 AU)	3.0
Outer Working Angle		1.9
	Kuiper belt (30–50 AU)	3.0–5.0

(\*) The PSF core is computed for a central 700 nm wavelength.

From this, it can be seen that, for our example system, nothing closer than a Mars orbit equivalent can be detected due to the inner working angle (IWA) limit. On the outermost side, observations of a Kuiper belt equivalent falls outside the OWA.

Figure 6.5-6 illustrates how the example system would appear to an idealized instrument (if seen from 90° above the orbital

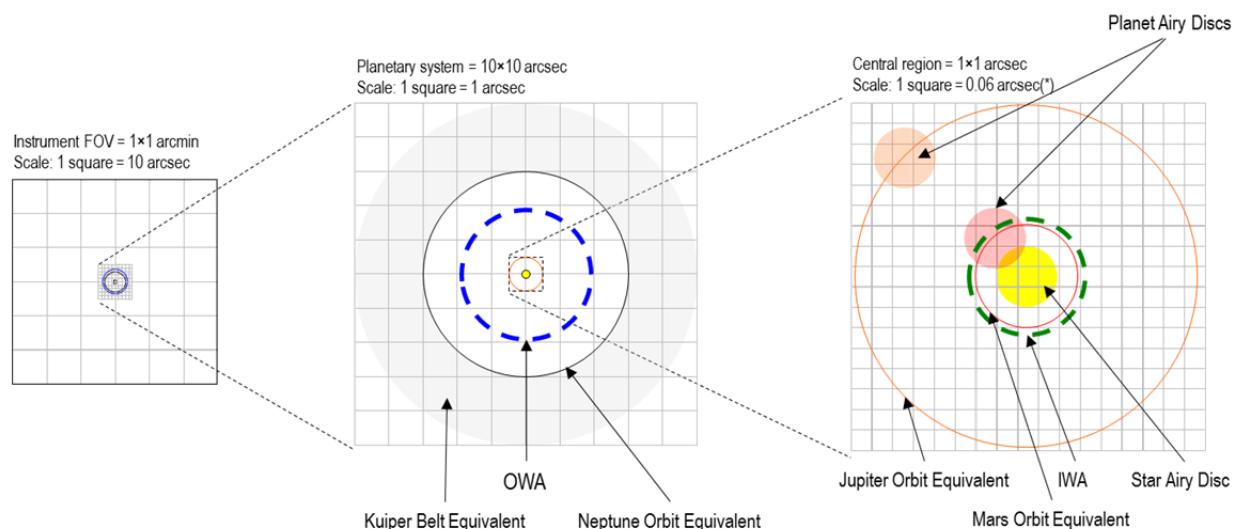
plane). Also shown is how the central zone would be sampled by a detector consisting of an array of  $1000 \times 1000$  pixels. It is significant to note that the PSF cores cover an area of  $3 \times 3$  pixels, which provides for sub-pixel centroiding of targets, supporting the ability to determine orbital parameters.

## 6.6 Thermal

### 6.6.1 Telescope

The purpose of the payload thermal control system is to maintain temperatures within limits to enable science performance and hardware safety. To meet science objectives, the thermal control system needs to drive thermo-elastic distortions down to acceptable levels within acceptable time periods. This is accomplished by minimizing the effect of thermal disturbances, both environmental and bus-based, while also applying active temperature control through a cold-bias/heater system.

The heliocentric, Earth-trailing orbit baselined for Exo-C is associated with extremely small planetary-based thermal loads, and the thermal design focuses on minimizing disturbances from varying incident solar loads. See modeling results of section 6.10. This is accomplished through the outer barrel



(\*) equivalent to 1 pixel on a  $1000 \times 1000$  pixel array

**Figure 6.5-6.** Idealized instrument view of example system. The IWA and Airy disks are evaluated at a wavelength of 550 nm. The OWA is evaluated at a wavelength of 800 nm.

assembly, which serves as a solar radiation shield. The outer diameter is covered with multi-layer insulation. The external layer minimizes solar absorption and resulting temperature increases. The inner diameter is also covered with multi-layer insulation.

The inner barrel assembly serves as the secondary metering structure. It is actively temperature controlled to maintain its dimensional stability and to provide a more constant temperature environment for the primary and secondary mirror surfaces, when subjected to varying solar incidence angles. Atop both barrel assemblies is a scarfed solar shield to allow up to 45° off-Sun pointing.

Active heater control is also employed through radiative heating of the primary and secondary mirrors to reduce wavefront drift errors to acceptable levels within settling times of a few hours. The set-point temperature of the inner barrel is at room temperature rejects dissipations from payload electronics. The instrument bench runs at < 250 K and is used to maintain detector temperatures. The electronics dissipations are transported to the radiator via constant conductance heat pipes, while the detectors are sufficiently close to the radiator such that a solid-state link is used to transport waste heat.

## 6.7 Pointing Control Architecture

### 6.7.1 Introduction

A small inner working angle on a coronagraph is only useful if the image of the star can be centered on the field coronagraph to within a few percent of the IWA and maintained there over the entire exposure. While the pointing accuracy and stability is challenging for the Exo-C coronagraph, the techniques for achieving the required accuracy and stability have high heritage. A flight proven pointing control architecture is proposed for Exo-C, which meets the science objectives.

### 6.7.2 Pointing Architecture

A review of the state-of-the-art in pointing technology for relevant space observatories, Spitzer (Bayard et al. 2004), Kepler (Koch et al. 2004), and Hubble (Sharkey et al. 1992), and recent coronagraph studies, AFTA (Spergel et al. 2013), and the Extrasolar Planetary Imaging Coronagraph, EPIC, (Champin et al., 2009), leads to a flight proven pointing architecture that builds upon previous experience. It employs a two-stage pointing architecture with telescope pointing achieved by the spacecraft attitude control system (ACS) while precision pointing and jitter rejection is achieved with a fast-steering mirror (FSM) in the payload.

The key features of this architecture are:

- **Fine Guidance Sensor (FGS).** The FGS, located in a telescope focal plane, provides high rate pointing measurements with respect to the science target star.
- **Fast Steering Mirror (FSM).** A high bandwidth FSM compensates for residual spacecraft pointing errors and keeps the coronagraph centered on the science target star.
- **Earth-trailing orbit**  
As was demonstrated by Spitzer and Kepler, an Earth trailing orbit provides a stable environment, where the only exogenous disturbance is the solar flux. This orbit selection mitigates pointing disturbances associated with eclipse induced thermomechanical snaps, gravity gradients, and aerodynamic drag associated with Earth orbit.
- **Observatory structural design.** The spacecraft structural design is as rigid as possible to eliminate control structure interactions (CSI) between the control loop and the vibration modes of the structure. It does not have any deployable or articulated structures. For example, the telescope cover is ejected

upon reaching orbit. A preliminary rendering of the Exo-C observatory is shown in Foldout 6-1.

- **Passive Isolation.** Passive isolators at the reaction wheels and at the payload-to-spacecraft interface mitigate high frequency jitter introduced by reaction wheels.
- **Enhanced spacecraft ACS.** The spacecraft ACS is enhanced with a fine guidance signal from the instrument that provides precise pointing information derived from the FGC.

Figure 6.7-1 shows the pointing control system diagram for this architecture.

The diagram depicts the two-stage pointing architecture of the spacecraft ACS and the payload pointing system. The spacecraft ACS is a three-axis attitude stabilization system composed of star trackers and an inertial reference unit mounted on the payload side to sense the telescope attitude and reaction

wheels (mounted on passive isolation) to correct the spacecraft attitude. It also includes a propulsion system that is used for momentum desaturations (not shown in the block diagram). As was done in Hubble and Kepler, a fine-guidance signal from the payload is used to improve attitude determination. A spacecraft isolator further isolates the reaction wheels from the payload.

As was proposed in the ACCESS study (Trauger et al. 2009), the payload pointing system is composed of the FGS, an FGS alignment mirror to align the center of the target guide star to within the cross hairs of four pixels, and the FSM. The FSM control set-point is centered on the target star by use of the imaging camera.

### 6.7.3 Pointing Requirements

Coronagraphic missions call for high precision pointing to mitigate contrast degradation due to errors in centering the coronagraphic instrument on the target star and errors due to

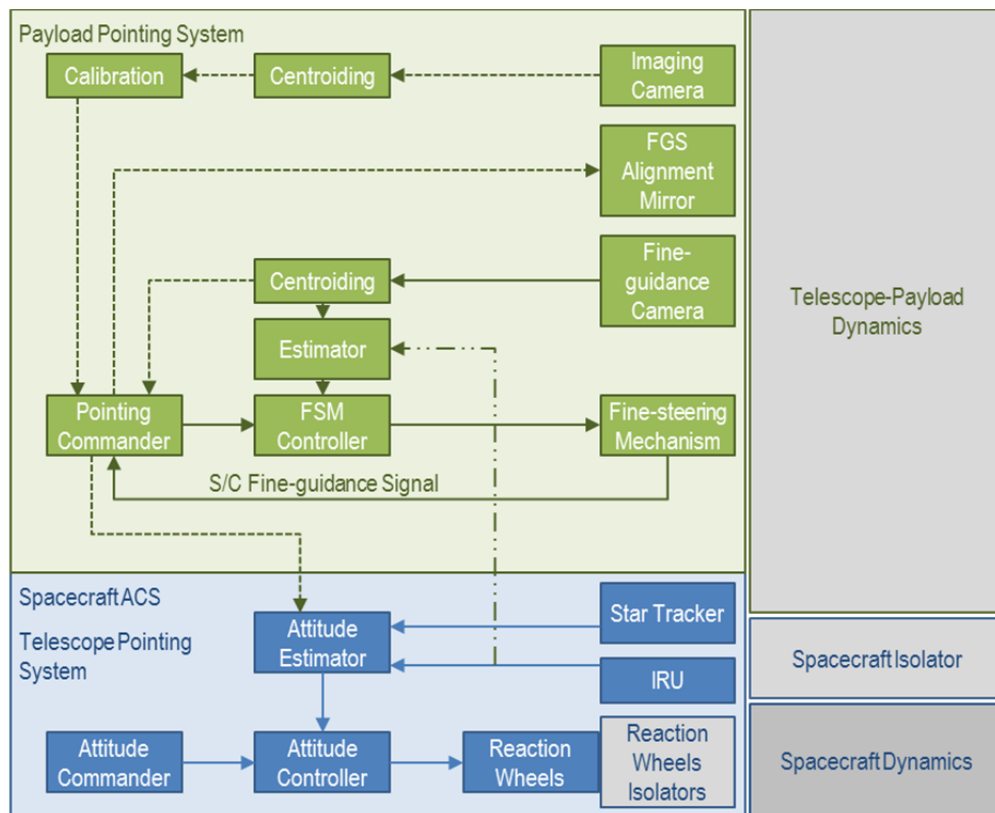


Figure 6.7-1. Pointing control system diagram.

beamwalk on the optics ahead of the FSM.

The proposed pointing requirements are derived from analysis of pointing performance from Kepler, Spitzer and Hubble, and from bounding models of the isolators and FSM pointing loop (Table 6.7-1):

**Table 6.7-1.** Accuracy and stability requirements for the spacecraft pointing and fine guiding.

Pointing Requirements	
Telescope Pointing (Angle in the sky, 1σ RMS)	
Accuracy	1.2 milliarcsec (Line-of-sight tip/tilt) 10 arcsec (Line-of-sight roll)
Stability (1000s)	6 milliarcsec* (Line-of-sight tip/tilt) 10 arcsec (Line-of-sight roll)
Instrument Pointing (Angle in the sky, 1σ RMS):	
Accuracy	0.08 milliarcsec (Line-of-sight tip/tilt)
Stability (1000s)	0.4 milliarcsec (Line-of-sight tip/tilt)

The telescope pointing error stability requirement (Table 6.7-1) has a PSD bound associated with it (Figure 6.7-2). Note that the area under the PSD matches the 6-milliarcsec RMS requirement.

### 6.7.4 Heritage

The proposed architecture leverages flight-

proven technology and lessons learned from seven previous missions notably Kepler, Spitzer, and Hubble. Table 6.7-2 summarizes this heritage.

## 6.8 Electrical Configuration

The Exo-C payload electronics are distributed into three separate electronics boxes: the Payload Processing Electronics (PPE), telescope Thermal Control Electronics (TCE) and Instrument Control Electronics (ICE). The PPE is the brains of the instrument, providing the processing power and commands to control the instrument thermal and mechanical drivers, as well as bringing in and processing data taken from the sensors. The TCE and ICE house the thermal and mechanical sensors and drivers. These units take in commands from the PPE via a 1553 interface and perform the necessary functions required to control the instrument and telescope.

The PPE contains one backplane and seven different circuit boards. The Processor board provides the interface to the spacecraft electronics and performs all the processing needs of the instrument, including any

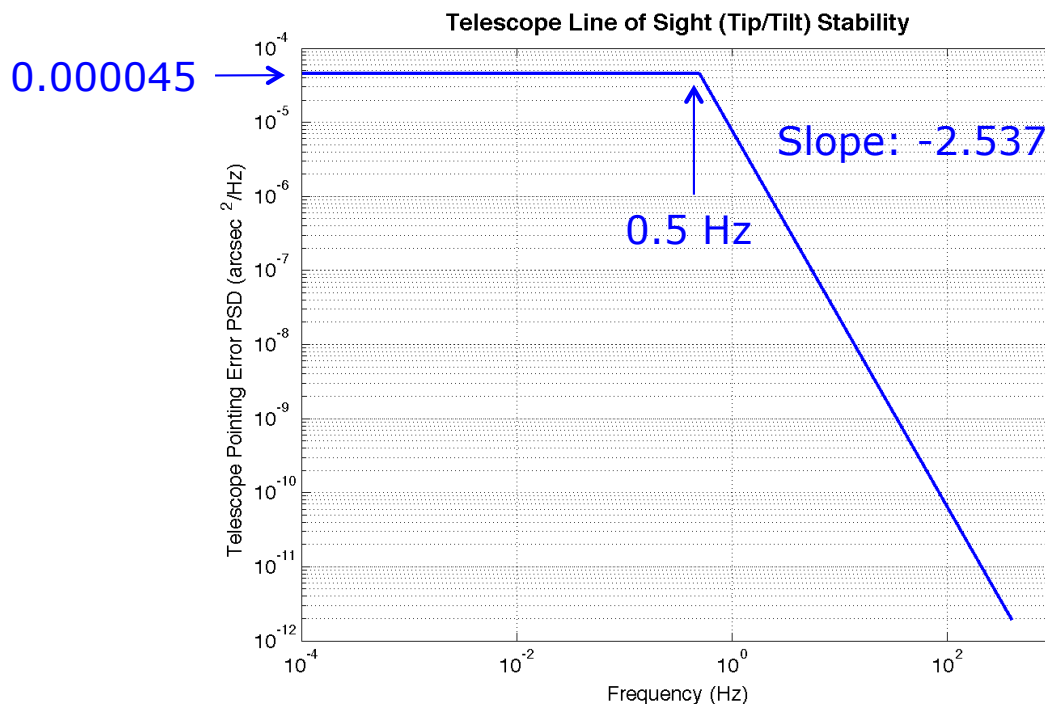


**Figure 6.7-2.** Telescope line-of-sight (tip/tilt) PSD stability bound.

**Table 6.7-2.** Flight heritage of the Exo-C pointing control system. IRAS (De Pontieu et al. 2014), PICTURE (Mendillo et al. 2012), Kepler (Koch et al. 2004), Spitzer (Bayard et al. 2004), Chandra (Weisskopf et al. 2003), Hubble (Sharkey et al. 1992), and TRACE (Handy et al. 1998).

Key Features of the Pointing System	Exo-C	IRIS SmEx (2013)	PICTURE Sounding Rocket (2011)	Kepler Discovery (2009)	Spitzer (2003)	Chandra (1999)	Hubble (1990)	TRACE SmEx (1990)
FGS	X	X	X	X	X	X	X	X
High bandwidth fast-steering mechanism	X	X	X					X
Enhanced ACS using FGS	X	X		X		X	X	X
Passive Isolation	X					X	X	
Low disturbance Earth-trailing orbit	X			X	X			
High stiffness observatory (no deployables/articulations)	X			X	X			

compression, analysis and sequencing for the instrument. Interface boards and memory are included in the PPE. The PPE provides the necessary interfaces and data for the other electronics boxes.

The TCE and ICE contain the necessary drivers to control the telescope and the instrument respectively. The TCE contains a number of thermal control electronic boards for each thermal zone of the telescope. This allows for customizable control of the thermal environment throughout the telescope.

The ICE provides the thermal control of the instrument starting from the secondary onward as well as the mechanical driver boards that control the instrument's filter wheels. The separation of the instrument and telescope functions enables a modular approach to developing, integrating, and testing the instrument and telescope.

## 6.9 Interfaces

The Exo-C telescope and instrument are designed to be as isolated from the spacecraft as possible. The only interfaces to the telescope lie within the mechanical isolators that mount the telescope to the spacecraft and the communications and electrical interface providing the instrument with power, commanding and transmitting processed data. The entire payload has been designed to be thermally isolated from the spacecraft bus.

### 6.9.1 Isolators

The mechanical isolators consist of six isolators that mount to the base of the telescope attaching to the spacecraft bus. These isolators are responsible for dampening out any vibration induced by the spacecraft during science observations.

### 6.9.2 Electrical

An electrical interface will go across the isolator, between the instrument and spacecraft. It will carry power and command information to the instrument, and return processed data for down-link back to the spacecraft.

## 6.10 Payload Structural Thermal Optical Performance Modeling

This section highlights preliminary results of integrated Structural, Thermal, and Optical Performance (STOP) modeling of the Exo-C Instrument Payload. Detailed mechanical and thermal models were developed in order to analyze system performance in response to characteristic orbital maneuvers.

Quasi-static WFE was computed as a function of time for each maneuver. The WFE was broken down into constituent components (optical aberrations) to compare with the rejection capabilities of a notional LOWFS and DM adaptive optics system. The contributions modeled here include effects from thermal-mechanical deformations only; dynamics are

included in the pointing and control models. Preliminary results are promising, indicating that WFE due to orbital maneuvers is dominated by low order aberrations, which the adaptive optics system is designed to correct.

The design team analyzed system performance against two characteristic orbital maneuvers. The first maneuver, a  $45^\circ$  slew, is characteristic of a slew between two successive science targets (Figure 6.10-1). When slewing between science targets, it is important that the instrument payload reaches thermal and structural steady state quickly (within a few hours) to minimize the impact on science observation time. The second maneuver, a  $30^\circ$  roll (Figure 6.10-2), is characteristic of the maneuver used to resolve an exoplanet from the instrument background noise. For this maneuver to be successful, wavefront error stability must be strictly maintained by the LOWFS and DMs as the telescope is rotated around its boresight axis.

As shown in Figure 6.10-3, detailed finite element models (FEMs) were developed to

model structural deformations of the inner barrel (IB), the PSS, the primary mirror (PM), and the primary mirror bipods (PMB).

The baseline thermal design, presented in §6.6.1, calls for a passive outer barrel and actively heated inner barrel to minimize structural deformations due to variations in solar loading. The primary and secondary mirrors are radiatively heated. The thermal response to each characteristic orbital maneuver was modeled using thermal analysis software.

Then the thermal transient responses were imported into the structural FEM and rigid body motions of the PM and secondary were modeled along with the surface figure error of the primary mirror. MACOS modeling of the optical configuration from the pupil plane to the coronagraph mask indicate that the WFE will be dominated by contributions of the PM and SM. Early indications are that without thermal control, waiting for the thermal transient to die down will take up an excessive fraction of the mission.

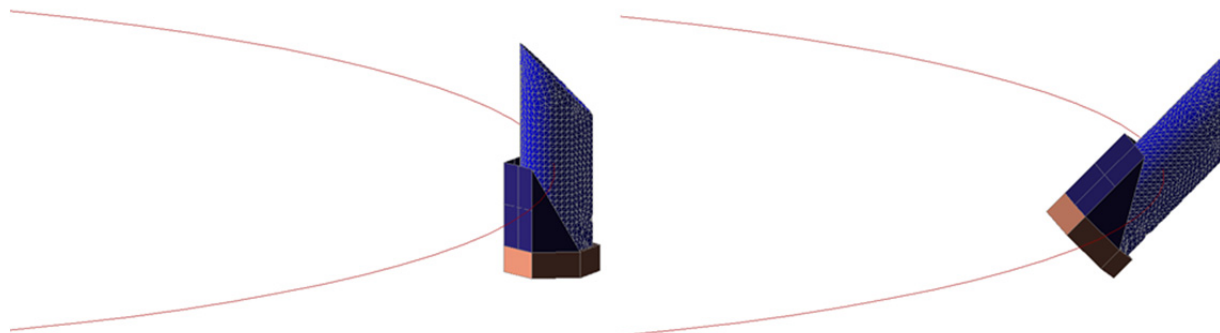


**Figure 6.10-1.** A slew of  $45^\circ$ , characteristic of a maneuver between two successive science targets.

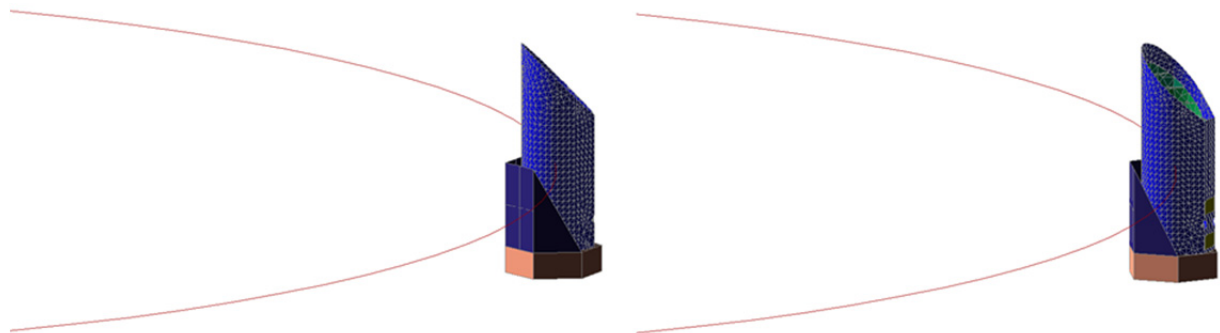


**Figure 6.10-2.** A roll of  $30^\circ$ , characteristic of a maneuver used to resolve an exoplanet from the background noise.

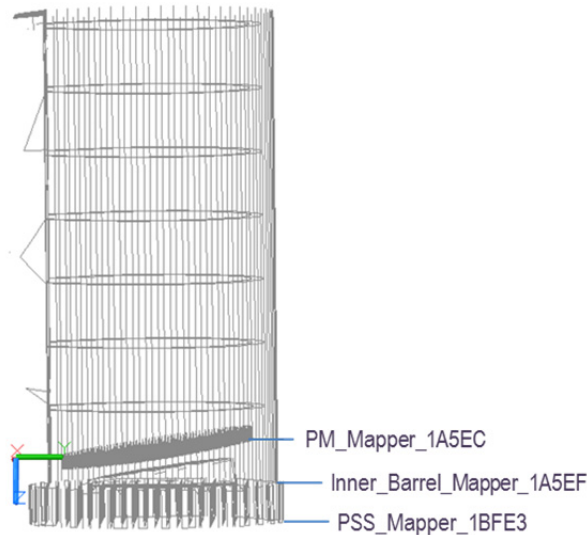


**Figure 6.10-3.** FEM used to map temperature data to mechanical deformations. The PM Bipods are included in the FEM but not shown in this figure.

The surface figure error and the rigid body motion induced WFE were then broken into their constituent Zernike WFE terms for more detailed evaluation. The preliminary results suggest that even the extreme case of a  $45^\circ$  pitch maneuver the thermal control system has reduced the WFE drift contributions of the primary and secondary mirrors to a range easily within deformable mirror stroke allocated for wavefront drift control. The focus term dominates the WFE; its source is predominately drift in the separation between the primary and the secondary mirrors. The wavefront drift rate quickly falls below the control bandwidth of the LOWFS/DM loop.

The different coronagraph architectures have different sensitivities to the different modes of the WFE, but all three coronagraphs meet the  $10^{-10}$  contrast drift requirement provided that the LOWFS can sufficiently reduce the wavefront drift. To verify that the LOWFS has enough bandwidth to sense pm wavefront drift, the LOWFS was modeled for the baseline configuration centered on a 6<sup>th</sup> magnitude star. Losses from reflections, the CCD quantum efficiency, read noise and shot noise were included in the model. An integration time of  $\sim 45$  seconds was sufficient to sense contrast

drift of  $10^{-10}$ , indicating that the LOWFS can easily keep up with the wavefront drift. Further analysis will be done to quantify the WFE drift contributions of the other optics and their impact on the dark field speckle drift.

## 6.11 Spacecraft

### System Overview

The Exo-C spacecraft is designed to use significant Kepler heritage to meet the science requirements defined for the mission. With few exceptions, including structure, high-gain antenna (HGA), optics, and very reliable components, the spacecraft is designed to be fully redundant with all subsystems necessary to deliver the payload to orbit and support it through primary operations. The spacecraft utilizes a low-profile hexagonal box structure at the base of the coronagraph to minimize the total Flight Segment height and satisfy the fairing envelope constraints defined by intermediate class launch vehicles. The spacecraft meets all fairing volume constraints, as can be seen in Foldout 6-1G.

The spacecraft utilizes a three-axis stabilized architecture, maintaining a fixed solar array pointed toward the Sun. This type of architecture minimizes jitter disturbances and shades the coronagraph telescope, helping to maintain payload thermal equilibrium. A body fixed Ka-band high-gain antenna (HGA) is used for high-rate data transmission with body-mounted X-band low-gain antennas (LGAs) for low-rate data transmission and commanding.

#### 6.11.1 Structure

The spacecraft structure's primary requirement is to support the observatory loads during launch and to provide a stable surface to mount the various sensors, avionics, communication and propulsion hardware. To meet these requirements, the hexagonal bus structure, wrapped around the base of the telescope consists of shear panels, a top deck, bottom deck, reaction control system (RCS) deck, and the launch vehicle adapter ring. The shear panels provide structure to accommodate

mounting of the spacecraft electronics, battery, reaction wheels, inertial measurement units (IMUs), radio frequency (RF) equipment, and LGAs. The upper deck serves to provide a rigid closeout for the shear panels, and provides the mounting surface for the solar array panels and HGA. The bottom deck serves as a rigid lower closeout for the shear panels and provides the load path from the shear panels to the launch vehicle adapter ring. The bottom deck also supports the thrusters, associated propellant lines, and launch vehicle umbilical connectors. The RCS deck is attached to the inside of the launch vehicle adapter ring, and provides a mounting surface for the RCS tank, pressure transducer, latch valves, distribution plate, and propellant lines.

To properly isolate the coronagraph from the spacecraft, passive vibration isolators connect the telescope to the upper deck. This system spreads the coronagraph loads into the launch vehicle adapter ring and isolates the instrument from the bus structure. Figure 6.11-1 shows the Exo-C bus structure and solar panels, while Foldout 6-1E depicts the instrument vibration isolation system.

### 6.11.2 Propulsion

The Earth-trailing orbit selected for the Exo-C mission requires no significant maneuver to achieve or maintain orbit. As a result, the only driving propulsion requirement is to provide the observatory with attitude control functionality including: (1) Nulling residual tip-off and spin rates of the flight segment (FS) after separation from the launch vehicle (LV), (2) RWA desaturation, and (3) Attitude control in emergency mode.

To meet these requirements, Exo-C employs a blow-down mono-propellant reaction control system (RCS), shown in Figure 6.11-2. The hydrazine ( $N_2H_4$ ) propellant is stored in a readily available, flight-qualified 13" diameter diaphragm titanium tank. The diaphragm is used to separate the propellant from the pressurant in the tank. The propulsion system also includes

two fill-drain service valves, system filter, pressure transducer, two latch valves, lines, fuel, pressurant (gaseous nitrogen (GN<sub>2</sub>)) and the eight thrusters separated into two redundant thruster branches. The two thruster branches, each containing four thrusters, are mounted on the +Y and -Y axes of the spacecraft bus and isolated by latch valves.

### 6.11.3 Attitude Control

The attitude determination and control system (ADCS) is required to meet the following determination and control functions: (1) stabilize attitude after launch vehicle separation, (2) point the telescope to the science attitude, (3) hold science pointing by using a fine guidance signal provided by the instrument, (4) point solar array to Sun and point HGA to Earth when required, (5) protect coronagraph from imaging Sun, (6) perform roll maneuvers when commanded, and (7) provide attitude control during safe and emergency modes. This section will be used to define the spacecraft ADCS capability that will provide coarse pointing needed for the system. Fine pointing and control is discussed in more detail in §6.7

The ADCS subsystem consists of a combination of attitude determination sensors and active control systems. For attitude determination, fourteen coarse Sun sensors

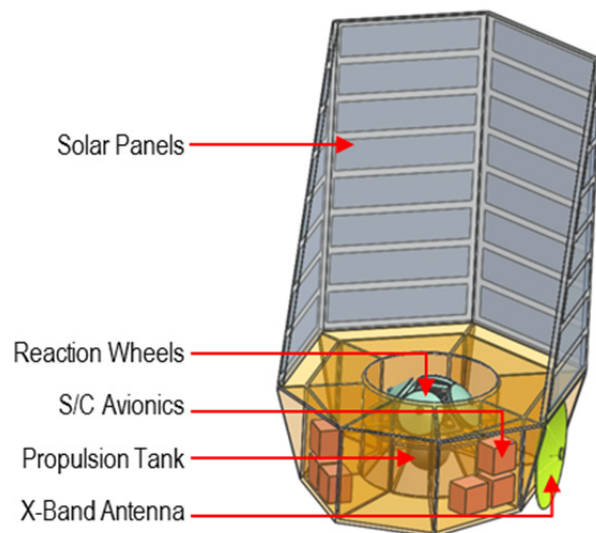


Figure 6.11-1. Exo-C bus and solar array structure.

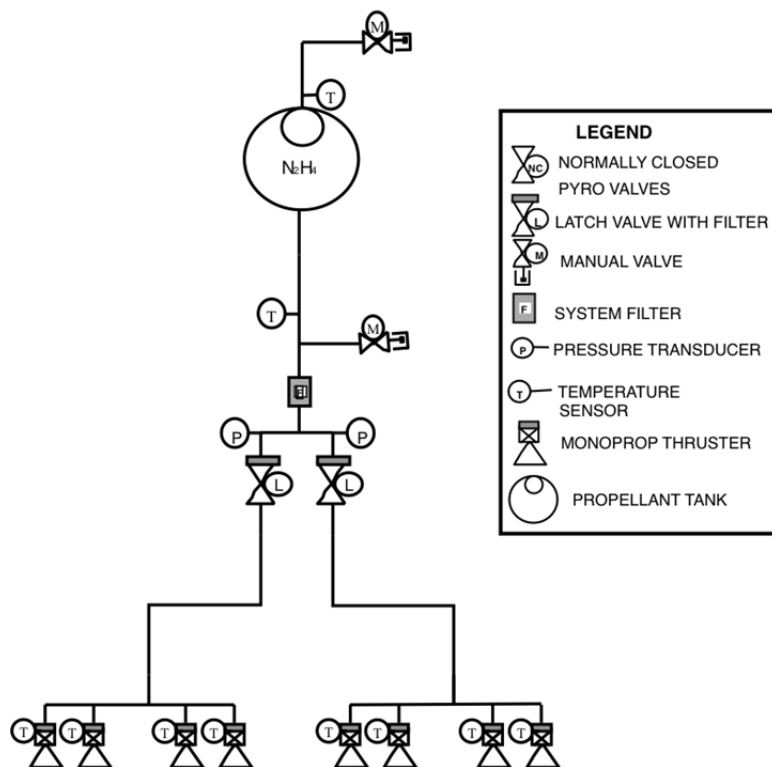


Figure 6.11-2. Exo-C Propulsion Block Diagram.

(CSS) are mounted on the flight structure allowing for coarse pointing by locating the Sun at all times. Redundant star trackers provide the spacecraft with inertial attitude data, while redundant IMUs provide angular rates.

Spacecraft control is provided by a reaction wheel assembly (RWA) consisting of four wheels mounted on non-orthogonal axes. They are active redundant, meaning that all four are normally used, and share the momentum load while remaining single fault tolerant to a wheel failure. Reaction wheels will provide coarse pointing during science observations, solar array and communication pointing, and slew maneuvering during nearly the entire mission except during the initial tipoff from the LV. In addition to the RWA, the ADCS commands the RCS thrusters for attitude control when the reaction wheels are unavailable (such as during launch and early operations and Emergency mode). The RCS thrusters will also be used to desaturate the reaction wheels' solar-pressure-accumulated angular momentum.

#### 6.11.4 Electrical Power

The electrical power distribution system (EPDS) is responsible for providing the spacecraft and instrument with sufficient power throughout the lifetime of the mission. In particular, the EPDS will be required to: (1) provide sufficient power throughout the course of the mission, (2) provide a consistent, stable voltage throughout the mission, and (3) manage and distribute the power to the required subsystems and instrumentation. The EPDS meets these requirements via two methods, solar array and battery, for generation and distribution electronics for power management (see Figure 6.11-3).

Exo-C uses a single fixed solar array of photo-voltaic cells. The EPDS architecture uses a direct energy transfer system that operates by switching on the solar array strings as required to supply power, while regulating the supply voltage within the normal operating range of 24–35 VDC. Strings are arranged into blocking diode-protected subsegments further arranged into segments, resulting in extensive string loss tolerance. The solar array meets the power requirements with one string failure, and is expected to generate approximately 1000 W at the end of the mission, depending on the season.

A 20 A-hr (15 A-hr end of mission energy storage) Li-Ion battery provides launch load support, voltage stability during the mission, and energy reserve if needed for contingency operations.

The bus control assembly (BCA) electronics provides the distribution current-monitor shunts, and fault-isolation fuses capability for the mission. The single point ground is formed by connecting power bus returns to battery returns, solar array returns, and structure.

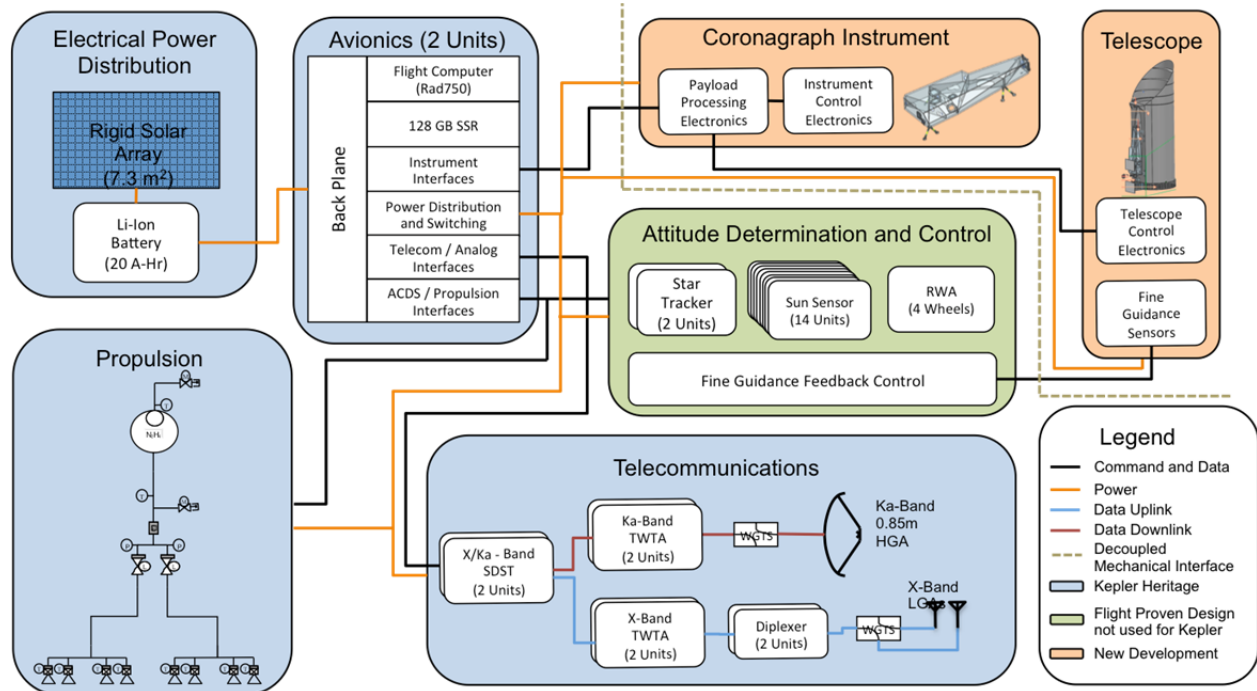


Figure 6.11-3. Exo-C draws significant heritage from the Kepler flight system.

### 6.11.5 Avionics

The avionics subsystem is required to: (1) command and control of the flight system, (2) store and playback of engineering and science data, (3) encode all telemetry for downlink, and (4) time-tag the science data. The Exo-C control box (ECB) utilizes a similar architecture used for the Kepler mission. At the heart of the system lies the RAD750 flight computer, which processes the spacecraft commands and science data for downlink. Command and telemetry, solid-state recorder, attitude determination, and instrument interface boards are located within the ECB and provide the necessary interfaces and drivers for spacecraft operations. A SSR provides the necessary data storage for science data prior to downlink.

### 6.11.6 Communications

The telecom subsystem will be required to: (1) receive commands from the science operations team, (2) transmit engineering and navigation data back to Earth, and (3) provide 4Mbps data rate communication link to a 34-m Deep Space

Network (DSN) station for science data. The telecom subsystem meets these two requirements through a combination of communication frequencies, radios, and antennas.

Exo-C's communication strategy employs a similar architecture as that used by Kepler. Consisting of Ka-band high gain antenna, (HGA), two transmit/receive X-band only LGA pairs, two small deep space transponder radios (SDSTs) capable of operating in the X and Ka-bands, two Ka-band and two X-band traveling wave tube amplifiers (TWTAs), the subsystem is fully capable of meeting the data requirements of the mission. A telecom subsystem block diagram is shown in Figure 6.11-4.

The two communication frequencies are used for varying operation modes. X-band is used for uplink while both X-band and Ka-band are used for downlink. Engineering data can be downlinked via both X-band or Ka-band, however the higher data rate Ka-band system will be used to meet the science data requirements of the mission. The uplink and downlink data rates are listed in Table 6.11-1.

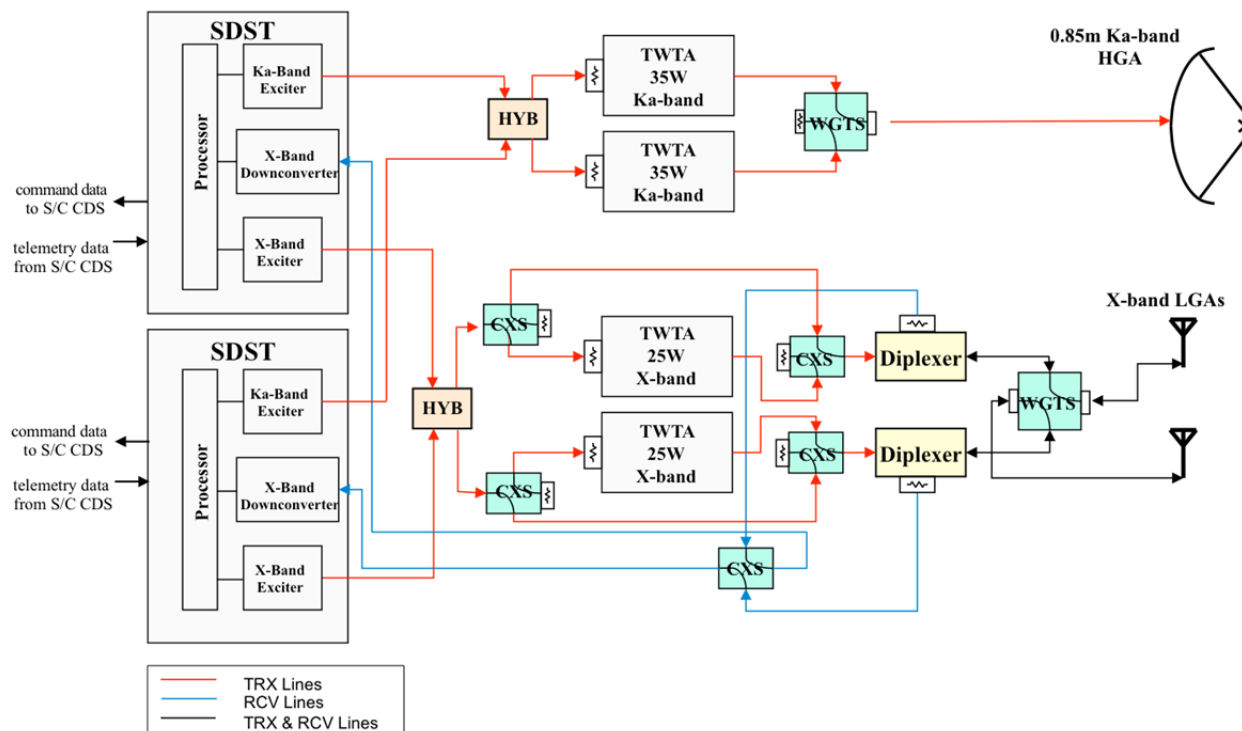


**Figure 6.11-4.** Exo-C telecom subsystem utilizes substantial Kepler heritage to provide sufficient communication data rates throughout the life of the mission.

**Table 6.11-1.** Exo-C's Telecom Subsystem has been designed to meet the required downlink and uplink performance at maximum distances from the Earth.

Parameter	X-band Data Rate (b/s)	Ka-band Data Rate (b/s)
Uplink	2000	N/A
Downlink	16,000	4,331,250

### 6.11.7 Thermal

The thermal control subsystem (TCS) is responsible for: (1) maintaining spacecraft component temperatures within operational limits, and (2) providing temperature sensors for sensing of spacecraft critical temperatures.

All thermal control of the telescope and instrument are provided by the instrument, minimizing mechanical and electrical interfaces to the spacecraft. The instrument thermal design can be found in §6.6.

Heat generated by spacecraft electrical boxes serves to maintain them at flight-allowable temperatures while the bus serves as a radiator of excess heat. Redundant heaters and heater controllers are used to maintain survival temperatures in the event of a failure. Heaters

are usually controlled automatically; FSF compares thermistor data with temperature limits to maintain temperatures by powering the heaters on and off. If necessary, heater setpoint tables can be changed by flight team command.

### 6.12 Ground Subsystem

The Exo-C Mission Ground Segment (GS) is responsible for the execution of Exo-C to ensure the accomplishment of the Level 1 Requirements/Mission Success Criteria. The GS is the final destination of the mission data products. It consists of the people, policies, procedures, facilities, hardware, and software required to successfully complete Exo-C.

As the project prepares for launch and begins the transition from a development organization to an operations organization, more and more emphasis is placed on the development of team procedures and interfaces and validation of the project's capabilities through ground segment integration tests, mission scenario tests, and ultimately operational readiness tests.

Figure 6.12-1 shows the project organization during operations, where the project no longer includes a mission design element and the mission operations system is divided into separate function-based elements.

The Mission Director heads the Mission Management Office (MMO) and reports to the Project Manager. The Project Management Office is administratively responsible to NASA Headquarters to assure that financial, schedule, and staffing resources are properly applied. The MMO will also manage the Flight Planning Center and the Science Operations Center elements as well as performing project system engineering during flight.

The Science Operations Center (SOC) runs the science processing pipeline, manages the database of science targets, provides target data to the MOC when configuration changes are required, analyzes data from each contact to determine if there are any issues and is responsible for monitoring the payload. Planning of science activities is the

responsibility of the Science Office (SO).

The Flight Planning Center (FPC) is responsible for performing spacecraft analysis and flight system anomaly resolution. In addition, the FPC is responsible for overseeing activity planning and command product generation. The FPC also includes the engineering support to manage the flight system including analyzing telemetry, trending subsystem performance and generating any activity requests required to maintain the flight system. The FPC maintains and operates the system test bed (STB), which is used to validate all new command products before they are sent to the FS.

The Mission Operations Center (MOC) will perform the day-to-day operations of the Flight Segment to acquire science and spacecraft data as well as monitor health and safety status. The MOC is responsible for the real-time mission control functions. The MOC also commands data recorder playbacks to downlink science data, accounts for (and replays if required)

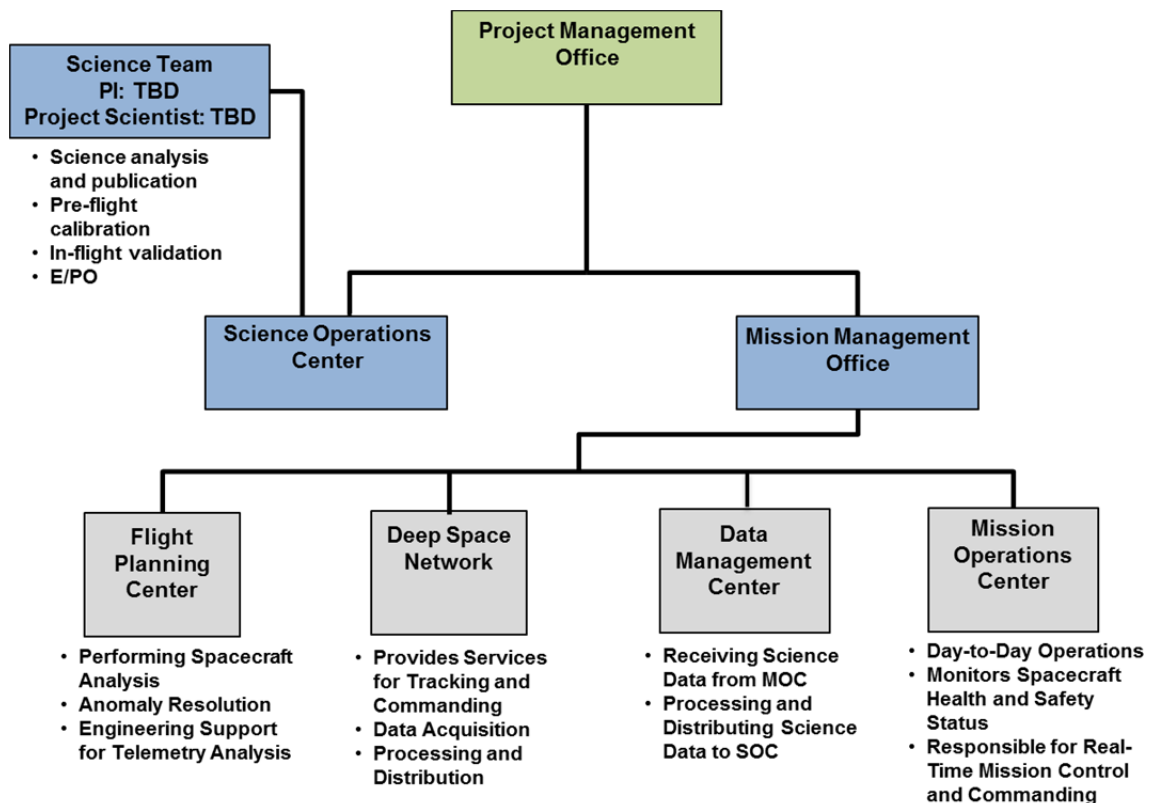


Figure 6.12-1. Exo-C utilizes a simple straightforward distribution of management during Phase E operations.

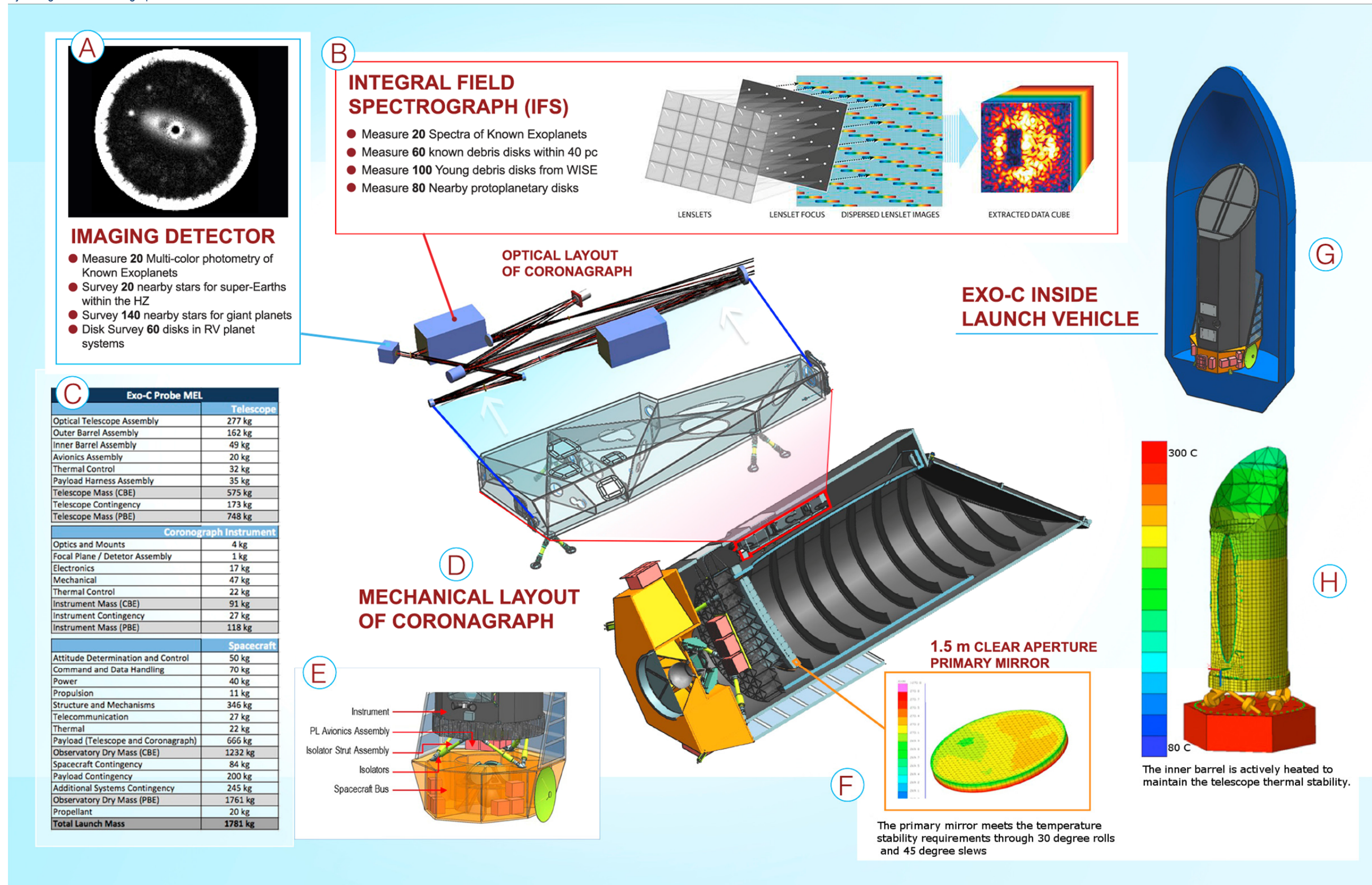
science data, and archives engineering data for performance trending. The MOC performs the activity planning function.

The Data Management Center (DMC) is responsible during operations for receiving science data from the Mission Operations Center and routing processed (decompressed,

partially calibrated) science data to the SOC as well as archiving of science data.

The DSN provides services for tracking and commanding of the spacecraft, data acquisition from the spacecraft, processing and distribution. The Project Scheduling Service (PSS) will interact with the Exo-C project to schedule, allocate, and prioritize DSN resources.

Foldout 6-1. Project organization during operations.



## 7 Mission Operations and Data Analysis

### 7.1 Mission Operations

Exo-C operations fall into the following categories: spacecraft management, target acquisition, instrument optimization and management, and science observations. The Exo-C baseline design, described in §6, along with the science objectives described in §4, allows us to derive durations and repeat rates for these activities. Operations flow and mission time estimates will be based on these durations. The durations and repeat times are summarized in Table 7.1-1.

Based on our preliminary analysis, we show Exo-C can accommodate all of the mission operations and science observations. More detail is given in following subsections.

#### 7.1.1 Spacecraft Management

These activities include communications with the spacecraft, orbit and attitude management, and general housekeeping. Since Exo-C is in an Earth-trailing orbit no time needs to be spent on orbit management or maintenance maneuvers. Due to the high number of targets to be observed, the Exo-C's observing schedule will be constructed in such a way that Earth and Moon avoidance maneuvers will not be necessary, as their positions in relation to the spacecraft will always be known.

Communications with the spacecraft are conducted via two low-gain X-band antennas and a body-fixed Kepler-like Ka-band high-gain antenna. Key characteristics and resulting telecom pass times are shown in Table 7.1-1.

The reaction wheels have been chosen to allow greater than 100 hours of uninterrupted observing times between momentum management events to accommodate spectroscopy observations.

At this point, no specific time has been allocated for anomaly investigations. The assumption is that the routine occurrences are reflected in average duration estimates in the

operations database, while more extreme cases should be handled as risks.

#### 7.1.2 Target Acquisition

The target acquisition time is dominated by how long it will take the instrument to come to its required thermal stability after the Sun angle has been changed. This will depend greatly on the magnitude of the maneuver, illumination change, and thermal design. Preliminary estimates indicate that after two hours the instrument should be sufficiently stable to initiate instrument optimization and maintenance operations. Details of the payload's thermal performance are covered in §6.6.

#### 7.1.3 Instrument Optimization and Maintenance

The coronagraph uses four images to tune the deformable mirrors (DM) to obtain the required contrast. The integration time to obtain the images depends on the apparent magnitude of the star and will vary from target to target. Based on the current target list we have calculated the average time needed to reach  $1e^{-9}$  contrast to be 6 hours. For disk imaging we have assumed a shorter 4 hours for DM tuning, since the contrast does not to be as high.

#### 7.1.4 Science Observations

Science observations are governed by science objectives and fall into three main categories: Spectroscopy of Known Exoplanets, Planet Discovery Surveys, and Disk Imaging Surveys. The durations of each observation will depend on the target characteristics and instrument design. For the Final Report, detailed simulations based on the target list will be performed to evaluate the required durations, but at this point they have been assumed, as shown Table 7.1-1.

**Table 7.1-1.** Mission operations database.

Activity		Duration (hrs)	Repeat Duration (hrs)	Description
<b>Spacecraft Management</b>				
<b>Communications</b>				
C4	Low data rate spacecraft command and telemetry	0		Two LGAs on each face. X-band, 16 kB/sec. No power limitation, but maneuvers may be required. Need to investigate further. For now assume this does not take time away.
C3	High data rate scientific data downlink maneuver	4	168	The current estimate for downlink science is 54 Gbits per week. The body-fixed, Kepler-like, 0.85-m antenna would support 4 Mbits/sec transmissions. In this configuration, there would be one science downlink per week, lasting approximately 4 hours. This is an acceptable configuration.
C2	Set up a link for telecon pass	1	168	A half hour at the frontend and a half hour at backend is required to set up the telecon.
C1	Maneuver spacecraft into place	1	168	Requires 0.5 hr at the front end and 0.5 hr at the back end. The 0.5 hr on back end may not be necessary, as it may be part of subsequent retargeting.
<b>Orbit Management</b>				
	Orbit correction maneuver	N/A	N/A	Not needed for Earth-trailing orbit.
MM	Momentum management	0.5	120	The baselined reaction wheel assemblies, similar to the ones used by SMAP, would allow the spacecraft to maintain pointing without desaturation maneuvers for up to 120 hours. This accommodates the up to 100 hr spectroscopy observation.
	Earth/Moon avoidance maneuvers	N/A	N/A	Should be able to pick targets such that these maneuvers are not necessary.
<b>Housekeeping</b>				
	Anomaly investigation			For now, assume this is included in other estimates as overhead.
<b>Retargeting</b>				
RT	Retargeting maneuver	0.2		Typical slew maneuver time.
TA	Settling time; thermal stab A	2		For spectroscopy and imaging of planets.
TB	Settling time; thermal stab B	1		For disk imaging.
<b>Instrument Optimization and Maintenance</b>				
DM1	Instrument optimization (DM speckle)	6		For the brightest 84 targets, all those that are brighter than 7 <sup>th</sup> mag, the average time to tune the dark hole is 6 hours. The shortest time is 0.72 hr for the brightest -0.12 mag star.
DM2	Instrument optimization (DM speckle)	4		For disk imaging.
<b>Science Observations</b>				
I_SP	Spectroscopy	100		Based on simulations using a 1.5-m clear aperture and the baseline coronagraph architecture described in §5 and §6.
I_PD	Planet discovery survey	20		
I_DI	Disk imaging	6		

### 7.1.5 Operations Flow

Based on the durations in Operations Database, shown in Table 7.1-1, a candidate operations flow is shown in Table 7.1-2. A two-week duration is shown to accommodate a 100-hour spectroscopy observation, which needs to be fitted in between momentum management events. Our current estimates of the 120 hours between momentum management events are based on fairly conservative assumptions and

should not be viewed as restrictive. Observation times longer than 100 hours should easily be accommodated from the momentum management perspective. This sample observation plan shows we can accommodate all the needed operations within a two-week sequence. The entire mission lifetime would be comprised of such observing sequences stitched together and optimized to maximize the science return.

Table 7.1-2. A two-week subset of operations flow.

Hrs	Day N+8	Hrs	Day N+9	Hrs	Day N+10	Hrs	Day N+11	Hrs	Day N+12	Hrs	Day N+13	Hrs	Day N+14		
1	T0001 Retargeting (RT) and Thermal Stabilization (TA)	25		49		73	T0004 Instrument Optimization (DM)	97	T0005 RT and Thermal Stab (TB)	121		145			
2		26		50		74		98	T0005 Instrument Optimization (DMB)	122		T0007 Instrument Optimization (DMA)		146	
3		27		51		75		99		123				147	
4	T0001 Instrument Optimization (DMA)	28		52		76		100	T0005 Disk Imaging (I_DI)	124	T0007 I_PD		148	T0008 RT and Thermal Stab (TB)	
5		29		T0002 RT and Thermal Stab (TB)		53		77		101		125	149		
6		30		T0002 Instrument Optimization (DMB)		54		78		102		126	150		
7	31	55	79		103	127	151								
8	32	56	80		104	128	152								
9	T0001 Planet Discovery Observation (I_PD)	33		57	T0003 Planet Discovery Observation (I_PD)	81	T0004 I_PD	105	T0006 RT and Thermal Stab (TB)	129	T0007 Planet Discovery Observation (I_PD)	153	T0008 Instrument Optimization (DMB)		
10		34		58		82		106		130		154			
11		35		59		83		107		131		155			
12	T0001 Planet Discovery Observation (I_PD)	36	T0002 Disk Imaging (I_DI)	60		84		108	T0006 Instrument Optimization (DMB)	132		156	T0008 Disk Imaging (I_DI)		
13		37		61		85		109		133		157			
14		38		62		86		110		134		158			
15	T0001 Planet Discovery Observation (I_PD)	39		63		87		111	T0006 Disk Imaging (I_DI)	135		159			
16		40		T0003 Retargeting (RT) and Thermal Stabilization (TA)		64		88		112		136		160	Unassigned
17		41		T0003 I_PD		65		89		113		137		161	Unassigned
18	T0001 Planet Discovery Observation (I_PD)	42		66		90		114		138		162	Unassigned		
19		43		67		91		115		139		163		Setup Telecom (C1,C2)	
20		44		68		92		116		140		164		C3 Science Download	
21	45	T0003 Instrument Optimization (DM)	69	T0004 Retargeting (RT) and Thermal Stabilization (TA)	93	117	141								
22	46	70	94	118	142	166									
23	T0001 Planet Discovery Observation (I_PD)	47		71	T0004 I_PD	95		119	MM – Momentum Comp	143		167			
24		48		T0003 I_PD		72		96	120	T0007 RT and TA		144		168	End Telecom (C1, C2)

**Table 7.1-2.** A two-week subset of operations flow (continued).

Hrs	Day N+8	Hrs	Day N+9	Hrs	Day N+10	Hrs	Day N+11	Hrs	Day N+12	Hrs	Day N+13	Hrs	Day N+14	
169	T0009 Retargeting (RT) and Thermal Stabilization (TA)	193		217		241	T0012 Spectroscopy Observation (L_SP)	265		289		313	T0012 Spectroscopy Observation (L_SP)	
170		194		218		242		266		290		314		
171	T0009 Instrument Optimization (DMA)	195		219	Unassigned	243		267		291		315		
172		196		220	Unassigned	244		268		292		316		
173		197	T0010 RT and Thermal Stab (TB)	221	MM – Momentum Comp	245		269		293		317		
174		198	T0010 Instrument Optimization (DMB)	222	T0012 Retargeting (RT) and Thermal Stabilization (TA)	246		270		294		318		
175		199		223	247	271		295		319				
176		200		224	248	272		296		320				
177	201	225		249	273	297		321						
178	T0009 Planet Discovery Observation (L_PD)	202	T0010 Disk Imaging (L_DI)	226	T0012 Instrument Optimization (DMA)	250		274		298		322		
179		203		227		251		275		299		323		
180		204		228		252		276		300		324		
181		205		229		253		277		301		325		
182		206		230		254		278		302		326		
183		207		231		255	279	303	327					
184		208	T0011 RT and Thermal Stab (TB)	232	256	280	304	328						
185		209	T0011 Instrument Optimization (DMB)	233	T0012 Spectroscopy Observation (L_SP)	257	281	305	329					
186		210		234		258	282	306	330					
187		211		235		259	283	307	331					
188	212	236		260		284	308	332						
189	213	T0011 Disk Imaging (L_DI)	237	261		285	309	333						
190	214		238	262		286	310	334						
191	215		239	263		287	311	335						
192	216		240	264		288	312	336						
														Setup Telecom (C1,C2)
														C3 Science Download
													End Telecom (C1, C2)	

## 7.2 Science Data Analysis

The Exo-C science data will go through a science-processing pipeline, similar to that of Kepler. This process will produce Level-4 data products. The data will then be distributed and archived.

### 7.2.1 *Science-processing Pipeline*

The science-processing pipeline will take the raw instrument data and telemetry and produce

four levels of data products. These products will be defined by the final report.

### 7.2.2 *Data Distribution and Archiving*

A data distribution center will receive the raw science data and will be responsible for generating and archiving all of the Exo-C science data. The center will produce the high-level science data products, in the form of images and spectra, to the science team.

## 8 Mission Cost Estimation

### 8.1 Cost

In keeping with the Probe Study Charter, the Exo-C concept is estimated at below the \$1B FY15 Charter requirement. This initial design team estimate is built on the NASA standard WBS and is derived from cost estimation models in common use within the aerospace industry and past NASA analogues, and will be independently estimated by Aerospace Corporation using their Cost and Technical Evaluation (CATE) process. The CATE process endeavors to produce a low risk cost estimate and includes cost assessments for technical and programmatic risks; it was used as the cost evaluation method in the ASTRO 2010 Decadal Survey. The Aerospace CATE will constitute the official estimate of the concept's cost. To ensure that there are no discrepancies between the design team estimate and the CATE estimate, two unofficial CATEs will be run before the final official CATE. This will afford the STDT the opportunity to adjust the baseline design should the CATE estimate come in at a higher number than the design team estimate.

The Exo-C Design Team has performed numerous design trades (aperture, orbit, in-house/out-of-house build, etc.) to achieve a design meeting the required cost cap and returning the maximum science possible. Almost every design decision is weighed against cost. The estimate for the baseline design is captured in Appendix A. The estimate is calculated in \$FY15 and includes: all flight mission costs for Phases A–F, launch service costs, reserves, and all technology development costs following the start of Phase A. No contributions were assumed. The mission was assumed to be reliability Class B (per NPR 8705.4). The use of commercial busses was permitted for these studies.

The four largest contributors to the total mission costs are the payload, spacecraft,

launch services, and reserves. Launch services costs were specified by the study guidelines. For the lowest cost intermediate class launch vehicle the cost was set at \$130M, based on launch vehicle cost data collected by the JPL Advanced Projects Design Team. Reserves were calculated at 30% of the total project cost excluding launch services costs. This exceeds the typical NASA proposal requirement of 25% cost reserves.

The payload is composed of a telescope and a coronagraph and its cost was generated from two widely accepted statistical models, both utilizing only objective input parameters. The coronagraph is modeled as an optical instrument using the NASA Instrument Cost Model (NICM), which is based on over 150 completed flight instruments. NICM is the primary NASA instrument cost estimation tool and has been in wide use for over 10 years. The telescope estimate is derived from aperture size and is calculated from *Update to Single-Variable Parametric Cost Models for Space Telescopes* (Stahl et al. 2013). The aperture-based model was chosen over the mass-driven model since—at this point in the design process—there is no uncertainty in the telescope's aperture diameter unlike its mass. The model fit and its supporting data are shown in Figure 8-1 (Stahl et al. 2013). Most, if not all of the data points used in the model are on-axis telescopes, while Exo-C is off-axis. However, the Quikbird telescope (0.6 m, launched in 2001) and the Worldview telescope (0.6 m, launched in 2007) are both off-axis and cost \$11M and \$19M respectively (BATC presentation to STDT 2013), which straddle the model fit and are consistent with the other actual on-axis telescope costs. Additionally, the sub-millimeter 1.5-m off-axis telescope on Planck is well below the model fit (most likely due to its operational frequency). Though limited, what data there is for off-axis telescopes is consistent with this model, so optical architecture is not a significant telescope cost driver. Like NICM, this

telescope model is also based on actual costs of flight hardware—both models represent the as-built costs with all reserves consumed. Since additional reserves are layered on top of these estimates in the total mission cost, they are both conservative in nature.

Exo-C is in many ways similar to the successful Kepler exoplanet mission. They both have focused exoplanet science objectives; their telescope primary mirrors are of similar size; and they have the same orbit, flight system architecture, ground system, and mission duration. Not surprisingly, their spacecraft are also very similar in design. To estimate the Exo-C spacecraft costs, Kepler actual spacecraft costs (as recorded in the NASA Cost Analysis Data Requirement (CADRe) database) were used as a starting point and adjusted for design variations (i.e., more reliable reaction wheels, upgraded inertial reference unit (IRU), larger load supporting panels) using JPL’s Advanced Projects Design Team design tools to capture the costs of the changes.

Science, operations, and ground system development costs are also based on Kepler

actual costs. The Exo-C ground system architecture is identical to Kepler’s; however, no cost credit has been included for reuse of the Kepler ground system. Exo-C data volume is expected to be smaller than Kepler’s, so the use of Kepler operations costs also includes some conservatism in the estimate. Other Work Breakdown Structure (WBS) costs (management, systems engineering and mission assurance) are based on JPL Advanced Projects Design Team models and are consistent with past JPL Discovery and New Frontiers-class missions.

Following this report, Aerospace will deliver their first CATE for comparison to this estimate. After reconciliation to remove differences in assumptions, the costs will be compared WBS item by WBS item. If any significant differences are evident, the portion of the design driving the difference will be clearly identified in the comparison and the STDT and design team will evaluate the science impact of redesigning for lower cost. This process will be repeated again this summer to identify and reconcile disconnects between the CATE and the design team estimates. The

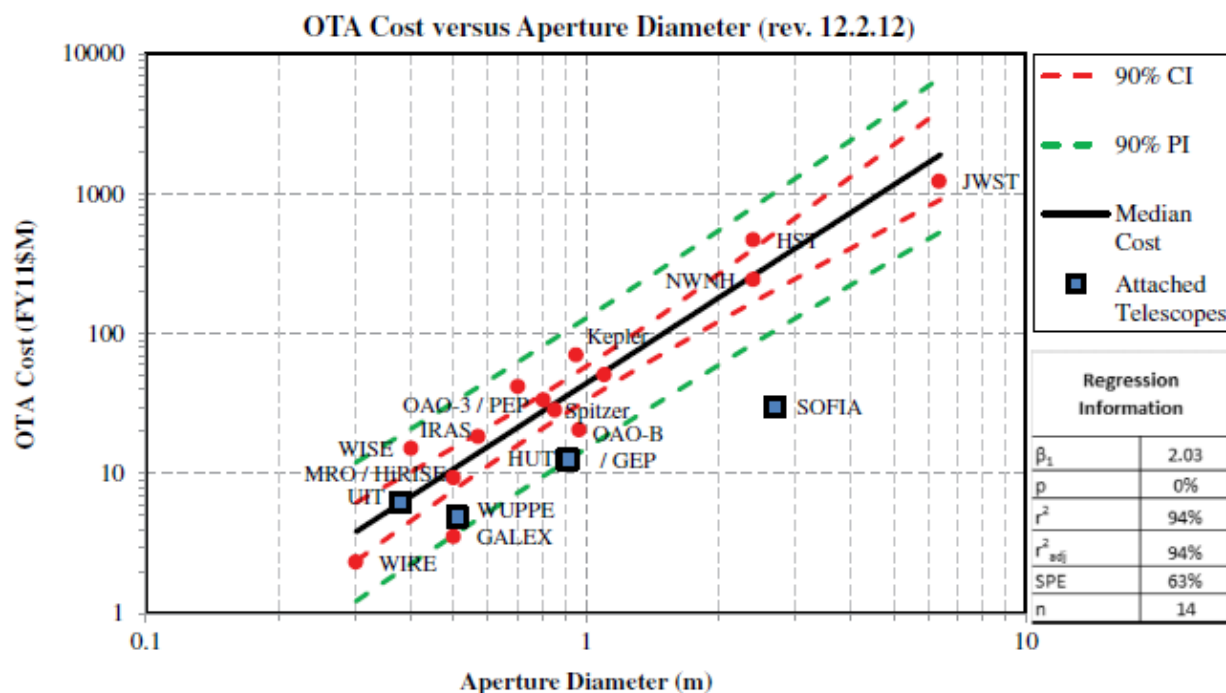


Figure 8-1. Telescope cost as a function of aperture diameter for space-based telescopes (Stahl et al. 2013).

design represented in the final report will include any adjustments needed to address these last issues and will be submitted to Aerospace for the last and official CATE estimate.

## 8.2 Schedule

Exo-C developed a concept schedule based on a Phase A start at the beginning of FY17, project Preliminary Design Review (PDR) in FY19 and a launch no later than December 31, 2024. Technologies requiring development must be at Technology Readiness Level (TRL) 5 by the start of FY17 and TRL 6 at the start of FY19.

The Exo-C schedule is shown in Foldout 8-1. This schedule was developed largely from the Kepler as-built schedule, including all technical delays and programmatically-driven funding delays. The overall schedule is 140 months long and includes 12 months of pre-Phase A development, 92 months of spacecraft and payload development (Phase A through launch), and 36 months of operations. Pre-Phase A technology development work is not included in the \$1B cost cap and is discussed in §9.0. In keeping with the study charter, Phase A begins at the start of FY17. Formulation (Phases A and B) runs for 43 months and includes requirements definition, system and subsystem design, and the start of procurements for long-lead items. It also encompasses the work needed to complete the technology development of the low-order wavefront sensor (LOWFS) and the coronagraph by the start of FY19. The flight system implementation (Phases C and D) takes 50 months and includes the fabrication, integration and test of the flight system. Implementation ends with the launch and initial on-orbit checkout of the flight system in July 2024. The critical path is highlighted in the schedule and runs through the detector procurement, coronagraph development, telescope and payload integration and test, flight system integration and test, and launch. Durations for the telescope, spacecraft bus, payload and flight system integration and test, and ground system development are all based

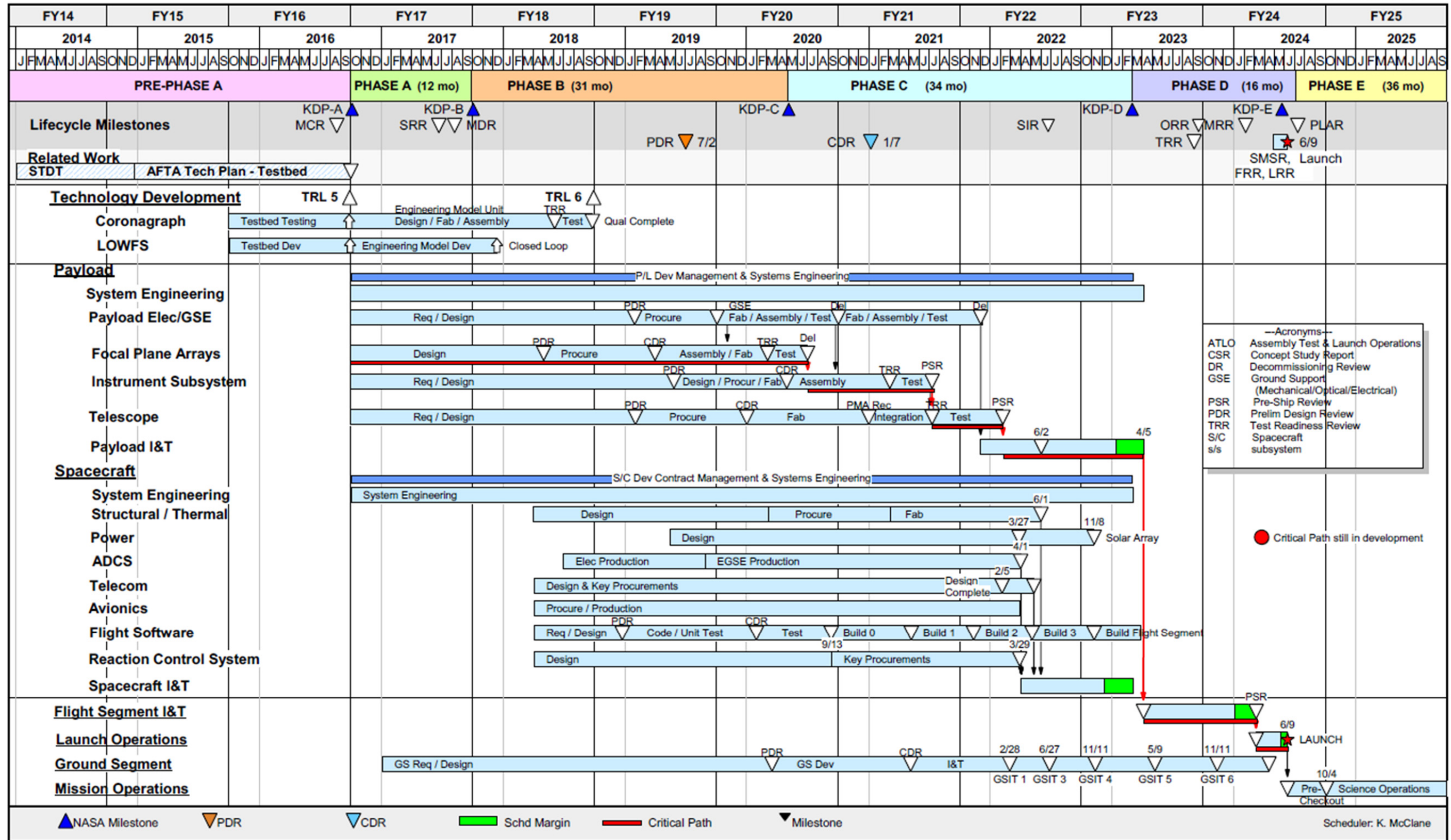
on the actual time required to develop Kepler. The schedule for the coronagraph development was based on expert judgment for JPL instrument systems engineers with experience in developing complex optical observation systems. The schedule shows an overall margin of 6 months, which is in keeping with JPL margin practices for a schedule of this duration.

The Phase A through Phase D duration for Exo-C is 93 months, compared to 91 months for Kepler. At 91 months, Kepler had the longest Phase A–D schedule of any NASA Discovery or New Frontiers mission launched to date. The New Frontiers-class planetary missions are around the \$1B cost cap placed on these studies so they represent comparable scope to the Exo-C mission concept. Of the dedicated telescopes launched by NASA since 2000 (i.e., Wide-field Infrared Survey Explorer (WISE) and Galaxy Evolution Explorer (Galex)) their respective developments took only 87 and 72 months. Only the great observatories, which were significantly larger spacecraft with multiple instruments and served multiple science communities with competing objectives, took longer to develop.

Overall Exo-C has a very conservative development schedule. It is largely based on actual development durations and exceeds the development schedules of all of the most relevant comparable historic missions. Pre-project technology development time is adequate to bring the mission's key technologies up to appropriate TRLs in time to meet the required 2024 launch date. Margins are in keeping with guidelines from a NASA center experienced in developing missions of this scale. Coupled with the previously described conservative cost estimate, this schedule outlines a credible approach to doing the first mission dedicated to direct imaging of exoplanets within the next decade at an affordable cost.

Foldout 8-1. STDT-Coronagraph top schedule (preliminary).

Rev. 1/15/2014



## 9 Technology Needs Assessment

### 9.1 Technology Inheritance

The Exo-C coronagraph instrument is a visible-wavelength camera with a number of critical new features for extremely high contrast imaging—features that are new to space astronomy. Fortunately, a sequence of NASA-sponsored engineering design studies and technology investments over the past decade have identified the critical technologies and brought many of these to an advanced state of readiness. NASA’s Astrophysics Strategic Mission Concept Studies (ASMCS) program, which was completed in 2009, sponsored four relevant coronagraph mission studies: Actively-Corrected Coronagraphs for Exoplanetary System Studies (ACCESS), Pupil mapping Exoplanet Coronagraphic Observer (PECO), Extrasolar Planetary Imaging Coronagraph (EPIC), and DaVinci, which collectively explored the mission design and technology requirements for the five major types of coronagraph architectures: the hybrid Lyot, vector vortex, shaped pupil, pupil mapping phase-induced amplitude apodization (PIAA), and the visible nuller coronagraphs. Over the past five years, NASA’s Strategic Astrophysics Technology (SAT) Technology Development for Exoplanet Missions (TDEM) program has brought each of these coronagraph technologies to a vacuum testbed at JPL in order to test and improve their contrast performance. Over the next few years, they plan to further demonstrate their performance under a simulated space environment. In addition, Small Business Innovation Research (SBIR), Astrophysics Research and Analysis (APRA) Program, and institutional investments have made important contributions to technology readiness, most notably JPL’s development of the precision deformable mirrors now baselined for the Exo-C mission. As a result, most of the critical technologies have been identified and are already poised to advance to flight readiness.

### 9.2 Critical Coronagraph Technologies

Technology needs for high-contrast space coronagraphy can be organized into the following key areas.

1. Coronagraph for starlight suppression.
2. Theoretical designs and Astrophysics Focused Telescope Asset (AFTA) coronagraph technology selections.
3. Laboratory demonstrations and performance model validation.
4. High-order wavefront control for the creation of high contrast dark field images.
5. Maturity and performance of the deformable mirror technology. Wavefront sensing and control algorithms based on deformable mirror (DM) probes and wavefront sensing at the science imager.
6. High order wavefront sensing and control in the presence of pointing jitter.
7. Low-order wavefront sensing and correction of telescope jitter and thermal drift. Requires high fidelity dynamic and thermal models for the telescope.
8. Spectrograph for characterization of exoplanet atmospheres. Optical design for high throughput, low pixel-to-pixel cross talk, large field of view. Large low read-noise image sensors for R = 70 integral field spectroscopy.

### 9.3 Technology Needs In Common with AFTA

While the Exo-C technologies are all based on laboratory tested technologies, three areas have been identified where further development is needed to raise the technology from technology readiness level (TRL) 4 to TRL 5 by the end of Phase A. We note that some of these technology development needs are shared with the AFTA coronagraph program. Therefore, the Exo-C technology development program expects to benefit from technology plans already in place for the AFTA program.

### 9.3.1 Low-order Wavefront Sensor

The low-order wavefront sensor (LOWFS) is the critical component for wavefront maintenance during the science measurements. The Zernike Wavefront Sensor (ZWFS) has been chosen for its simplicity, excellent mechanical stability and theoretically ideal performance. Here the challenge will be testing the LOWFS in JPL's High-Contrast Imaging Testbed (HCIT) to verify it has the necessary subnanometer resolution and stability in a flight-like environment.

The proposed LOWFS is based upon the static, Zernike phase-contrast sensor. This sensor will be used to sense low-order optical aberrations in a system (i.e., tip/tilt, focus). The fundamental operation of the sensor is to introduce a phase shift in the core of a point-spread function ( $1-2 \lambda/D$ ) at the focal plane conjugate to and/or coincident with the coronagraph focal plane. In the subsequent pupil plane, phase variations in the input pupil are imaged as intensity variations. This method is simple yet sensitive. The challenge will be in devising methods to implement it with a focal-plane coronagraph (hybrid Lyot, vector vortex, or PIAA).

The current TRL is 3 primarily based upon the work performed by Mamadou N'diaye, K. Dohlen, T. Fusco, and B. Paul, as reported in *Astronomy & Astrophysics*, June 3, 2013. In that work, they performed analytical and laboratory studies to validate the analytical predictions of the Zernike phase-contrast optical element. At JPL, we have also fabricated a static Zernike phase-plate, but have not quantified its performance to the same level as the group mentioned above.

To mature this technology further, we need to explore how to tightly integrate the phase-contrast optical element with the coronagraph focal-plane-mask optical element. We need to perform analysis to quantify the sensitivity of this method, based upon realistic assumptions about the optical system and the wavefront sensing detector and pupil sampling. Once the

analysis and engineering is refined, we would then proceed to a brassboard demonstration of this system.

#### **LOWFS Technology Development**

##### **Milestones:**

1. Refine requirements for LOWFS.
2. Establish baseline assumptions of system parameters.
3. Engineering analysis to determine architecture and interactions of coronagraph and low-order sensor.
4. Performance analysis of LOWFS to determine fundamental operation.
5. Specification and fabrication of brassboard LOWFS/coronagraph focal plane mask.
6. Brassboard demonstration of LOWFS and coronagraph in open-loop operation consistent with error budget.
7. Brassboard demonstration of closed-loop control with LOWFS as sensor in representative disturbances and within a representative control scheme.

### 9.3.2 Integral Field Spectrograph

Spectroscopic characterization of exoplanet atmospheres is one of the primary science goals of the mission and the integral field spectrograph (IFS) has been chosen as the most promising technology for efficient capture of the spectra. The IFS is a proven technology utilized widely on large ground-based telescopes, but the IFS has yet to be demonstrated in a flight environment.

The Exo-C mission places science requirements that specify imaging and spectroscopic capabilities. In addition to imaging and spectroscopy, the instrument must be able to maintain high contrast between each of the spectra. The instrument will be used for (1) focal plane wavefront sensing, (2) starlight suppression in post processing, and (3) spectral characterization of the science targets (e.g., exoplanets and circumstellar disks). IFSs deployed on ground-based observatories are now capable of taking thousands of spectra

simultaneously, and by the end of the decade the James Webb Space Telescope will fly two IFSs on the Near InfraRed Spectrograph (NIRSpec) and the Mid InfraRed Instrument (MIRI).

Lenslet-based IFSs are very similar to conventional slit-based spectroscopy; however, the slit is replaced by a lenslet array that is used to separate the spatial locations in a focal plane. Each lenslet compresses the light incident upon it into a spot one focal length behind the lenslet array, and the entire array creates a grid of spots in the lenslet focal plane. These spots are passed into a conventional set of spectrograph optics that include collimation, dispersion, and focusing onto the science detector. The general concept of a lenslet-based IFS is shown in Figure 6.5-4. The first lenslet-based IFS was a visible-light instrument at the Canada France Hawaii Telescope (Bacon et al. 1995), and later it was proven to also be viable in the infrared with the OH-Suppressing InfraRed Imaging Spectrograph (OSIRIS) IFS at Keck (Larkin et al. 2006). Now, all of the next-generation, ground-based, high-contrast imaging systems include lenslet-based IFSs as their science cameras (e.g., Apache Point Observatory/GIII, Palomar/P1640, Gemini Planet Imager (GPI), Very Large Telescope (VLT)/Spectropolarimetric High-contrast Exoplanet Research (SPHERE), Subaru/Coronagraphic High Angular Resolution Imaging Spectrograph (CHARIS)). The selection of lenslet-based IFSs for all ground-based high contrast instruments was based on a complimentary set of science and instrument requirements that are imposed on Exo-C. The plethora of lenslet-based IFSs on ground observatories justify this instrument concept is at TRL 4.

Although no IFSs have flown in space to date, the only nontraditional optic in a lenslet-based IFS is the lenslet array itself. Lenslet arrays have been used to conduct science at low contrast on ground-based telescopes for the past 18 years. However, lenslet arrays have never been demonstrated to meet the spectral crosstalk

requirements (e.g., preserving intrascene contrasts of  $10^4$ ) for a space-based, high-contrast imaging IFS. Recent designs suppress the starlight to preserve the  $10^4$  contrast, but this technology has not been demonstrated in a laboratory. Therefore, high-contrast lenslet arrays are at TRL 3. High-contrast lenslet arrays must be matured as soon as possible.

#### ***Milestones:***

1. Develop a verified error budget. Develop calibration and operational procedures for a high-contrast IFS.
2. In a testbed demonstration, characterize the performance limits of the high-contrast IFSs. Demonstrate high-contrast (e.g.,  $10^{-9}$ ) at small angular separations (e.g.,  $3 \lambda/D$ ) over a large spectral bandpass (e.g., 20% bandpass).
3. Compare the IFS model predictions with experimental data to validate the model.

It will take roughly  $\sim 1.5$  years to develop the instrument model and build the high-contrast IFS. Then, it will take another  $\sim 1$  year to integrate this instrument with the HCIT at JPL and demonstrate its performance. After the delivery, the instrument could be made available to all users of the HCIT.

### **9.3.3 High-contrast Actively-corrected Coronagraph**

Here is a high-level checklist of the critical Exo-C enabling coronagraph technologies.

***Coronagraph optical masks and/or stops for the suppression of diffracted starlight:*** All candidate coronagraph types have completed TDEM development and performance demonstrations in JPL's HCIT as part of the SAT/TDEM program. Three of these (hybrid Lyot, shaped pupil, and pupil mapping) will advance to TRL 5 under the Exoplanet Exploration Program (ExEP) in the coming two years as part of the WFIRST-AFTA coronagraph technology development.

***Precision DMs for optical wavefront control:*** High-order surface figure control (i.e., 24 cycles across the pupil with a  $48 \times 48$

actuator DM) is used to create the high contrast dark field coronagraphic images. Our baseline DM is manufactured with a fused silica mirror facesheet controlled by an array of electrostrictive actuators, and is a technology that has been used in coronagraph validation testing over the past decade in the vacuum testbed (HCIT) environment at JPL (see Figures 9.3-2 and 9.3-3). Recent three-axis vibe tests have been completed with flight-configured DMs, and further thermal and radiation testing in the next 2 years will bring the DM technology to TRL 6.

***Wavefront sensing and control algorithms:***

Wavefront sensing and control algorithms have been developed for “static” optical systems in the SAT/TDEM program, and now need to be extended to “dynamic” systems that include the predicted effects of telescope pointing jitter and thermal drift in the Exo-C observatory systems. Current methods utilize the science camera and DM settings to “probe” the wavefront and create the high-contrast exoplanet discovery fields. Algorithm development and testbed demonstrations will be guided by high-fidelity dynamic and thermal models for the Exo-C observatory systems.

***Post-processing of raw image data:***

Science mission studies presume that post-processing of raw image data will be employed to suppress background speckle noise. These algorithms leverage the known imaging characteristics of the observatory, and can be developed and demonstrated on the testbed once the observatory dynamic and thermal models have been perfected.

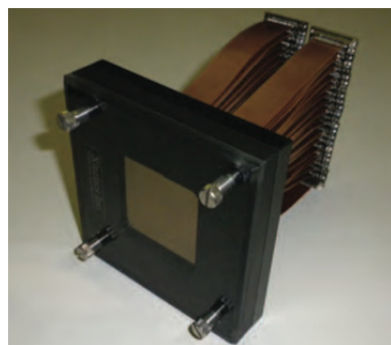


**Figure 9.3-2.**  
Baseline deformable  
mirror technology.

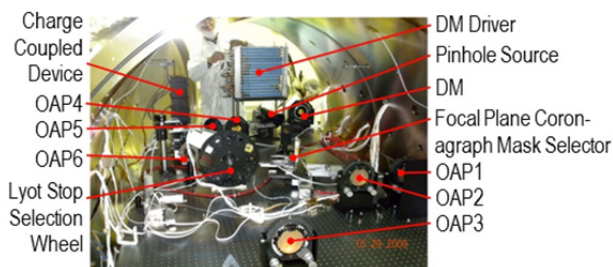


**Figure 9.3-3.** Typical coronagraph layout for the HCIT.

## 9.4 Focused Technology Needs for Exo-C

Critical technology needs that are unique to the Exo-C mission will be identified by the final report.

## 9.5 PIAA and LOWFS Technology and Testbed Demonstrations

### 9.5.1 Introduction

This section describes the status of the starlight suppression system (SSS) technology based on the PIAA option for Exo-C. Most of this work has been carried out at NASA JPL’s HCIT and the Ames Coronagraph Experiment (ACE) testbed at NASA Ames Research Center (ARC), as part of the technology development under the TDEM program, the Explorer program, and internally funded work. Most of this work is directly relevant to the Exo-C PIAA option, and furthermore, the wavefront control and LOWFS demonstrations are relevant to all coronagraph options for Exo-C.

### 9.5.2 Overview of Technology Readiness

The current technology readiness for a PIAA-based SSS is summarized in Table 9.5-1. All the components have been tested in a vacuum environment but not under realistic conditions and are therefore at TRL 5. A simplified version of the SSS has met Exo-C inner working angle (IWA) and raw contrast requirements in vacuum with monochromatic light, and broadband light levels are approaching required levels. However, the existing demonstrations had a slightly different configuration from the one proposed for Exo-C, and have not been tested under realistic thermal and vibrational

environments expected on orbit. Planned technology development efforts for WFIRST-AFTA will demonstrate Exo-C technologies to TRL 6 by 2018, given the similarities between the two missions. Furthermore, proposed PIAA, wavefront control, and LOWFS development for other missions such as EXCEDE would accelerate the schedule.

### 9.5.3 SSS Components, Hardware, and Algorithms

#### 9.5.3.1 Coronagraph Hardware

The PIAA development groups collectively own several sets of Axsys-made PIAA lenses

and three sets of PIAA mirrors: a “first generation” dual set made by Axsys that were tested at JPL, achieving contrasts of  $5 \times 10^{-10}$ ; and a very high quality “second generation” set made by Tinsley (Figure 9.5-1), with which the best of ACE and HCIT results to date were obtained (see first row of Table 9.5-1).

#### 9.5.3.2 DM and Wavefront Control System

The ACE results were obtained with a vacuum-compatible  $32 \times 32$  actuator Boston Micromachines MEMS DM, and HCIT results with a  $32 \times 32$  Xinetics mirror. The Xinetics mirrors were extensively tested in vacuum at HCIT and testing with the BMC mirrors has

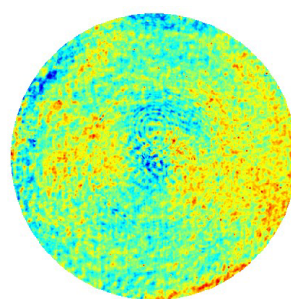


**Figure 9.5-1.** PIAA mirrors manufactured by Tinsley (left) and a surface error map of the second mirror (right) showing an rms surface error of 3.8 nm rms.

**Table 9.5-1.** Components of the SSS, their current and projected technological readiness based on AFTA and other existing technology development efforts. Most components of this table directly impact all coronagraphs and direct imaging missions.

Technology	Current State	Estimated State by 2016–2018
Full SSS	TRL: ~ 4 <ul style="list-style-type: none"> <li>• <math>5e^{-10}</math> contrast between 2.0–4.0 <math>\lambda/D</math> in monochromatic light (HCIT)</li> <li>• <math>1e^{-8}</math> contrast between 2.0–4.0 <math>\lambda/D</math> in 10% broadband light (HCIT)</li> <li>• <math>1.8e^{-7}</math> contrast between 1.2–2.0 <math>\lambda/D</math> (ACE)</li> <li>• Small FOV configuration: DM downstream of PIAA, no inverse PIAA</li> <li>• No FSM, no IFS</li> <li>• Laboratory-controlled illumination and stability conditions</li> </ul>	TRL: 6 <ul style="list-style-type: none"> <li>• Exo-C contrast, working angle, and bandwidth requirements met</li> <li>• Wide FOV configuration: DM upstream of PIAA, inverse PIAA</li> <li>• Fully integrated SSS</li> <li>• Broadband light</li> <li>• Realistic illumination and stability conditions</li> </ul>
BMC DM (alternative option)	TRL:5 <ul style="list-style-type: none"> <li>• Required DM performance proven in air, with DM model validations</li> <li>• Has been operated in vacuum but not tested for required performance</li> </ul>	TRL:6 <ul style="list-style-type: none"> <li>• Required DM performance proven in vacuum with model validations</li> </ul>
Broadband wavefront control	TRL:5 <ul style="list-style-type: none"> <li>• Using data from set of narrowband sub-bands</li> <li>• Not yet with an Exo-C-like configuration</li> </ul>	TRL:6 <ul style="list-style-type: none"> <li>• Uses data from a single broad band</li> <li>• With Exo-C-like configuration</li> </ul>
LOWFS	TRL:5 <ul style="list-style-type: none"> <li>• Fast control demonstrated in air at ACE</li> <li>• Slow control in vacuum at JPL (and at Lockheed Martin)</li> <li>• Not yet tested with realistic disturbances and illumination levels</li> </ul>	TRL:6 <ul style="list-style-type: none"> <li>• Fast control demonstrated in vacuum</li> <li>• Proven to work to spec with realistic disturbances and illumination levels</li> </ul>
Post-processing signal extraction techniques	TRL:5 <ul style="list-style-type: none"> <li>• ADI and CDI, matched filtering have been tried at high contrast in vacuum</li> <li>• Exact benefit under realistic disturbances and illumination levels not characterized</li> </ul>	TRL:6 <ul style="list-style-type: none"> <li>• ADI, CDI, PDI, LOCI, matched filtering, PCA tried in vacuum</li> <li>• Benefit characterized under realistic disturbances and illumination levels</li> </ul>

started in a vacuum chamber at Lockheed Martin (as part of EXCEDE technology development effort) and has shown no arcing problems or performance degradation so far.

Two wavefront control algorithms are in operation at ACE and HCIT: EFC and Speckle Nulling (Belikov et al. 2011). Speckle nulling is a slower algorithm than EFC, but is less sensitive to model errors and is often used as a limiting factor diagnostic tool.

### 9.5.3.3 LOWFS

“Guyon-type” LOWFS systems have been integrated with PIAA coronagraphs at ACE and HCIT. Both are similar except (at the moment) the ACE one has a faster 1100 Hz camera. Both image light reflected by the focal plane mask and a controller uses the image to measure low-order modes (tip/tilt before and after PIAA system, focus, etc.) and computes the appropriate corrections. These corrections are sent to piezo actuators controlling source fiber position (currently in lieu of a fine-steering mirror) and the DM. At ACE, the LOWFS has improved LO errors from  $6 \times 10^{-3} \lambda/D$  to  $2.5 \times 10^{-3} \lambda/D$  and can be further improved. Similar levels have been achieved at HCIT (Figure 9.5-2).

### 9.5.3.4 Modeling, Characterization of Sensitivity, and Error Budgets

PIAA modeling is a mature field as a result of several NASA-funded modeling studies (Krist

et al. 2011). In particular, currently available modeling tools include the following:

- A high accuracy diffraction technique, S-Huygens (Belikov et al. 2006), developed specifically for PIAA to correct Fresnel diffraction approximations that are not accurate enough for high contrast.
- A fast technique based on simple geometric remapping (essentially ray tracing) but with a correction based on the Talbot effect to account for wave propagation, accurate to  $10^{-10}$  contrast for properly designed PIAA systems where diffraction is small.
- End-to-end system modeling capability including wavefront control.

Testbed models are usually run in parallel with laboratory tests to validate our understanding of test data. Any discrepancy is investigated to identify its source. Once identified, the source is either eliminated or incorporated into the models and calibrated. These calibrated models are then used to predict performance, test the importance of suspected limiting factors, help develop wavefront control algorithms and tune optical layouts, and develop realistic error budgets for tolerable levels of wavefront error and misalignment.

A second modeling effort is also planned by the AFTA and EXCEDE programs to characterize expected thermal and mechanical

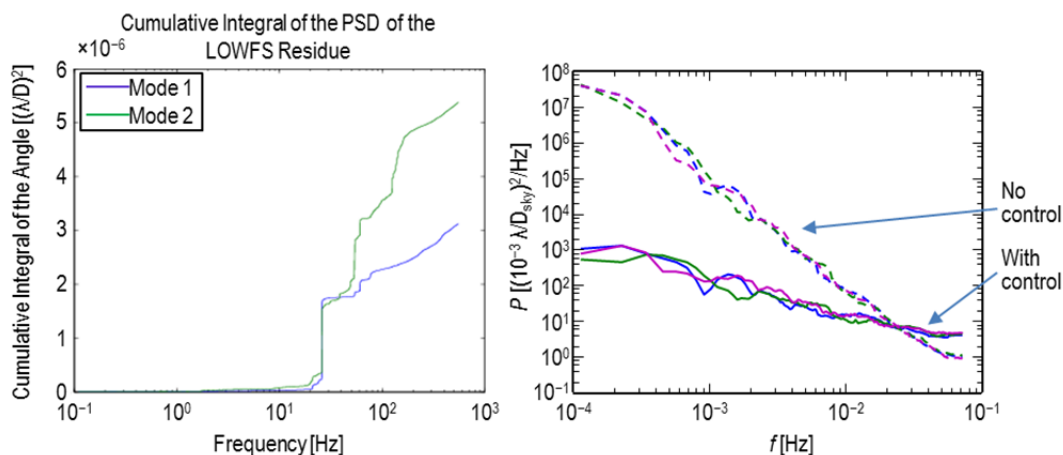


Figure 9.5-2. Left: ACE PIAA LOWFS results. Right: HCIT PIAA LOWFS results.

environmental instabilities on orbit, and replicate similar disturbances in the lab. Existing work at Lockheed Martin in support of the EXCEDE Explorer proposal already resulted in an analysis of the orbital environment and its effect on the stability of the spacecraft. These results will be used in the coming years to estimate the corresponding magnitudes and temporal characteristics of low order error and SSS component misalignments. These errors will then be fed directly into the testbed models to predict the impact on performance, and fed directly into the motorized stages on the testbed to approximately replicate the effects of the orbital environment in the lab.

### 9.5.3.5 Post-processing Speckle Calibration and Subtraction

Several mature speckle subtraction and PSF-fitting techniques exist to suppress speckle noise in post processing by a factor of 10 or more (Marois et al. 2010) and are critical in order to reach the ultimate limits of the instrument. These include difference imaging: spectral (SDI), angular (ADI), polarization (PDI), coherence (CDI); as well as LOCI (locally optimized combination of images), and PCA (principal component analysis). In addition, low

order dynamic errors (such as vibration and decentering) can be measured by the LOWFS and later subtracted in software if they are too fast to be corrected directly. Some of these techniques have been demonstrated in space by members of this team with HST coronagraphy.

As an example, Figure 9.5-3 shows a test demonstrating the extraction of synthetic planet signals below raw contrast in lab data using CDI and matched filtering. CDI in particular is a technique that can be very useful in space but has not seen much use on the ground because it requires static speckles. Such speckles can be calibrated and subtracted even when the DM cannot remove them (e.g., amplitude errors in the  $360^\circ$  field of view). These techniques require no special hardware beyond what exists already for raw contrast demonstrations and we propose to further develop these techniques and characterize their benefit.

### 9.5.4 Testbeds and Results

This section describes the testbeds and results related to PIAA coronagraph, wavefront control, LOWFS, and post-processing work at JPL's HCIT vacuum testbeds at JPL (Kern et al. 2011) as well as ACE testbed (Figure 9.5-4) at NASA ARC (e.g., Belikov et al. 2012). The

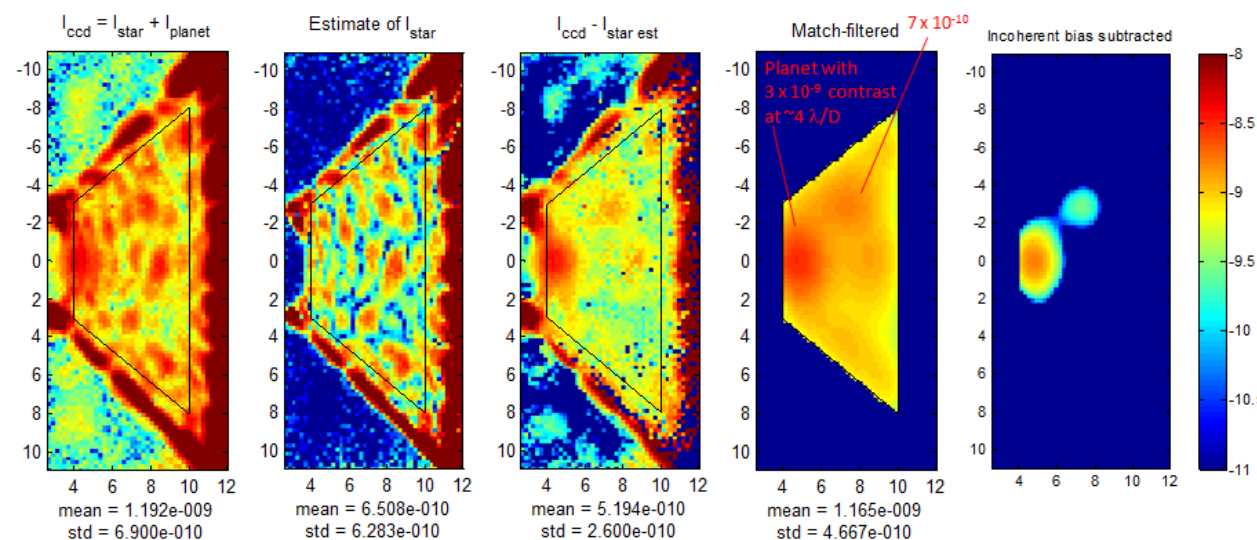


**Figure 9.5-3.** Extraction demonstration of synthetic planet signals below raw contrast in post-processing (at HCIT). Panel 1: raw contrast image; 2: EFC estimate of coherent speckles; 3: CDI image removing coherent speckle; 4: matched filtering; 5: incoherent bias subtraction (zodi, exozodi, and stray instrument light).

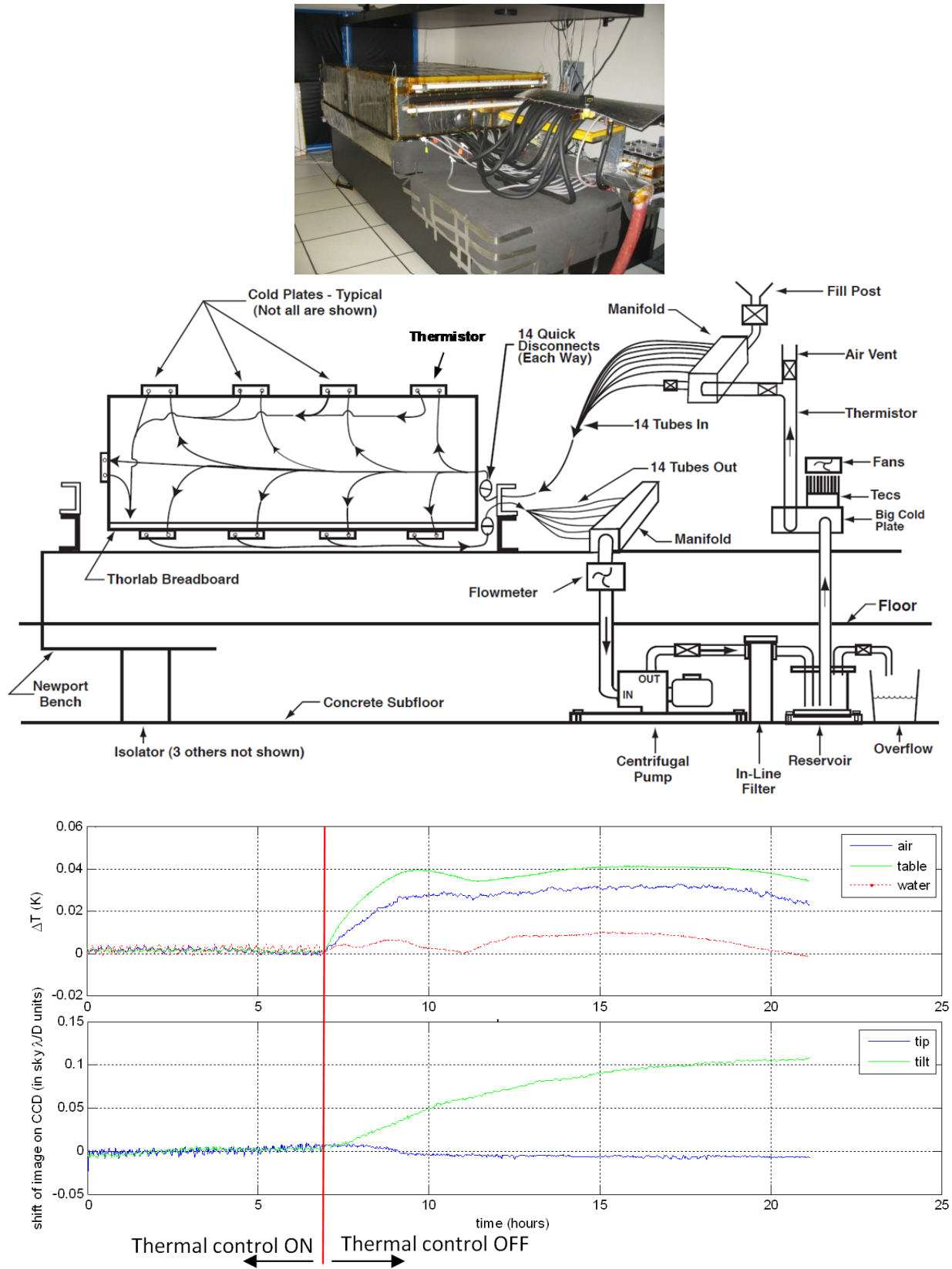


Figure 9.5-4. ACE testbed and its thermal control system.

work at ACE was funded by internal contributions from ARC, Lockheed Martin, and University of Arizona, and also supported in part by HQ, recently through Explorer. The work at HCIT was primarily funded by the SAT/TDEM program. The main thrust of the effort at HCIT is to demonstrate aggressive contrasts at a modest inner working angle of  $2 \lambda/D$  for flagship-class missions potentially capable of exo-Earth detection. The main thrust of the work at ACE is to demonstrate aggressive inner working angles at modest contrast levels for smaller missions such as EXCEDE. Exo-C will benefit from both these testbed demonstrations.

#### 9.5.4.1 Ames Coronagraph Experiment Testbed in Air

The ACE testbed is in temperature-stabilized air, designed for development of coronagraph technologies through TRL 4 and has been defining state of the art performance at IWAs  $< 2 \lambda/D$  (Figure 9.5-5) using the PIAA

architecture. In particular, we have surpassed with substantial margin the EXCEDE contrast requirements in monochromatic light at least in the  $1.2\text{--}2.0$  and  $2.0\text{--}3.4 \lambda/D$  regions separately and have met the “Category III milestone 1” of maintaining  $10^{-6}$  and  $10^{-7}$  contrast in the  $1.2\text{--}2.0$  and  $2.0\text{--}4.0 \lambda/D$  regions simultaneously.

#### 9.5.4.2 High-contrast Imaging Testbed in Vacuum

The layout of the PIAA test at JPL’s HCIT is shown in Figure 9.5-6. Functionally, it is very similar to ACE except that two DMs are used instead of one at ACE. Although the configuration of this layout is slightly different from the one proposed in Exo-C (specifically the DMs are downstream of PIAA and there is no inverse PIAA system), upcoming AFTA technology development includes testing DMs ahead of the PIAA system with the inverse PIAA system.

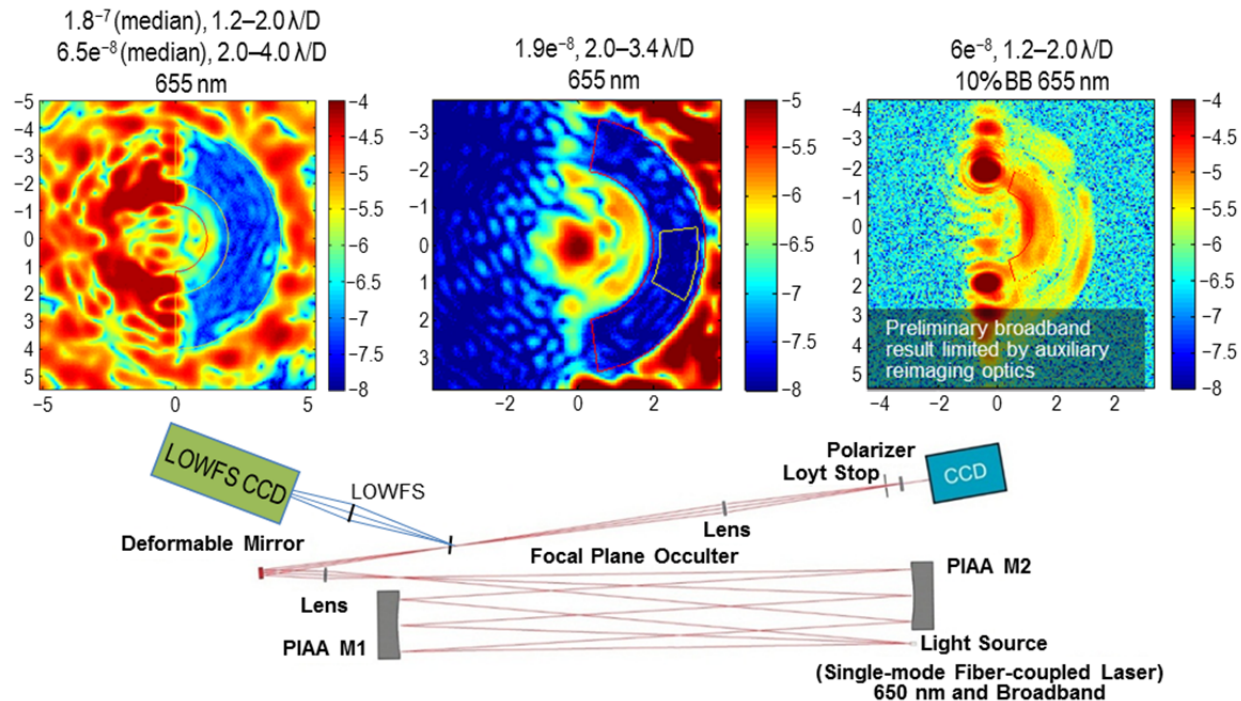


**Figure 9.5-5.** Top: High-contrast demonstrations at the Ames testbed, showing, respectively,  $4.3 \times 10^{-7}$  and  $1.4 \times 10^{-7}$  (median) contrasts in the  $1.2\text{--}2.0 \lambda/D$  and  $2.0\text{--}3.6 \lambda/D$  regions at  $655 \text{ nm}$ ;  $1.9 \times 10^{-8}$  mean contrast between  $2.0$  and  $3.4 \lambda/D$ ; and  $6 \times 10^{-6}$  contrast between  $1.2$  and  $2.0 \lambda/D$  in a  $10\%$ -wide band centered on  $655 \text{ nm}$  (dark zones are shown by red and yellow outlines). Bottom: System architecture used to achieve these results.

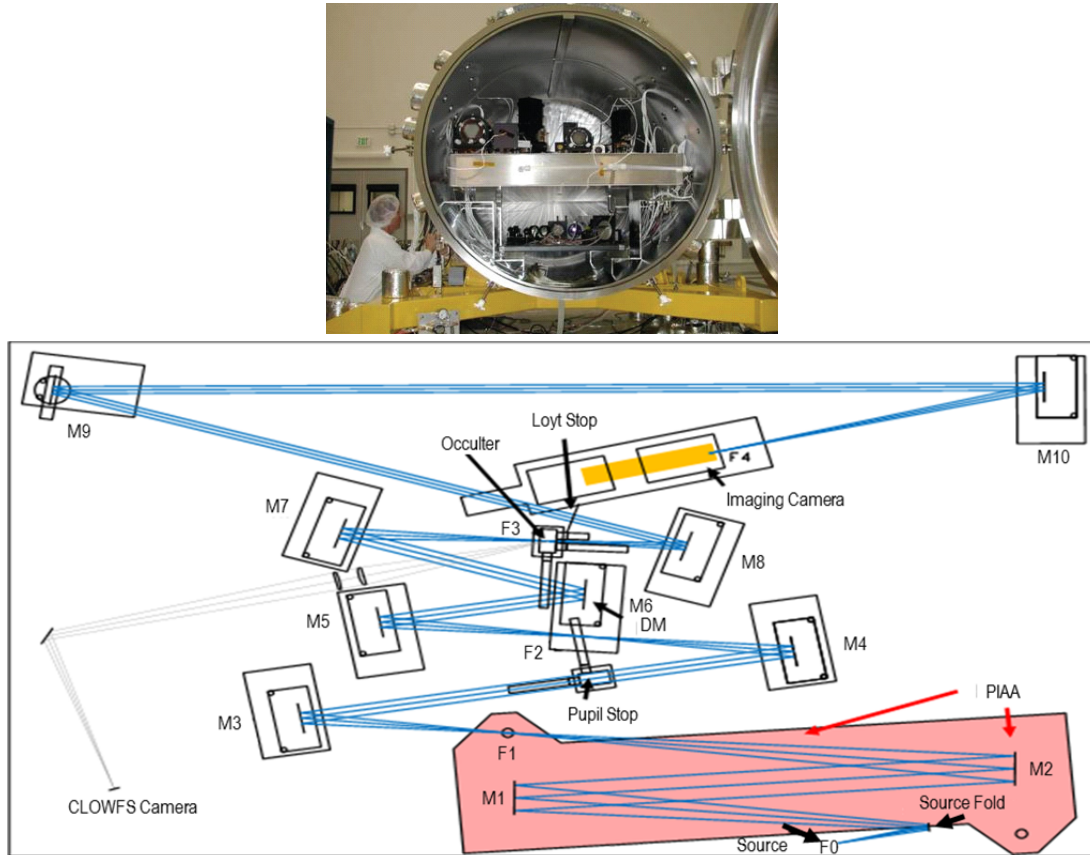


Figure 9.5-6. HCIT tank and PIAA system.

### 9.6 Vortex Probe

In the optical vortex coronagraph (OVC), a spiral phase wrap is applied to the stellar Airy pattern by means of a focal plane phase mask. Recent TDEM work in the HCIT has already allowed the demonstration of monochromatic light suppression below  $10^{-9}$  for the OVC. Specifically, an average suppression of  $5 \times 10^{-10}$  has been obtained for OVC dark holes covering both  $2-7 \lambda/D$  and  $3-8 \lambda/D$  in the HCIT. Figure 9.6-1 shows radially-averaged contrast data from two such dark-hole runs, where the suppression is seen to be below  $10^{-9}$  everywhere but in the innermost  $2-3 \lambda/D$  bin, where it is only slightly higher.

OVC tests with light covering a broader band were also carried out in the HCIT, using a supercontinuum laser source. A dark hole over the region of  $1.5-9.5 \lambda/D$  for the central 2% of a 10% band of light is shown in

Figure 9.6-2. Over the full 10% band, this same dark hole region shows an average suppression of  $9 \times 10^{-9}$ . Thus, the OVC has already demonstrated quite deep contrasts inside the default inner working angle of the probe mission under consideration, which is at  $2 \lambda/D$ .

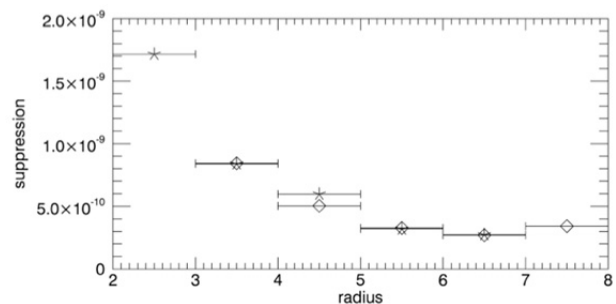
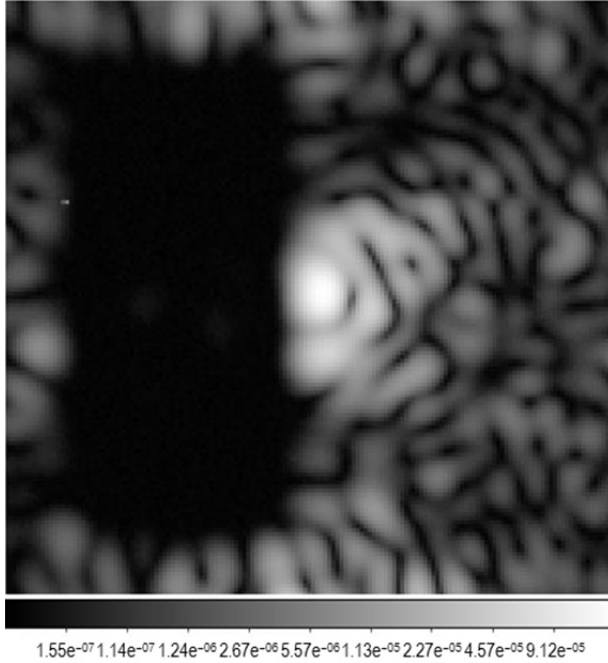


Figure 9.6-1. Radial contrasts for two monochromatic nulling runs that targeted dark holes covering  $3-8 \lambda/D$  (diamonds) and  $2-7 \lambda/D$  (asterisks). Each point gives the average suppression over radial bins  $1 \lambda/D$  wide.



**Figure 9.6-2.** Dark hole covering 1.5–9.5  $\lambda/D$  obtained for one of our broadband nulling runs, for the central 2% band of our overall 10% band, for which suppression was  $9 \times 10^{-9}$  over the full band.

## 10 Plans for the Rest of the STDT Studies

### 10.1 Planned Studies

Design work prior to the interim report began with a broad survey of the mission trade space and concluded with convergence to a baseline mission design configuration that maximizes science yield within the confines of mission cost, risk, and engineering constraints.

Recognizing that the expected science yield will be the most widely read and cited part of the final report, follow-on work will focus on attaining an accurate expected science yield, as well as aspects of the design that most affect the science yield. This primarily includes: (a) a better estimate of telescope thermal and mechanical stability; (b) better jitter specification to verify the need of the two layer isolation system; (c) coronagraph designs that are optimized to take full advantage of the inner working angle; and (d) better mission simulations that generate more accurate science yields based on a given coronagraph design in (c). Beyond this priority, we will perform additional design trades to minimize costs/risks in response to the initial Cost Appraisal and Technical Evaluation (CATE) evaluation should such deficiencies be identified by the CATE team. Any required descope would be followed by more detailed studies to ensure that science and performance requirements will be met, bringing our concept to a high degree of credibility and maturity, and ensuring that the final concept meets the initial study requirement of an end-to-end direct imaging mission producing meaningful advancements in exoplanet science at a CATE-estimated cost below \$1B FY15.

#### 10.1.1 Attitude Control

A detailed pointing control performance study will be carried out to assess pointing performance against requirements. The study will develop a three-axis simulation that includes models of the spacecraft attitude

control system (ACS), jitter sources (reaction wheels), an observatory integrated optomechanical model (flexible body dynamics including isolators and optical sensitivities), and the coronagraph pointing system (fine-guidance camera, fine-steering mechanism, and pointing algorithms).

#### 10.1.2 Thermal Design

Two additional planned trade studies for the thermal subsystem are set-point temperature for the telescope and instrument (traded against testing costs and ability to correct for static gradients), and temperature controller zones and gains, which will be tuned to minimize settling time and wavefront drift. Further design work will involve the simulation of bus-based temperature disturbance sources and the specification of thermal isolation needs and/or levied requirements for bus stability. Time permitting, sensitivity studies will be conducted on the baseline design in an effort to assess performance uncertainty.

#### 10.1.3 Optical Design

The baseline optical design will be updated to incorporate detailed versions of the wavefront sensor and integral field spectrograph. As specific aspects of the selected coronagraph technologies are studied, the optical design will be revised as needed to accommodate their particular implementation requirements. For example, the deformable mirror (DM) and fine-steering mirror (FSM) functions may be severed into discrete units due to the technical immaturity of combined units. However, advancements in devices integrating a DM with a momentum compensated FSM are of interest to Exo-C. If sufficient technical progress is achieved, the optical design will be revised to recapture the benefits of the simplified optical design and increased throughput that a combined unit offers. Similarly, an option to incorporate a higher-density DM device ( $64 \times 64$ ) will be exercised should device developments indicate sufficient

maturity for flight application. Finally, once a satisfactory binary target technique is identified (per §10.1.7), the optical design will be revised as needed to incorporate this high-value function.

#### **10.1.4 Mechanical Design**

Several areas of the telescope mechanical design will be improved over the next few months. The main objective of the planned work is to improve the fidelity of the design. A new optical layout is expected to drive changes in the instrument bench. Once the new optical layout is designed, the instrument bench will be designed in more detail, including determining the layout of the composite panels. The inner barrel, outer barrel, and primary mirror support structure will also be designed in more detail, including light weighting and better definition of interfaces.

#### **10.1.5 Wavefront Sensing**

Four components of the instrument (imaging camera, integral field spectrograph (IFS), low-order wavefront sensor (LOWFS), and FGS) will be used to achieve full wavefront control. More details of the imaging camera and the spectrograph will be modeled to produce requirements for generating the dark field. Also, more details of the FGS and the LOWFS will be modeled to better understand their bandwidth and precision limitations, which may lead to relaxations of the spacecraft line-of-sight and telescope thermal drift requirements. Photon noise and readout noise of individual sensors will set the floor of the measurements; however, noncommon path optics, sensor drift, polarization, and chromaticity (if the selected LOWFS and FGS implementations use light outside of the science band) will also be assessed to determine their impact on wavefront sensing and control.

#### **10.1.6 STOP Modeling**

The structural, thermal, and optical performance (STOP) model integrates Exo-C

thermal, structural, and optical models to predict the time-varying behavior of the dark field. Two scenarios, a 45° pitch and a 30° roll, will be analyzed to bound thermal transients due to spacecraft maneuvers. Thermal model predictions will be used to calculate rigid body motion and figure deformations of the optics. Structural dynamics will be modeled to ascertain their impact on the line-of-sight control loop. The resulting aberrations will be combined with the coronagraph's wavefront sensitivity to estimate the impact on the dark field. The STOP results will be used to produce an error budget, which will include contributions from thermal transients, spacecraft pointing induced beam walk, line-of-sight jitter, as well as control errors from the wavefront sensing and control loop. The impact of the communications roll will also be analyzed to quantify the impact the resultant thermal transient will have on the mission timeline.

#### **10.1.7 Coronagraph**

The designs, models, and analyses will be updated to incorporate the specific features of the down-selected coronagraph approaches. These will be used to identify performance sensitivities, PROPER performance predictions, and influences of mechanical and thermal perturbations. Approaches will be analyzed for achieving performance in the presence of a binary companion star, and assessed for implementation practicality.

### **10.2 Conclusions**

STDT work prior to the interim report focused on a broad survey of the mission trade space and determination of the feasibility of the proposed science goals. STDT work following the interim report will comprise a focused study of the baseline design configuration to ensure that science and performance requirements can be met.

## 11 Conclusion

The Exo-C Science and Technology Definition Team (STDT) was chartered in June 2013 by NASA’s Exoplanet Exploration Program Office to develop a probe-class (not to exceed \$1B) reference mission concept for direct exoplanet imaging and spectral characterization using a visible/NIR space telescope and internal coronagraph instrument. At study completion, in January 2015, the mission concept will be delivered to NASA headquarters for evaluation towards a path to flight at the end of the decade. The Exo-C mission study will also help to guide technology investments in this decade in support of the Astro2010 Decadal Survey goal of having a well-formulated habitable exoplanet imaging mission capable of finding biomarkers by the Astro2020 Decadal Survey.

This interim report documents the work performed by the Exo-C STDT from June 2013 to April 2014, up to the midpoint of the mission study, and culminates in the selection of a baseline mission design that will be refined further in the second half of the mission study. Work prior to the interim report focused on defining science goals, surveying the mission trade space, and modeling efforts to understand telescope stability and instrument performance. Design work after the interim report will focus on more accurate determinations of the expected science yield, another coronagraph design cycle to maximize instrument performance at Exo-C’s inner working angle, and more detailed estimates of telescope and instrument performance and cost.

The science goals outlined by the Exo-C STDT are to: (a) Spectrally characterize at least a dozen RV planets; (b) Search > 100 nearby stars (including alpha Centauri) at multiple epochs for planets down  $\sim 3 \times 10^{-10}$  contrast, characterize mini-Neptunes, and smaller planets if sufficiently close ones exist; (c) Image hundreds of circumstellar disks.

The Exo-C baseline design consists of an unobscured Cassegrain telescope with a 1.5 m primary, in an Earth-trailing orbit, and designed for a 3-year science mission lifetime. It carries a starlight suppression system (SSS) instrument capable of  $10^{-9}$  raw contrast, between 2 and 20  $\lambda/D$ , between 450–1000 nm, and spectral resolution ranging from  $R = 25$  (for < 600 nm) to 70 (for > 600nm), and consists of the following elements (in optical train order): fine-guidance and low-order wavefront sensor (FGS/LOWFS), wavefront control (WFC) system, coronagraph, an integral field spectrometer (IFS), and an imaging camera.

Five architectures were evaluated for the coronagraph: hybrid Lyot, phase-induced amplitude apodization (PIAA), shaped pupil, vector vortex, and the visible nuller. Preliminary evaluations resulted in the selection of the hybrid Lyot as a baseline, with vector vortex and PIAA remaining as options for second design cycle. All of these coronagraphs have demonstrated performance close to what is required by Exo-C and differ primarily in their balance of maturity/risk vs. performance.

The Exo-C mission study serves as a proof-of-concept, demonstrating that a low-risk, cost-driven, probe-class (not to exceed \$1B) mission that leverages mature and proven technologies is capable of ground-breaking exoplanet science that broadly serves the scientific community and responds well to the Astro2010 Decadal Survey, with minimal need for new development, and capable of a first start in this decade. The Exo-C mission study promises to directly image and spectrally characterize planets and disks around more than 100 of the nearest stars. This includes known RV planets, new planets down to Super-Earth size, and potentially Earth twins in the habitable zone if they exist around a few of the most favorable nearest stars. This represents a wide range of science containing characterizations and surveys, essentially making Exo-C an “Exoplanetary Grand Tour” of our immediate galactic neighborhood.

## 12 References and Acronyms

### 12.1 References

- Anglada-Escudé, G., M. Tuomi, et al. “A dynamically-packed planetary system around GJ 667C with three super-Earths in its habitable zone.” *Astronomy & Astrophysics* 556, no. A126 (2013).
- Ardila, D. et al. “A Resolved Debris Disk around the G2V Star HD 107146.” *The Astrophysical Journal* 614, 147 (2004).
- Bacon, R., Y. Copin, G. Monnet, Bryan W. Miller, J. R. Allington-Smith, M. Bureau, C. Marcella Carollo, Roger L. Davies, Eric Emsellem, Harald Kuntschner, Reynier F. Peletier, E. K. Verolme, P. Tim de Zeeuw, et al. “The SAURON project - I. The panoramic integral-field spectrograph.” *Monthly Notices of the Royal Astronomical Society* 326, no.1 (September 2001): 23–35.
- Barnet, C. D., Westphal, J. A., Beebe, R. F., and Huber, L.F. “Hubble Space Telescope observations of the 1990 Equatorial Disturbance on Saturn: Winds and Central Meridian Albedos.” *Icarus* 100 (1992): 499–511.
- Bastien, F.A., et al. “Radial velocity variations of photometrically quiet, chromospherically inactive Kepler stars: A link between RV jitter and photometric flicker.” *The Astronomical Journal* 147, 29 (2014).
- BATC presentation to STDT, “Ball Precision Telescope Heritage and Capabilities,” December 13, 2013.
- Bayard, D. S. “Advances in Precision Pointing Control for NASAs Spitzer Space Telescope.” Proceedings of the 27<sup>th</sup> Annual AAS Rocky Mountain Guidance and Control Conference (2004).
- Bean, Jacob L., Desert, Jean-Michel, Kabath, Petr, Stalder, Brian., Seager, Sara, et al. “The Optical and Near-infrared Transmission Spectrum of the Super-Earth GJ 1214b: Further Evidence for a Metal-rich Atmosphere.” *The Astrophysical Journal* 743, Issue 1, article id. 92 (2011): 12 pp.
- Belikov, R., Pluzhnik, E., Witteborn, F. C., Greene, T. P., Lynch, D. H., Zell, P. T., and Guyon, O. “Laboratory demonstration of high-contrast imaging at inner working angles  $2 \lambda/D$  and better.” *Proc SPIE* 8151 (2011).
- Belikov, R., Give’on, A., Kern, B., Cady, E., Carr, M., Shaklan, S., Balasubramanian, K., White, V., Echternach, P., Dickie, M., Trauger, J., Kuhnert, A., and Kasdin, N. J. “Demonstration of high contrast in 10% broadband light with the shaped pupil coronagraph.” *Proc. SPIE* 6693, 6693-0Y (2007).
- Belikov, R., Kasdin, N. J., and Vanderbei, R. J. “Diffraction-based Sensitivity Analysis of Apodized Pupil-Mapping Systems.” *Astrophysical Journal* 652, Issue 1 (2006): 833–844.
- Belikov, R., Pluzhnik, E., Witteborn, F. C., Greene, T. P., Lynch, D. H., Zell, P. T., Schneider, G., Guyon, O., and Tenerelli, D. “EXCEDE Technology Development I: First demonstrations of high contrast at  $1.2 \lambda/D$  for an Explorer space telescope mission.” *Proc SPIE* 8442-6 (2012).
- Betremiux and Kaltenecker 2013 (in review).
- Borucki, William J., Agol, Eric, Fressin, Francois, Kaltenecker, Lisa, Rowe, Jason, et al. “Kepler-62: A Five-Planet System with Planets of 1.4 and 1.6 Earth Radii in the Habitable Zone.” *Science* 340, Issue 6132 (2013): 587–590.
- Breckinridge, J. B., and B. R. Oppenheimer. “Polarization Effects in Reflecting Coronagraphs for White-Light Applications in Astronomy.” *Astrophysical Journal* 600 (2004): 1091–1098.
- Bryden, G., Beichman, C. A., Trilling, D. E., et al. “Frequency of Debris Disks around Solar-Type Stars: First Results from a Spitzer/MIP Survey.” *The Astrophysical Journal* 636 (2006): 1098–1113.

- Cahoy, K.L., Marley, M.S., and Fortney, J.J. “Exoplanet albedo spectra and colors as a function of planet phase, separation, and metallicity.” *The Astrophysical Journal* 724 (2010): 189–214.
- Casertano, S., Lattanzi, M. G., Sozzetti, A., et al. “Double-blind test program for astrometric planet detection with Gaia.” *Astronomy & Astrophysics* 482, no. 2 (2008): 699–729.
- Charbonneau, David, Berta, Zachory K., Irwin, Jonathan, Burke, Christopher J., Nutzman, Philip, et al. “A super-Earth transiting a nearby low-mass star.” *Nature* 462, Issue 7275 (2009): 891–894.
- Chabrier, G., Baraffe, I., Selsis, F., et al. “Gaseous planets, protostars, and young brown dwarfs.” *Protostars and Planets V* (2007): 623–638.
- Clampin, M. et al. “The Extrasolar Planetary Imaging Coronagraph: Architectures of Extrasolar Systems.” ASMC Study Report (2009). <http://exep.jpl.nasa.gov/files/exep/asmc-clampin.pdf>.
- Deming, D., Seager, S., Winn, J., Miller-Ricci, E., Clampin, M., Lindler, D., and Ennico, K., “Discovery and characterization of super-Earths using an all-sky transit survey and follow-up by the James Webb Space Telescope.” *Publications of the Astronomical Society of the Pacific* 121 no. 883 (2009): 952–967.
- De Pontieu, B., et al. “The Interface Region Imaging Spectrograph (IRIS).” *Astro-ph.* (2014).
- Des Marías D. et al. “Remote Sensing of Planetary Properties and Biosignatures on Extrasolar Terrestrial Planets.” *Astrobiology* 2 (2002): 153–181.
- Eiroa, C., Marshall, J. P., Mora, A., Montesinos, B., Absil, O., Augereau, J. C., Bayo, A., Bryden, G., Danchi, W., del Burgo, C., Ertel, S., Fridlund, M., Heras, A. M., Krivov, A. V., Launhardt, R., Liseau, R., Löhne, T., Maldonado, J., Pilbratt, G. L., Roberge, A., Rodmann, J., Sanz-Forcada, J., Solano, E., Stapelfeldt, K., Thébault, P., Wolf, S., Ardila, D., Arévalo, M., Beichmann, C., Faramaz, V., González-García, B. M., Gutiérrez, R., Lebreton, J., Martínez-Arnáiz, R., Meeus, G., Montes, D., Olofsson, G., Su, K. Y. L., White, G. J., Barrado, D., Fukagawa, M., Grün, E., Kamp, I., Lorente, R., Morbidelli, A., Müller, S., Mutschke, H., Nakagawa, T., Ribas, I., and Walker, H. “DUst around NEarby Stars. The survey observational results.” *Astronomy & Astrophysics* 555, no. A11 (2013).
- Elkins-Tanton, Linda T. and Seager, Sara. “Ranges of Atmospheric Mass and Composition of Super-Earth Exoplanets.” *The Astrophysical Journal* 685, Issue 2 (2008): 1237–1246.
- Give’on, A., Kern, B., Shaklan, S., Moody, D., and Pueyo, L. “Broadband wavefront correction algorithm for high-contrast imaging systems.” *Proc. SPIE* 6691, 66910A (2007).
- Greaves, J. S., Holland, W. S., Wyatt, M. C., Dent, W. R. F., Robson, E. I., Coulson, I. M., Jenness, T., Moriarty-Schieven, G. H., Davis, G. R., Butner, H. M., Gear, W. K., Dominik, C., and Walker, H. J. “Structure in the  $\rho$  Eridani Debris Disk.” *The Astrophysical Journal* 619 (2005): L187–L190.
- Green, Joseph J., and Shaklan, S. B. “Optimizing coronagraph designs to minimize their contrast sensitivity to low-order optical aberrations.” *Proc. SPIE* 5170 (2003): 25–37. doi: 10.1117/12.506485.
- Green, J., et al. “Wide-Field InfraRed Survey Telescope (WFIRST) Final Report,” arXiv 1208.4012 (2012).
- Guyon, O., Martinache, F. “How extremely large telescopes (ELTs) will acquire the first spectra of rocky habitable planets.” *American Astronomical Society Meeting Abstracts* 221, no. 419.05 (2013).
- Guyon, Olivier. “Limits of Adaptive Optics for High-Contrast Imaging.” *The*

- Astrophysical Journal* 629 (2005): 592–614. arXiv:astro-ph/0505086v2.
- Guyon, Olivier, Taro Matsuo, and Roger Angel. “Coronagraphic Low Order Wave front Sensor: Principle and Application to a Phase-Induced Amplitude Coronagraph.” *The Astrophysical Journal* 693 (2009): 75–84. arXiv:0911.1301v1.
- Handy, B. N., L. W. Acton, C. C. Kankelborg, C. J. Wolfson, D. J. Akin, M. E. Bruner, R. Carvalho, R. C. Catura, R. Chevalier, D. W. Duncan, C. G. Edwards, C. N. Feinstein, S. L. Freeland, F. M. Friedlaender, C. H. Hoffmann, N. E. Hurlburt, B. K. Jurcevich, N. L. Katz, G. A. Kelly, J. R. Lemen, M. Levay, R. W. Lindgren, D. P. Mathur, S. B. Meyer, S. J. Morrison, M. D. Morrison, R. W. Nightingale, T. P. Pope, R. A. Rehse, C. J. Schrijver, R. A. Shine, L. Shing, K. T. Strong, T. D. Tarbell, A. M. Title, D. D. Torgerson, L. Golub, J. A. Bookbinder, D. Caldwell, P. N. Cheimets, W. N. Davis, E. E. Deluca, R. A. McMullen, H. P. Warren, D. Amato, R. Fisher, H. Maldonado, and C. Parkinson. “The transition region and coronal explorer.” *Solar Physics* 187, no. 2 (1999): 229–260.
- Hines, D. C., et al. “The Moth: an Unusual Circumstellar Structure Associated with HD 61005.” *The Astrophysical Journal* 671, L165 (2007).
- Hinz, P. “The Hunt for Observable Signatures of Terrestrial Planetary Systems (HOSTS): LBTI’s Zodiacal Dust Survey.” In *American Astronomical Society Meeting Abstracts* 221 (2013): #403.06.
- Howard, Andrew W. “Observed Properties of Extrasolar Planets.” *Science* 340, Issue 6132 (2013): 572–576.
- Howard, Andrew W., Marcy, Geoffrey W., Bryson, Stephen T., Jenkins, Jon M., Rowe, Jason F., et al. *The Astrophysical Journal Supplement* 201, Issue 2, article id 15 (2012): 20 pp.
- Ida, Shigeru and Lin, D. N. C. “Toward a Deterministic Model of Planetary Formation. II. The Formation and Retention of Gas Giant Planets around Stars with a Range of Metallicities.” *The Astrophysical Journal* 616, Issue 1 (2004): 567–572.
- Kalas, P., Graham, J. R., and Clampin, M. “A Planetary System as the Origin of Structure in Fomalhaut’s Dust Belt” *Nature* 435 (2005): 1067–1070.
- Kalas, P., Fitzgerald, M. P., and Graham, J. R., “Discovery of Extreme Asymmetry in the Debris Disk Surrounding HD 15115.” *The Astrophysical Journal* 661, L85 (2007).
- Karkoschka, E. “Spectrophotometry of the Jovian planets and Titan at 300–1000 nm wavelength, The methane spectrum.” *Icarus* 111 (1994) 174–192.
- Kasdin, N. J., Groff, T., Carlotti, A., and Vanderbei, R. “Space-based planet detection using two MEMS DMs and a shaped pupil.” in *Society of Photo-Optical Instrumentation Engineers (SPIE) Conference Series* 8253 (2012).
- Kelsall, T., Weiland, J. L., Franz, B. A., et al. “The COBE Diffuse Infrared Background Experiment Search for the Cosmic Infrared Background. II. Model of the Interplanetary Dust Cloud.” *The Astrophysical Journal* 508 (1998): 44–73.
- Kern, B., Guyon, O., Give’on, A., Kuhnert, A., Niessner, A., Martinache, F., and Balasubramanian, K. “Laboratory demonstration of phase induced amplitude apodization (PIAA) coronagraph with better than  $10^{-9}$  contrast.” *Proc. SPIE* 8864, 8864-26 (2013).
- Kern, B. D., Guyon, O., Give’on, A., Kuhnert, A., and Niessner, A. “Laboratory testing of a Phase-Induced Amplitude Apodization (PIAA) coronagraph.” *Proc. SPIE* 8151, (2011).
- Koch, D., Borucki, W., Dunham, E., Geary, J., Gilliland, R., Jenkins, J., Latham, D., Bachtell, E., Berry, D., Deiningner, W., R.

- Dureng, T. N., Gautier, Gillis, L., Mayer, D., Miller, C., Shafer, D., Sobock, C., Stewart, C., and Weiss, M. “Overview and status of the Kepler Mission.” Proceedings of the SPIE Conference 5487 on Optical, Infrared, and Millimeter Space Telescopes (2004).
- Kreidberg, L., Bean, J. L., Desert, J.-M., Benneke, B., Deming, D., Stevenson, K. B., Seager, S., Berta-Thompson, Z., Seifahrt, A., and Homeier, D. “Clouds in the atmosphere of the super-Earth exoplanet GJ1214b.” *Nature* 505 (2014): 69–72.
- Kreidberg, L., Bean, J. L., Desert, J.-M., Benneke, B., Deming, D., Stevenson, K. B., Seager, S., Berta-Thompson, Z., Seifahrt, A., and Homeier, D. “Clouds in the atmosphere of the super-Earth exoplanet GJ1214b.” *Nature* 505 (2014): 69–72.
- Krist, J. E., Ardila, D. R., Golimowski, D. A., Clampin, M., Ford, H. C., Illingworth, G. D., Hartig, G. F., Bartko, F., Benítez, N., Blakeslee, J. P., Bouwens, R. J., Bradley, L. D., Broadhurst, T. J., Brown, R. A., Burrows, C. J., Cheng, E. S., Cross, N. J. G., Demarco, R., Feldman, P. D., Franx, M., Goto, T., Gronwall, C., Holden, B., Homeier, N., Infante, L., Kimble, R. A., Lesser, M. P., Martel, A. R., Mei, S., Menanteau, F., Meurer, G. R., Miley, G. K., Motta, V., Postman, M., Rosati, P., Sirianni, M., Sparks, W. B., Tran, H. D., Tsvetanov, Z. I., White, R. L., and Zheng, W. “Hubble Space Telescope Advanced Camera for Surveys Coronagraphic Imaging of the AU Microscopii Debris Disk.” *The Astronomical Journal* 129 (2005): 1008–1017.
- Krist, J., Belikov, R., Pueyo, L., Mawet, D., Moody, D., Trauger, J., and Shaklan, S. “Assessing the performance limits of internal coronagraphs through end-to-end modeling.” *Proc. SPIE* 8864, 88640P (2013).
- Krist, J., et al. “TDEM Technology Milestones 1 & 2 Results Reports: Assessing the performance limits of internal coronagraphs through end-to-end modeling.” JPL Documents D-74425 and D-74426 (2012) (available at [exep.jpl.nasa.gov/technology](http://exep.jpl.nasa.gov/technology)).
- Krist, J. E., Stapelfeldt, K. R., Bryden, G., and Plavchan, P. “Hubble Space Telescope Observations of the HD 202628 Debris Disk.” *The Astronomical Journal* 144, 45 (2012).
- Krist, J., Belikov, R., Pueyo, L., Mawet, D., Moody, D., Trauger, J., and Shaklan, S. “Assessing the performance limits of internal coronagraphs through end-to-end modeling: a NASA TDEM study.” *Proc. SPIE* 8151, 81510E (2011).
- Krist, J., Pueyo, L., and Shaklan, S. “Practical numerical propagation of arbitrary wavefronts through PIAA optics.” *Proc. SPIE* 7731, 77314N (2010).
- Krist, J. “PROPER: an optical propagation library for IDL.” *Proc. SPIE* 6675, 66750P (2007).
- Kuchner, M. J., and Holman, M. J. “The Geometry of Resonant Signatures in Debris Disks with Planets.” *The Astrophysical Journal* 588 (2003): 1110–1120.
- Lagrange, A.-M., Bonnefoy, M., Chauvin, G., et al. “A Giant Planet Imaged in the Disk of the Young Star beta Pictoris.” *Science* 329, 57 (2010).
- Larkin, James, Matthew Barczys, Alfred Krabbe, Sean Adkins, Ted Aliado, Paola Amico, George Brims, Randy Campbell, John Canfield, Thomas Gasaway, Allan Honey, Christof Iserlohe, Chris Johnson, Evan Kress, David LaFreniere, Ken Magnone, Nick Magnone, Michael McElwain, Juleen Moon, Andreas Quirrenbach, Gunnar Skulason, Inseok Song, Michael Spencer, Jason Weiss, and Shelley Wright. “OSIRIS: A diffraction limited integral field spectrograph for Keck.” *New Astronomy Reviews* 50, no. 4 (2006): 362–364.

- Lawson, P. R., Belikov, R., Cash, W., Clampin, M., Glassman, T., Kasdin, N. J., Kern, B. D., Lyon, R., Mawet, D., Moody, D., Samuele, R., Serabyn, E., Sirbu, D., and Trauger, J. “Survey of experimental results in high-contrast imaging for future exoplanet missions.” *Proc. SPIE* 8864, 8864-1F (2013).
- Lawson, P. R. “Exoplanet Exploration Program Technology Plan, Appendix: 2012.” JPL Document D-77698 (2013). [http://exep.jpl.nasa.gov/files/exep/2012Appendix\\_Fall.pdf](http://exep.jpl.nasa.gov/files/exep/2012Appendix_Fall.pdf).
- Leger, A., Rouan, D., Schneider, J., Barge, P., Fridlund, M., et al. “Transiting exoplanets from the CoRoT space mission. VIII. CoRoT-7b: the first super-Earth with measured radius.” *Astronomy and Astrophysics* 506, Issue 1 (2009): 287–302.
- Lindgren, L., Lammers, U., Hobbs, D., et al. “The astrometric core solution for the Gaia mission.” *Astronomy & Astrophysics* 538, A78 (2012).
- Jack J. Lissauer, Daniel C. Fabrycky, Eric B. Ford, William J. Borucki, Francois Fressin, Geoffrey W. Marcy, Jerome A. Orosz, Jason F. Rowe, Guillermo Torres, William F. Welsh, Natalie M. Batalha, Stephen T. Bryson, Lars A. Buchhave, Douglas A. Caldwell, Joshua A. Carter, David Charbonneau, Jessie L. Christiansen, William D. Cochran, Jean-Michel Desert, Edward W. Dunham, Michael N. Fanelli, Jonathan J. Fortney, Thomas N. Gautier III, John C. Geary, Ronald L. Gilliland, Michael R. Haas, Jennifer R. Hall, Matthew J. Holman, David G. Koch, David W. Latham, Eric Lopez, Sean McCauliff, Neil Miller, Robert C. Morehead, Elisa V. Quintana, Darin Ragozzine, Dimitar Sasselov, Donald R. Short, and Jason H. Steffen “A closely packed system of low-mass, low-density planets transiting Kepler-11.” *Nature* 470 (2011): 53–58.
- Lopez, Eric, and Fortney, J. J. “How Thermal Evolution and Photo-Evaporation Sculpt Kepler’s Sub-Neptunes and Super-Earths.” *American Astronomical Society*, DPS meeting #45, #200.08. (2013).
- Lyon, R. G., Clampin, M., Petrone, P., Mallik, U., Madison, T., and Bolcar, M. R. “High contrast vacuum nuller testbed (VNT) contrast, performance, and null control.” *Proc. SPIE* 8442, 8442-08 (2012).
- Marcy, G., Butler, R. P., Fischer, D., Vogt, S., Wright, J. T., Tinney, C. G., and Jones, H. R. A. “Observed Properties of Exoplanets: Masses, Orbits, and Metallicities.” *Progress of Theoretical Physics Supplement*, No. 158 (2005): 24–42.
- Marcy, Geoffrey W., Isaacson, Howard, Howard, Andrew W., Rowe, Jason F., Jenkins, Jon M., et al. “Masses, Radii, and Orbits of Small Kepler Planets: The Transition from Gaseous to Rocky Planets.” *The Astrophysical Journal Supplement* 210, 2, article id. 20 (2014): 70 pp.
- Marley, M.S., et al. “On the luminosity of young Jupiters.” *The Astrophysical Journal* 655 (2007): 541–549.
- Marois, C., et al. “Extrasolar planets: A giant surprise.” *Nature* 468 (2010): 1048–1049.
- Marois, C., Zuckerman, B., Konopacky, Q., et al. “Images of a fourth planet orbiting HR 8799” *Nature* 468 (2010): 1080–1083.
- Marois, C., Macintosh, B., and Verian, J-P. “Exoplanet imaging with LOCI processing: photometry and astrometry with the new SOSIE pipeline.” *Proc. SPIE* 7736 (2010).
- Mendillo, C. B., et al. “Flight demonstration of a milliarcsecond pointing system for direct exoplanet imaging.” *Applied Optics* 51, no. 29 (2012).
- Misra et al. 2014 (in review).
- Mouillet, D., Larwood, J. D., Papaloizou, J. C. B., and Lagrange, A. M. “A planet on an incline orbit as an explanation for the warp in the beta Pictoris disc.” *MNRAS* 292 (1997): 896–904.
- N’Diaye, M., Dohlen, K., and Paul, B. “Calibration of quasi-static aberrations in exoplanet direct imaging instruments with

- a Zernike phase-mask sensor.” *Astronomy & Astrophysics* 29 (2013).  
arXiv:1305.5143v2.
- Nesvorny, D., Jenniskens, P., Levison, H. F., Bottke, W. F., Vokrouhlický, D., and Gounelle, M. “Cometary Origin of the Zodiacal Cloud and Carbonaceous Micrometeorites. Implications for Hot Debris Disks.” *The Astrophysical Journal* 713, no. 2 (2010): 816–836.
- Oberg, K. I., Murray-Clay, R., and Bergin, E. A. *The Astrophysical Journal Letters* 743, L16 (2011).
- Oppenheimer, B. and Hinkley, S. “High-contrast observations in optical and infrared astronomy.” *Annual Review of Astronomy and Astrophysics* 47 (2009): 253–289.
- Pollack, James B., Olenka Hubickyj, Peter Bodenheimer, Jack J. Lissauer, Morris Podolak, and Yuval Greenzweig. “Formation of the Giant Planets by Concurrent Accretion of Solids and Gas.” *Icarus* 124, no. 1 (1996): 62–85.
- Roberge, A., Chen, C. H., Millan-Gabet, R., Weinberger, A. J., Hinz, P. M., Stapelfeldt, K. R., Absil, O., Kuchner, M. J., and Bryden, G. “The Exozodiacal Dust Problem for Direct Observations of Exo-Earths.” *Publications of the Astronomical Society of the Pacific* 124 (2012): 799–808.
- Schneider, G., Weinberger, A. J., Becklin, E. E., Debes, J. H., and Smith, B. A. “STIS Imaging of the HR 4796A Circumstellar Debris Ring.” *The Astronomical Journal* 137, no. 5 (2009): 3–61.
- Serabyn, E., Mawet, D., Trauger, J. T., Moody, M., Liewer, K., Krist, J. E., and Kern, B. D. “High-contrast imaging with the vortex coronagraph.” *Proc. SPIE* 8864, 8864-32 (2013).
- Shao, M., et al. “DAVINCI, a dilute aperture visible nulling coronagraph instrument.” *Proc. SPIE* 7013, 789767 (2008).
- Sharkey, J. P., G. S. Nurre, G. A. Beals, and J. D. Nelson. “A chronology of the on-orbit pointing control system changes on the Hubble Space Telescope and associated pointing improvements.” AIAA-92-4618-CP.
- Stahl, H. Philip, Todd Henrichs, Alexander Luedtke, and Miranda West. “Update to single-variable parametric cost models for space telescopes.” *Optical Engineering* 52(9), 091805 (2013).  
<http://dx.doi.org/10.1117/1.OE.52.9.091805>.
- Stapelfeldt, K. “The Scientific requirements for extremely large telescopes.” *Proceedings of the International Astronomical Union Symposium* 232 (2006): 149–158.
- Su., K. Y. L., Rieke, G. H., Stapelfeldt, K. R., et al. “The Debris Disk around HR 8799.” *The Astrophysical Journal* 705 (2009): 314–327.
- Trauger, J., Moody, D., Gordon, B., Krist, J., and Mawet, D. “Complex apodization Lyot coronagraphy for the direct imaging of exoplanet systems: design, fabrication, and laboratory demonstration.” *Proc. SPIE* 8442, 8442-4Q (2012).
- Trauger, J., et al. “ACCESS: a concept study for the direct imaging and spectroscopy of exoplanetary systems.” *Proc. SPIE* 7731, 773128 (2010).
- Trauger, J., et al. “A space Coronagraph Concept for direct imaging and spectroscopy of Exoplanetary SystemS (ACCESS).” *ASMC Study Report* (2009).  
[http://exep.jpl.nasa.gov/files/exep/access\\_compiled\\_report\\_public\\_090610.pdf](http://exep.jpl.nasa.gov/files/exep/access_compiled_report_public_090610.pdf).
- Weisskopf, M., Aldcroft, T., Bautz, M., Cameron, R., Dewey, D., Drake, J., Grant, C., Marshall, H., and Murray, S. “An Overview of the Performance of the Chandra X-ray Observatory.” *Experimental Astronomy*, 16, no. 1 (2003): 1–68.
- WFIRST-AFTA Science Definition Team Final Report (2013). [http://wfirst.gsfc.nasa.gov/science/sdt\\_public/wfirst-afta\\_sdt\\_final\\_report\\_rev1\\_130523.pdf](http://wfirst.gsfc.nasa.gov/science/sdt_public/wfirst-afta_sdt_final_report_rev1_130523.pdf).

## 12.2 Acronyms

ACCESS	Actively-Corrected Coronagraphs for Exoplanetary System Studies	CVD	chemical vapor deposited
ACE	Ames Coronagraph Experiment	CVZ	continuous viewing zone
ACS	attitude control system	DM	deformable mirror
ADCS	Attitude Determination and Control Subsystem	DMC	Data Management Center
ADI	angular difference imaging	DOF	degree of freedom
AFTA	Astrophysics Focused Telescope Asset	DSN	Deep Space Network
ALMA	Atacama Large Millimeter/submillimeter Array	ECB	Exo-C control box
AOI	angle-of-incidence	EDU	Engineering Design Unit
AOX	Adaptive Optics Associates/Xinetics	EE	encircled energy
APRA	Astrophysics Research and Analysis	E-ELT	European Extremely Large Telescope
ARC	Ames Research Center	ELT	Extremely Large Telescope
ASMCS	Astrophysics Strategic Mission Concept Studies	EMCCD	electron multiplying charge coupled device
AU	astronomical unit	ENF	excess noise factor
BCA	bus control assembly	EOL	end-of-life
BOE	basis of estimate	EOS	Electromagnetic Observations from Space
CAD	computer-aided design	EPD	entrance pupil diameter
CADRe	Cost Analysis Data Requirement	EPDS	Electrical Power and Distribution Subsystem
CATE	Cost Appraisal and Technical Evaluation	EPIC	Extrasolar Planetary Imaging Coronagraph
CBE	current best estimate	ESA	European Space Agency
CCD	charge coupled device	ESPRESSO	Echelle SPECTrograph for Rocky Exoplanet and Stable Spectroscopic Observations
CDI	coherence difference imaging	EXCEDE	EXoplanetary Circumstellar Environments and Disk Explorer
CG	center of gravity	ExEP	Exoplanet Exploration Program
CHARIS	Coronagraphic High Angular Resolution Imaging Spectrograph	FEM	finite element model
CLOWFS	Coronagraphic Low Order Wavefront Sensor	FGS	fine-guidance sensor
CMOS	complementary metal–oxide–semiconductor	FPA	focal-plane array
CNC	computer numerical control	FOV	field-of-view
CoRoT	COncvection ROTation et Transits	FMD	flight management system
CSS	coarse Sun sensor	FPC	Flight Planning Center
CTE	coefficient of thermal expansion	FS	flight segment
		FSM	fine-steering mirror
		FSW	flight software
		FWHM	Full-width, half-maximum
		Galex	Galaxy Evolution Explorer
		GDS	ground data system

GMT	Giant Magellan Telescope	OSIRIS	OH-Suppressing InfraRed Imaging Spectrograph
GPI	Gemini Planet Imager	OTA	optical telescope assembly
GS	Ground Segment	OVC	optical vortex coronagraph (
HCIT	High-Contrast Imaging Testbed	OWA	outer working angle
HGA	high-gain antenna	PCA	principal component analysis
HST	Hubble Space Telescope	PDI	polarization difference imaging
IB	inner barrel	PDR	Preliminary Design Review
IBA	inner barrel assembly	PEC	precision external clock
ICE	instrument control electronics	PECO	Pupil mapping Exoplanet Coronagraphic Observer
IFS	integral field spectrograph	PEL	Power Equipment List
IMU	inertial measurement unit	PIAA	phase-induced amplitude apodization
IR	infrared	PID	proportional-integral-derivative
IRU	inertial reference unit	PISCES	Prototype Imaging Spectrograph for Coronagraphic Exoplanet Studies
IWA	inner working angle	PLATO	Planetary Transits and Oscillations of stars
JPL	Jet Propulsion Laboratory	PM	primary mirror
JWST	James Webb Space Telescope	PMA	primary mirror assembly
LBTI	Large Binocular Telescope Interferometer	PMB	primary mirror bipods
LGA	low-gain antenna	PPE	payload processing electronics
LOCI	locally optimized combination of images	PPMZWFS	Pupil Plane Mach-Zehnder Wavefront Sensor
LOWFS	low-order wavefront sensor	PSF	point spread function
LV	launch vehicle	PSS	Project Scheduling Service
M	magnification	PSS	primary mirror support structure
M	mirror	PSS	Project Scheduling Service
MEL	Master Equipment List	QE	quantum efficiency
MIRI	Mid InfraRed Instrument	RBA	rigid body actuator
MIT	Massachusetts Institute of Technology	RCS	reaction control system
MMO	Mission Management Office	RF	radio frequency
MOC	Mission Operations Center	RMS	root mean square
MOS	mission operations system	RV	radial velocity
NASA	National Aeronautics and Space Administration	RWA	reaction wheel assembly
NICM	NASA Instrument Cost Model	SAT	Strategic Astrophysics Technology
NIRCam	Near Infrared Camera	SBIR	Small Business Innovation Research
NIRSpec	Near InfraRed Spectrograph	S/C	spacecraft
OAP	off-axis parabola		
OB	outer barrel		
OBA	outer barrel assembly		
OPZ	operational pointing zone		

SCExAO	Subaru Coronagraphic Extreme Adaptive Optics	TDI	time-delayed integration
SDI	spectral difference imaging	TESS	Transiting Exoplanet Survey Satellite
SFE	surface figure error	TMT	Thirty Meter Telescope
SM	secondary mirror	TRL	technology readiness level
S/N	signal-to-noise	TWTA	traveling wave tube amplifier
SNR	signal-to-noise ratio	ULE	ultra-low expansion
SO	Science Office	UV	ultraviolet
SOC	Science Operations Center	VLT	Very Large Telescope
SPHERE	Spectro-polarimetric High-contrast Exoplanet Research	WBS	Work Breakdown Structure
SSR	solid-state recorder	WFC	wavefront control
SSS	starlight suppression system	WFE	wavefront error
STB	system test bed	WFIRST	Wide-Field Infrared Survey Telescope
STDT	Science and Technology Definition Team	WFSC	wavefront sensing and control
STOP	structural, thermal, optical, performance	WISE	Wide-field Infrared Survey Explorer
TCE	telescope control electronics	ZLWS	Zernike Low-order Wavefront Sensor
TCS	thermal control subsystem	ZWFS	Zernike Wavefront Sensor
TDEM	Technology Development for Exoplanet Missions		